

SPSD II

MODELLING THE EVOLUTION OF CLIMATE AND SEA LEVEL DURING THE THIRD MILLENNIUM (MILMO)

T. FICHEFET, PH. HUYBRECHTS, H. DECLEIR, G. MUNHOVEN



PART 2

GLOBAL CHANGE, ECOSYSTEMS AND BIODIVERSITY



ATMOSPHERE AND CLIMATE



MARINE ECOSYSTEMS AND BIODIVERSITY



TERRESTRIAL ECOSYSTEMS AND BIODIVERSITY



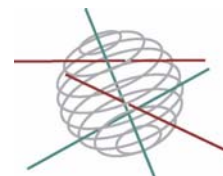
NORTH SEA



ANTARCTICA

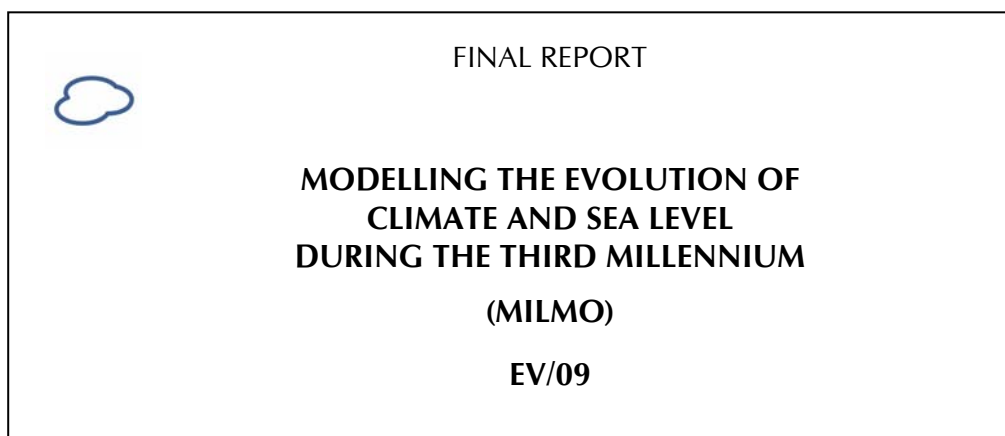


BIODIVERSITY



Part 2:

Global change, Ecosystems and Biodiversity



Thierry Fichet, Emmanuelle Driesschaert & Hugues Goosse

Université Catholique de Louvain, Institut d'Astronomie et de
Géophysique Georges Lemaître (UCL-ASTR)
Chemin du Cyclotron, 2
B-1348 Louvain-la-Neuve

Philippe Huybrechts & Ives Janssens

Vrije Universiteit Brussel, Departement Geografie (VUB-DGGF)
Pleinlaan, 2
B-1050 Brussels

Anne Mouchet & Guy Munhoven

Université de Liège, Département d'Astrophysique, de Géophysique et
d'Océanographie, Laboratoire de Physique Atmosphérique et Planétaire
(ULg-LPAP)
Allée du 6 août, 17
Bâtiment B5c
B-4000 Liège





D/2007/1191/11

Published in 2007 by the Belgian Science Policy

Rue de la Science 8

Wetenschapsstraat 8

B-1000 Brussels

Belgium

Tel: +32 (0)2 238 34 11 – Fax: +32 (0)2 230 59 12

<http://www.belspo.be>

Contact person:

Mrs Martine Vanderstraeten

Secretariat: +32 (0)2 238 36 13

Neither the Belgian Science Policy nor any person acting on behalf of the Belgian Science Policy is responsible for the use which might be made of the following information. The authors are responsible for the content.

No part of this publication may be reproduced, stored in a retrieval system, or transmitted in any form or by any means, electronic, mechanical, photocopying, recording, or otherwise, without indicating the reference.

TABLE OF CONTENTS

ABSTRACT	5
1. INTRODUCTION	11
2. DESCRIPTION OF LOVECLIM.....	15
2.1. ECBilt	15
2.2. CLIO	16
2.3. VECODE	17
2.4. LOCH.....	18
2.5. Coupling of LOCH with ECBilt–CLIO–VECODE.....	20
2.6. AGISM.....	21
2.7. Coupling of AGISM with ECBilt–CLIO–VECODE.....	25
2.8. Global glacier-melt algorithm.....	27
3. MODELLING THE EVOLUTION OF CLIMATE, SEA LEVEL AND CARBON CYCLE DURING THE LAST FEW CENTURIES.....	31
3.1. Forcings.....	31
3.2. Experimental design.....	34
3.3. Results.....	34
3.3.1. <i>Climate</i>	34
3.3.2. <i>Ice sheets, glaciers and sea level</i>	40
3.3.3. <i>Carbon cycle</i>	46
3.4. Conclusions.....	52
4. PROJECTIONS OF CLIMATE, SEA-LEVEL AND CARBON-CYCLE CHANGES OVER THE 21ST CENTURY	53
4.1. Forcing scenarios.....	53
4.2. Experimental design.....	53
4.3. Results	55
4.3.1. <i>Climate</i>	55
4.3.2. <i>Ice sheets, glaciers and sea level</i>	58
4.3.3. <i>Carbon cycle</i>	63

5. PROJECTIONS OF CLIMATE, SEA-LEVEL AND CARBON-CYCLE CHANGES OVER THE NEXT MILLENNIA	69
5.1. Forcing scenarios and experimental design.....	69
5.2. Results	73
5.2.1. <i>Climate</i>	73
5.2.2. <i>Ice sheets, glaciers and sea level</i>	85
5.3. Sensitivity experiments	95
5.3.1. <i>Interactions between the Greenland ice sheet and climate</i>	95
5.3.2. <i>Carbon cycle</i>	106
6. DISSEMINATION OF THE RESULTS.....	117
7. CONCLUSIONS AND RECOMMENDATIONS	119
REFERENCES	121

ABSTRACT

The overall objective of MILMO was to contribute to the international research effort leading to a better understanding of the Earth’s climate system, to improve projections of climate and sea-level changes at the century time-scale and beyond, and to explore the threat of possible rapid climate and sea-level changes during the next millennia. Three Belgian research teams have pooled their expertise in this project: the *Institut d’Astronomie et de Géophysique Georges Lemaître* of the *Université Catholique de Louvain*, the *Département Géographie* of the *Vrije Universiteit Brussels* and the *Laboratoire de Physique Atmosphérique et Planétaire* of the *Université de Liège*.

First of all, a new three-dimensional Earth system model of intermediate complexity was developed. This model, named LOVECLIM, consists of five major components representing the atmosphere (ECBilt), the ocean and sea ice (CLIO), the terrestrial biosphere (VECODE), the oceanic carbon cycle (LOCH) and the Greenland and Antarctic ice sheets (AGISM). It also includes a global glacier-melt algorithm which is run in off-line mode. It is worth mentioning that there are very few models of this type worldwide. ECBilt is a quasi-geostrophic atmospheric model with 3 levels and a T21 horizontal resolution. It includes simple parameterisations of the diabatic heating processes and an explicit representation of the hydrological cycle. Cloud cover is prescribed according to present-day climatology. CLIO is a primitive-equation, free-surface ocean general circulation model coupled to a thermodynamic–dynamic sea-ice model. Its horizontal resolution is $3^\circ \times 3^\circ$, and there are 20 levels in the ocean. VECODE is a reduced-form model of vegetation dynamics and of the terrestrial carbon cycle. It simulates the dynamics of two main terrestrial plant functional types (trees and grassland) at the same resolution as that of ECBilt. LOCH is a comprehensive model of the oceanic carbon cycle that takes into account both the solubility and biological pumps. The version utilised here has the same resolution as the one of CLIO, which greatly facilitates the coupling between both models. Finally, AGISM is composed of a three-dimensional thermomechanical model of the ice sheet flow, a visco-elastic bedrock model and a model of the mass balance at the ice–atmosphere and ice–ocean interfaces. The Antarctic ice-sheet module also contains a model of the ice-shelf dynamics to enable interactions with the ocean and migration of the grounding line. For both ice sheets, calculations are made on a $10 \text{ km} \times 10 \text{ km}$ resolution grid with 31 sigma levels.

The performance of LOVECLIM was assessed by conducting ensemble simulations over the last few centuries. Starting from different initial conditions, the model was integrated from year 1500 AD up to year 2000 AD with solar irradiance, volcanic activity, tropospheric ozone amount, greenhouse-gas (including CO_2)

concentrations and sulphate-aerosol load evolving with time according to reconstructions. Over the last 140 years, the model simulates a global surface warming ranging from 0.33°C to 0.43°C, with a mean value of 0.38°C. This value is about 0.15°C lower than the observed one. A detailed analysis of the results has revealed the model behaves reasonably well at mid- and high latitudes. By contrast, at low latitudes, the agreement between the model results and observational estimates is less good, especially in the Southern Hemisphere. In those regions, LOVECLIM significantly underestimates the warming and the climate variability observed during the last few decades. The coarse resolution of the model and the simplified representation of the atmospheric dynamical and physical processes seem to be the two major candidates responsible for this deficiency. Regarding the Greenland ice sheet, we found a slightly increasing ice volume during the period 1700–2000 AD. This trend is largely explained as a residual response to the late Holocene forcing, in particular to the Little Ice Age cooling after year 1500 AD. The effect is not particularly large, however, amounting to only 1.2 cm of global sea-level rise over the entire period. The growing trend stabilizes during the 20th century, with almost no net effect on ice volume. Only during the last decades of the 20th century, the ice volume begins to decrease in response to the imposed warming. We also found the Antarctic ice sheet to be retreating slowly at a rate equivalent to a global sea-level rise of about 1.7 cm during the 20th century. This evolution is mostly due to a long-term background trend of +2.6 cm, mitigated by about 0.9 cm from slightly rising accumulation rates over the same period. The ongoing dominance of past climatic changes on the contemporary ice-sheet evolution is a fine illustration of the inertia encountered when studying the response of large continental ice sheets. In this case, it mainly results from an ongoing grounding-line retreat in West Antarctica following rising sea levels since the Last Glacial Maximum. As far as mountain glaciers and small ice caps are concerned, their area and volume are found to reach a maximum in the late 19th century corresponding to the Little Ice Age, but this maximum and the ensuing 20th century glacier retreat are not very pronounced. Over the last hundred years, the model simulates an ice loss equivalent to only 0.89 cm of sea-level rise. This value is at the lower end compared to other assessments. One reason is the low total ice volume assumed by the global glacier-melt algorithm (about 20 cm of total sea-level rise, a factor 2.5 less than previous estimates). A second reason is the prescribed global ice mass balance for the 1961–1990 reference period, which is also at the lower end of other simulations. For the 20th century, LOVECLIM explains about 7.6 cm of sea-level rise. The bulk of that value, about 4.7 cm, comes from thermal expansion of the World Ocean. The Antarctic and Greenland ice sheets combined lead to a sea-level rise of 2 cm, and glaciers and ice caps are responsible for about 0.9 cm of sea-level rise. These numbers are similar to those that have been derived for the IPCC Third Assessment Report (TAR) for the

same components except for the lower glacier contribution as found here. Over the industrial era, the net uptake of carbon by the ocean simulated by LOVECLIM is within the range of current estimates, although at the lower end of this range. It should be noted that a detailed evaluation of the performance of the terrestrial carbon-cycle module was impossible to perform given the very wide range of available data. Experiments with interactive atmospheric CO₂ concentration were also carried out with LOVECLIM forced by CO₂ emissions from fossil fuel burning and land-use change. Interestingly enough, the atmospheric CO₂ level computed by the model in year 2000 AD compares relatively well with the observed one.

A series of climate-change projections were then conducted over the 21st century. In these experiments, LOVECLIM was driven by changes in greenhouse-gas (including CO₂), tropospheric ozone and sulphate-aerosol concentrations following the IPCC SRES scenarios B1, A1B and A2. In year 2100 AD, the model predicts a globally averaged, annual mean surface warming of 1°C, 1.4°C and 1.8°C for scenarios B1, A1B and A2, respectively, and an associated increase in precipitation of 3.6%, 5.1% and 6.6%, respectively. In agreement with studies performed with climate general circulation models (CGCMs), a weakening of the Atlantic meridional overturning circulation (MOC) is noticed in all runs. At the end of the 21st century, the decrease in the maximum value of the annual mean meridional overturning streamfunction below the surface layer in the Atlantic basin, which is an index of the MOC intensity, reaches 19% for scenario B1, 21% for scenario A1B and 27% for scenario A2. In our model, as in the majority of CGCMs, this decrease is caused more by changes in surface heat flux than by changes in surface freshwater flux. Under the forcing scenario A1B, LOVECLIM simulates a global sea-level rise of 31.3 cm in year 2100 AD. As for the 20th century, the most important contributor is the oceanic thermal expansion (+18.8 cm), followed by the contributions from the Greenland ice sheet (+5.2 cm), glaciers and ice caps (+3.8 cm) and the Antarctic ice sheet (+3.5 cm). The total rise is equivalent to a quadrupling of the sea-level rise simulated for the 20th century. Our sea-level value is somewhat lower than the central estimate for the same four components of about 40 cm in the IPCC TAR predictions. This can be explained by the low climate sensitivity of LOVECLIM, and hence the lower global temperature rise, which mostly affects the largest contribution of thermal expansion of the World Ocean. Another difference with the IPCC TAR predictions is the positive contribution from Antarctica of several cm of sea-level rise. That is in contrast to most other simulations showing a growing ice sheet and a negative contribution to global sea level of typically between -5 and -20 cm. The IPCC TAR also found a generally larger contribution from mountain glaciers and small ice caps. Our glacier-volume loss is smaller because of the lower initial glacier volume assumed by the glacier-melt algorithm. The total projected sea-level rise for the 21st century is only slightly affected by the scenario itself. For the range of SRES

scenarios used by LOVECLIM, the total sea-level rise is found to vary between +22 and +35 cm by year 2100 AD. The much larger range of between +9 and +88 cm obtained for the IPCC TAR arose mainly from the inclusion of model uncertainties, and not from the greenhouse-gas-forcing scenarios employed. As expected, climate change impacts the air–sea CO₂ exchange in the model by lowering the solubility and hence the net uptake of carbon by the ocean. The effect is however rather modest at the century time-scale given the moderate increase in sea-surface temperature simulated by LOVECLIM. In addition, we do not observe any significant change in the oceanic biology at the global scale during the 21st century. The picture is a bit different regarding the terrestrial biosphere. Both the climate and fertilization effects strongly increase the carbon uptake in VECODE. A number of experiments with interactive atmospheric CO₂ concentration were also carried out over the 21st century. Contrary to other modelling studies, LOVECLIM predicts lower atmospheric CO₂ levels at the end of the 21st century when the effect of climate change on the carbon cycle is accounted for in the model. The warming enhances the net uptake of carbon by the terrestrial biosphere which more than offsets the reduction in oceanic uptake resulting from the solubility decrease.

Finally, we have thoroughly analysed the model response to a range of stabilized anthropogenic forcings over the next millennia. For the variety of forcing scenarios considered, LOVECLIM simulates a globally averaged, annual mean surface warming ranging between 0.55°C and 3.75°C and an associated decrease in Arctic and Antarctic sea-ice extent. However, no simulation predicts an entirely ice-free Arctic Ocean during summertime at the millennium time-scale. In the most pessimistic case, a small ice pack of about 0.5×10^6 km² persists. Our results also suggest that it is very likely that the volume of the Greenland ice sheet will largely decrease in the future. After 1000 years of model integration, the ice volume is reduced by more than 20% when the radiative forcing is higher than 6.5 W m⁻². Moreover, for a radiative forcing greater than 7.5 W m⁻², the ice sheet melts away in less than 3000 years. Note that the ice-sheet disintegration might be even more rapid if processes responsible for the widespread glacier acceleration currently observed in Greenland were taken into consideration in the model. We also found that the freshwater flux from the melting Greenland ice sheet into the neighbouring oceans, which peaks in the most extreme scenario tested at 0.11 Sv (1 Sv = 10⁶ m³ s⁻¹) and remains above 0.1 Sv during three centuries, is not large enough to trigger a shutdown of the Atlantic MOC in our model, in contrast to some other models. Those models are however more responsive to freshwater perturbations than ours. Besides, we showed that climate feedbacks play a crucial role in the ice-sheet evolution and that the Greenland deglaciation considerably enhances the greenhouse-gas-induced warming over Greenland and the central Arctic. This stresses the importance of incorporating the two-way interactions between the Greenland ice sheet and climate

in climate- and sea-level-change projections at the millennial time-scale. For the Antarctic ice sheet, the response is much less drastic than for the Greenland ice sheet. For instance, after 3000 years of $4\times\text{CO}_2$ forcing ($\sim 7.7 \text{ W m}^{-2}$), the Antarctic grounded ice volume and area are reduced in our model by only 8% and 4 %, respectively. For a sustained radiative forcing of 8.5 W m^{-2} (the highest forcing scenario considered in our study), LOVECLIM predicts a global sea-level rise of 7.15 m by year 3000 AD. Most of it is due to melting of the Greenland ice sheet (+4.25 m), followed by melting of the Antarctic ice sheet (+1.42 m), thermal expansion (+1.29 m) and the contribution from mountain glaciers and small ice caps (+0.19 m). Our results show that it will be very difficult to limit the eventual sea-level rise to less than 1 m after 1000 years, unless the atmospheric CO_2 concentration can be stabilized to less than twice its pre-industrial level. Such a goal can only be reached by emission reductions far larger than any policy currently pursued. Concerning the carbon cycle, the experiments carried out with LOVECLIM highlight the opposite responses of the terrestrial and oceanic carbon reservoirs to climate change. We also found that, when anthropogenic CO_2 emissions cease, the terrestrial biosphere becomes a weak carbon source, while the ocean continues to be a sink. It should be mentioned that no dramatic change in the global marine productivity is observed in our simulations. This arises from the fact that the modifications of the oceanic properties that affect this productivity (stratification, meridional overturning, ...) are rather moderate. The effects of climate change are however not negligible. In particular, the decrease in sea-ice extent predicted by the model results in a longer growing season and a larger nutrient uptake (especially silica) in polar regions. As a result, by the end of the 23rd century, silica concentrations in the upper 100 m of the Southern Ocean drop by as much of 30% for the most extreme forcing scenarios.

1. INTRODUCTION

A large number of modelling studies have addressed the likely effects (including sea-level rise) of greenhouse-gas-induced climate change over the twenty-first century (see Houghton et al. (2001) for a review), but the longer-term effects have received much less attention. Yet these effects could be very significant, as a persistent increase in global mean temperature may ultimately influence the large-scale processes in the Earth system that play a central role in determining global climate.

The meridional overturning circulation (MOC) of the World Ocean is one such process. There is consensus today that this circulation is to a large extent driven from the high-latitude North Atlantic through the production of North Atlantic Deep Water (NADW). Sinking of surface water in the Greenland–Iceland–Norwegian (GIN) Seas and in the Labrador Sea initiates an overturning-circulation cell on the meridional plane in which the northward transport of upper-ocean warm water is balanced by a deep return flow of cold water, imposing a strong northward heat flux in both the North and South Atlantic (Gordon, 1986). Due to this transport, the northern North Atlantic is about 4°C warmer than the Pacific at similar latitudes. Changes in NADW circulation therefore have the potential to cause significant climate change over the North Atlantic region. The pioneering work by Stommel (1961) and other more recent studies (e.g., Rahmstorf, 1995) suggest that the MOC is a non-linear system which is highly sensitive to changes in freshwater forcing (i.e. evaporation, precipitation, river runoff, sea-ice formation/melting, ice-sheet and glacier melting, and iceberg calving). It may collapse if a certain threshold is exceeded and can show hysteresis behaviour. There is also growing evidence that some of the past climate shifts were associated with changes in NADW flow (e.g., Duplessy et al., 1988; Bond et al., 1993; Sarin et al., 1994). Furthermore, several studies with global atmosphere–sea-ice–ocean models indicate that a shutdown of the MOC could happen if anthropogenic emissions of greenhouse gases continue to rise beyond control (e.g., Manabe and Stouffer, 1994; Stocker and Schmittner, 1997; Rahmstorf and Ganopolski, 1999). Such a shutdown could enhance sea-level rise from oceanic thermal expansion and other contributions (e.g., Wiebe and Weaver, 1999; Knutti and Stocker, 2000). Nonetheless, it is not clear what the threshold is and how likely it is that human activity would lead it to being exceeded.

In addition, feedbacks related to the carbon cycle could accelerate future climate change. Modelling studies suggest that higher sea-surface temperatures, slower mixing with the deep ocean and less efficient biological pump all could lead to a reduction of the oceanic uptake of carbon dioxide (CO₂) (Sarmiento et al., 1995; Maier-Reimer et al., 1996; Joos et al., 1999; Matear and Hirst, 1999). The feedback

loop would be responsible for a decrease in CO₂ uptake by up to 25% in case of atmospheric CO₂ concentration equal to or higher than 1000 ppmv (Sarmiento et al., 1995; Joos et al., 1999).

Not only feedbacks between atmosphere, ocean and biogeochemical cycles could give rise to "surprises" in the climate system. Indeed, abrupt changes in the terrestrial vegetation are thought to have occurred in the past when anthropogenic perturbation was negligible (e.g., Claussen et al., 1999; deMenocal et al., 2000). These changes may be interpreted as non-linear changes triggered by slow variations in external, natural forcings. It is thus not excluded that such changes may happen in a near future.

Another important aspect of global climate change concerns the threat of significant sea-level rise. Global mean sea level has risen by about 1.5 mm per year during the twentieth century, and this rise is expected to accelerate if temperatures continue to increase (Houghton et al., 2001). About half of the observed rise is usually attributed to thermal expansion of the World Ocean, with the remainder being due to melting of mountain glaciers and the ongoing response of the Antarctic and Greenland ice sheets to past climatic changes as far back as the last glacial–interglacial transition. Although mountain glaciers contain less than 0.5% of the world's land-ice mass, they are more sensitive to climate change, and hence are expected to give a larger contribution to sea-level rise for most of the twenty-first century than the ice sheets of Greenland and Antarctica (e.g., de Wolde et al., 1997; Gregory and Oerlemans, 1998).

A continuous debate also concerns the stability of polar ice sheets. Simulations with dynamic ice-sheet models driven by outputs from climate-change experiments carried out with climate models indicate a relatively small response of the Greenland and Antarctic ice sheets during the twenty-first century, likely of opposite sign for both ice sheets (e.g., van de Wal and Oerlemans, 1997; Huybrechts and de Wolde, 1999). However, these studies have made clear that the ice sheets would continue to react for at least several millennia, even if the warming stabilises after the end of the twenty-first century. For a sustained regional, annual mean warming of more than 3°C, the Greenland ice sheet would melt away (Huybrechts and de Wolde, 1999; Greve, 2000; Gregory et al., 2004a). For warmings in excess of 10°C, total disintegration could take as little as 1000 years, in which case it would add an average of about 7 mm per year to sea level over the period, with wide-ranging implications for mankind. Regarding the West Antarctic ice sheet, it has long been argued that it may be inherently unstable because the bedrock at the grounding line slopes inland (Weertman, 1974) or because the grounded ice (inland ice) is abutted by large ice shelves that create "back pressure", such that ice-shelf thinning or break-up induced by future climate warming could cause the grounded ice to surge,

resulting in an abrupt sea-level rise of 4 to 6 m (e.g., Thomas, 1973; Oppenheimer, 1998). Such a collapse is considered very unlikely in the twenty-first century (Vaughan and Spouge, 2002), but the longer-term response of the ice sheet remains highly uncertain.

From the overview above, it is apparent that investigating the long-term response of climate and sea level to human activities requires the use of global three-dimensional models which include representations of all relevant components of the climate system (i.e. the atmosphere, the oceans, the ice masses, the upper Earth's mantle and the living world). But, most importantly, these models must be computationally fast enough so that integrations of longer duration and a larger number of sensitivity experiments can be performed than is currently the case with climate general circulation models (CGCMs). To achieve this requires some simplifications in the most CPU-time demanding model component, which is usually the atmospheric component.

Models of this type did not yet exist five years ago, but were being developed in several European and American research laboratories. One goal of the project *Modelling the evolution of climate and sea level over the third millennium (MILMO)* was to build such a model, named LOVECLIM, by coupling an efficient three-dimensional atmosphere–terrestrial biosphere–sea-ice–ocean model with a model of the oceanic carbon cycle and with thermomechanical models of the Greenland and Antarctic ice sheets. To close the sea-level contribution from the continental cryosphere, it was proposed to implement a global glacier-melt algorithm in off-line mode.

The overall objective of MILMO was to contribute with LOVECLIM to the international research effort leading to a better understanding of the climate system, to improve projections of climate and sea-level changes at the century time-scale and beyond, and to explore the threat of possible rapid climate and sea-level changes during the third millennium. More specifically, it was planned:

- to make as much projections as possible of climate and sea-level changes over both the twenty-first century and the next millennia using the most advanced scenarios for the anthropogenic forcing;
- to thoroughly analyse the changes in mean climate and climate variability simulated by the model;
- to quantify the influence of vegetation, carbon cycle and ice-sheet dynamics on the projections of climate and sea-level changes;
- to explore the thresholds for abrupt climate change in the next millennia and to identify the processes and feedbacks within the model that could induce such a change.

Three Belgian research teams have pooled their expertise in this project: the *Institut d’Astronomie et de Géophysique Georges Lemaître* of the *Université Catholique de Louvain* (UCL-ASTR; atmosphere, ocean and sea-ice modelling), the *Departement Geografie* of the *Vrije Universiteit Brussels* (VUB-DGGF; ice-sheet and glacier modelling) and the *Laboratoire de Physique Atmosphérique et Planétaire* of the *Université de Liège* (ULg-LPAP; carbon-cycle modelling).

In the rest of this report, we describe the different components of LOVECLIM and the coupling techniques developed during the project, we discuss the results of the simulations conducted with the model over the last centuries, the twenty-first century and the next millennia, we report on the dissemination of these results and on the degree of accomplishment of the initial objectives, and we end with some recommendations.

2. DESCRIPTION OF LOVECLIM

LOVECLIM consists of five major components representing the atmosphere (ECBilt), the ocean and sea ice (CLIO), the terrestrial biosphere (VECODE), the oceanic carbon cycle (LOCH) and the Greenland and Antarctic ice sheets (AGISM). It also includes a global glacier-melt algorithm which is run in off-line mode. Note that ECBilt, CLIO and VECODE were coupled together prior to MILMO. The reader is referred to <http://www.knmi.nl/onderzk/CKO/ecbilt-papers.html> for a full list of references on climate-change studies carried out with ECBilt–CLIO–VECODE.

2.1. ECBilt

ECBilt is a three-dimensional, spectral, quasi-geostrophic model of the atmosphere developed at the Koninklijk Nederlands Meteorologisch Instituut, De Bilt (Opsteegh et al., 1998). It has a T21 horizontal resolution and 3 levels located at 800, 500 and 200 hPa. As an extension to the quasi-geostrophic equations, an estimate of the neglected terms in the vorticity and thermodynamic equations is incorporated as a temporally and spatially forcing. This forcing is computed from the diagnostically derived field of vertical motion. With these ageostrophic terms, the simulation of the Hadley cells is considerably improved, resulting in a drastic improvement of the strength and position of the jet streams and transient eddy activity.

The model includes an explicit representation of the hydrological cycle and a dynamically passive stratospheric layer. Cloudiness is prescribed according to present-day climatology. The atmospheric boundary layer is not resolved. Temperature is therefore interpolated according to fixed lapse rates. Relative humidity is constant from the surface to the 500 hPa level. The surface wind speed is supposed to be 80% of the wind speed at 800 hPa.

The shortwave radiation scheme accounts for the absorption of solar radiation by atmospheric gases and clouds. Absorption is parameterised as a prescribed fraction of the incoming solar radiation. Reflection of solar radiation takes place at the top of the atmosphere and the surface. The reflected sunlight from the surface is completely reemitted to space. The longwave radiation scheme follows the approach proposed by Chou and Neelin (1996). Changes in longwave radiation fluxes result from perturbations in a reference vertical atmospheric profile taken from the ECHAM4 atmospheric general circulation model (AGCM). Those perturbations arise from changes in temperature, moisture and greenhouse-gas (including ozone) concentrations. They take the form of Green's functions for temperature and moisture, and have simpler forms for greenhouse gases. To take into consideration clouds, we combine the perturbed fluxes for clear sky conditions with those for cloudy

conditions using the actual cloud cover per grid cell. The global radiative forcing corresponding to a doubling of the atmospheric CO₂ concentration is 3.8 Wm⁻², which is very close to the best guess of Houghton et al. (2001), namely 3.7 Wm⁻².

The hydrological cycle is closed over land by using a bucket model for soil moisture. Each bucket is connected to a nearby oceanic grid cell to define river runoff. Accumulation of snow occurs in case of precipitation in areas with below 0°C surface temperature. As part of MILMO, a new land-surface scheme that takes into account the heat capacity of the soil has been inserted in the model.

Thanks to its coarse resolution and the simplifications made to the atmospheric dynamics and physics, ECBilt is two to three orders of magnitude faster than current atmospheric general circulation models (AGCMs).

2.2. CLIO

CLIO (Coupled Large-scale Ice–Ocean model) is a three-dimensional ocean–sea-ice model built at UCL-ASTR (Goosse and Fichefet, 1999).

The oceanic component is a primitive-equation, free-surface ocean general circulation model (Deleersnijder and Campin, 1995; Campin and Goosse, 1999). It contains a sophisticated formulation of the subgrid-scale vertical mixing derived from the Mellor and Yamada’s (1995) level-2.5 turbulence-closure scheme (Goosse et al., 1999) and a parameterisation of density-driven downslope flows (Campin and Goosse, 1999). Within MILMO, an isopycnal diffusion scheme, the Gent and McWilliams’ (1990) parameterisation of the tracer transport due to meso-scale eddies, a parameterisation of the large-scale interactions between Antarctic ice shelves and the ocean (Beckmann and Goosse, 2003), and a physically-based representation of the upper boundary condition for the salinity balance (Tartinville et al., 2001) were implemented in this model. Furthermore, a module that computes the contribution of the oceanic thermal expansion and/or haline contraction to global and regional sea-level changes was added.

The sea-ice component (Fichefet and Morales Maqueda, 1997) accounts for the heat capacity of the snow–ice system, the storage of latent heat in brine pockets trapped inside the ice, the effect of the subgrid-scale snow and ice thickness distributions on sea-ice thermodynamics, the formation of snow ice under excessive snow loading and the existence of leads within the ice pack. Ice dynamics are calculated by assuming that sea ice behaves as a two-dimensional viscous–plastic continuum.

The horizontal resolution of CLIO is 3° × 3°, and there are 20 unequally spaced levels in the ocean. The bathymetry is a discretized version of the real World Ocean’s

bottom topography. The only flux correction applied to CLIO when coupled to ECBilt is an artificial reduction of precipitation over the Atlantic and Arctic Oceans, and a homogeneous distribution of the removed amount of freshwater over the Pacific Ocean (Goosse et al., 2001).

2.3. VECODE

VECODE (VEgetation COn tinuous DEscription model) is a reduced-form model of the vegetation dynamics and of the terrestrial carbon cycle (Brovkin et al., 2002).

This model simulates at the same resolution as the one of ECBilt the dynamics of two main terrestrial plant functional types: trees and grassland. The equilibrium tree fraction in a given grid cell, f_t , is taken as a function of climatic parameters (the positive degree-day (PDD) index and the annual mean precipitation). This function was designed to fit at best the observations. Three major assumptions were made to derive it. (1) In a cold climate, temperature is the major limiting factor of forest growth. Moreover, below a given threshold, the tree fraction declines rapidly to zero. (2) In a warm climate, the annual mean precipitation is the main limiting factor of forest growth. (3) Isolines of tree concentration correspond to constant wetness conditions (depending on temperature and precipitation). The equilibrium fraction of desert (i.e., bare soil), f_d , is also obtained from climatic parameters using empirical formulas. Two types of desert are distinguished: cold and warm ones. In cold deserts (e.g., Antarctica), where temperature is the limiting factor, the dependence of vegetation fraction on rainfall is ignored. By contrast, in warm deserts (e.g., Sahara), rainfall is the limiting factor of plant growth. The equilibrium grassland fraction, f_g , is then $1 - f_t - f_d$. If climate changes, the model simulates vegetation transition from the equilibrium for the previous climate towards an equilibrium for the new climate. The time scale of this transition is determined from the carbon-cycle component of the model.

In this component, four carbon compartments are considered, all having different turnover times: a fast pool of green biomass (leaves), a slow pool of structural biomass (stems, roots), a fast pool of organic matter (woody residues) and a slow pool of organic matter (humus). The equations describing the dynamics of the carbon in those pools mainly depend on the decay rate of the carbon in each pool. The total input flux of carbon into the biomass is equal to the net primary productivity (NPP). In VECODE, the NPP does not depend on the vegetation cover but only on the climatic parameters. However, the fertilization effect is taken into account: the NPP increases in a logarithmic way with the atmospheric CO₂ abundance.

It is worth mentioning that the simulated vegetation changes only affect the land-surface albedo in ECBilt and have no influence on other processes such as, for instance, evapotranspiration.

2.4. LOCH

LOCH (Lière Ocean Carbon Heteronomous model; Mouchet and François, 1996) is three-dimensional oceanic carbon-cycle model developed at ULg-LPAP. It simulates the fate of dissolved inorganic carbon, total alkalinity, phosphates, dissolved and particulate organic matter, silica, oxygen as well as organic and inorganic ^{13}C and ^{14}C . The concentration of dissolved CO_2 at the sea surface is controlled by both physical and biological processes (solubility and biological pumps, respectively). Hence, LOCH includes physical, chemical and biological modules.

The alkalinity and dissolved organic carbon are both needed to determine the concentration of dissolved CO_2 in surface waters as well as the CaCO_3 saturation level in deep waters. The total dissolved inorganic carbon (DIC) represents the sum of dissolved CO_2 , bicarbonate and carbonate. The total alkalinity, a measure of the acid neutralizing capacity of seawater, is computed using the definition of Dickson (1981). However, in order to reduce the computing time, this definition is simplified by retaining only the essential contributions (bicarbonate, carbonate and borate). The error coming from the neglect of phosphates and silicates is by far smaller than other uncertainties inherent to climate modelling. The constants required to determine the various chemical equilibria in seawater are taken from Dickson and Goyet (1996) and expressed on the pH seawater scale.

The magnitude of the air–sea flux of a gas depends on the difference of its partial pressure between the two media, with an exchange rate given by the product of the solubility and the piston velocity. The solubilities are taken from Wanninkhof (1992) for O_2 and from Weiss (1974) for CO_2 . The piston velocity follows the empirical formulation proposed by Wanninkhof (1992), which relates it to the squared wind velocity and the Schmidt's number. The latter is gas-dependent and is calculated according to Wanninkhof (1992).

The biological activity exerts a strong control on the surface CO_2 at long time-scales by being responsible for the fast transfer of carbon to the deep-ocean layers. Therefore, we do not consider the total primary production but only that part which escapes recycling in the euphotic layers. The basis for the export-production model is a pool of phytoplankton whose growth is driven by the availability of nutrients (phosphates) and light. The various parameters of the biological module were tuned by forcing it with climatological phosphate reconstructions. The export-production fields obtained in this way were then compared with available estimates. The organic

matter resulting from the death of organisms is represented as fast sinking particulate organic matter (POM), which is subsequently remineralized at depths or broken down so as to feed the dissolved organic matter (DOM) pool. The distribution of POM with depth is governed by a power law of the vertical coordinate as suggested by Martin et al. (1987), but the actual vertical profile driving the distribution of POM may evolve in accordance with the ecosystem composition (Klaas and Archer, 2002).

The remineralization of organic matter depends on oxygen availability, but anoxic remineralization can occur in O₂-depleted regions. The module describing the fate of the organic matter differs from previous LOCH versions and was entirely renewed during the MILMO project. Indeed, the previous formulation exhibited some shortcomings in O₂-depleted waters, which led to unrealistic lifetimes of organic matter.

The hard tissues (shells) are made up of CaCO₃ or opal, and their precipitation occurs concurrently with the soft-tissue formation. One important factor for the carbon cycle is the rain ratio, which is the amount of organic carbon assimilated during photosynthesis over that of inorganic carbon incorporated into shells. This rain ratio depends in the model on the availability of silica, the latter determining which type of shells will be preferentially built. The influence of temperature and the ubiquity of calcareous organisms are also included in the parameterisation of this process. The dissolution of shells occurs in the deepest water layer below the production area. For opal, a simple constant rate is used, while the dissolution of CaCO₃ shells is chemically driven. Both the calcite and aragonite forms are considered during this process. The pressure dependency formulations of the chemical equilibrium constants are taken from Millero (1979) and UNESCO (1987).

Some organic matter and shells escape remineralization or dissolution, and are permanently preserved in sediments. On the other hand, river input of alkalinity, silica, nutrients and carbon constitutes a net source for the ocean. In the case of an equilibrium run, this source exactly compensates the permanent preservation in sediments. The main rivers of the world and their respective importance are taken into account in this process.

The various fluxes for ¹³C and ¹⁴C are proportional to those of ¹²C with a fractionation factor depending on the considered process (air–sea exchange, phytoplankton growth, ...). The decay of ¹⁴C is modelled with a half life-time of 5728 years.

LOCH also includes an atmospheric module which simulates the evolution of the various gases in the atmosphere (CO₂, ¹³CO₂, ¹⁴CO₂ and O₂). The atmosphere is considered to be well mixed in the zonal direction, whereas the meridional transport is represented by a diffusive law. The concentrations of atmospheric gases are then

predicted on the basis of the fluxes to or from the ocean and the terrestrial biosphere, and, if applicable, any other sources (e.g., anthropogenic emissions).

The atmospheric module offers two options for the study of the carbon cycle: either the concentrations are prescribed in the atmosphere (diagnostic mode) or the concentrations evolve according to the various exchange processes as described above (prognostic mode). In the current version of the model, oxygen and isotopes of carbon in CO₂ are not exchanged with the terrestrial biosphere. The incorporation of those processes in the model is under way.

2.5. Coupling of LOCH with ECBilt–CLIO–VECODE

LOCH has been fully coupled to CLIO. As the two models run on the same grid, LOCH makes directly use of the basin geometry and ocean dynamics provided by CLIO. The time step for solute transport in LOCH is the same as the time step for tracer transport in CLIO, thus eliminating the need for any interpolation procedure. Furthermore, all exchanged quantities consist in gross values, and not anomalies like in the coupling of AGISM with ECBilt–CLIO–VECODE (see Section 2.7), rendering the coupling rather straightforward.

The transport in LOCH is based on two-dimensional and three-dimensional fields provided by CLIO: downsloping flows and heights, salt and freshwater fluxes at the sea surface, current velocities, and vertical and horizontal diffusivities. LOCH uses a numerical scheme for advection which differs from the one of CLIO. The reason for this difference is to be found in the non-monotonic behaviour of the CLIO advection scheme, which results in negative tracer concentrations. On the other hand, the carbon-cycle results presented in this report were obtained without considering in LOCH the effects on the tracer distributions of the oceanic isopycnal mixing and of the Gent and McWilliams’ (1990) parameterisation for meso-scale eddies. The non-monotonic behaviour of isopycnal mixing is a well-known problem (Mathieu and Deleersnijder, 1998), but the conservation problems encountered with the Gent and McWilliams’ (1990) parameterisation were unexpected. The cause of this anomalous behaviour was eventually discovered and corrected.

Another difficulty emerged when the coupling was achieved and the first on-line experiments were performed. The ocean CO₂ uptake during the 1990’s produced by the coupled model was well above the range of accepted values. Moreover, the distribution of tracers in the Pacific Ocean (PO₄, O₂, SiO₂, ...) did not reflect the strong vertical stratification typical of that ocean. After analysis, it became clear that these problems were related to too high a sensitivity at depths of the vertical velocity in response to the atmospheric forcing. The high frequency fluctuations of the vertical velocity combined with the numerical diffusivity associated with the transport scheme

in LOCH and resulted in too much apparent mixing between surface and deep waters. Two actions were then taken. In a first step, the vertical advection scheme in LOCH was replaced by a second-order scheme, thus eliminating the artificial diffusivity. Then, we concentrated some efforts in determining the cause of this behaviour. It seems to be of numerical origin but some work is still needed in order to confirm this hypothesis. A solution to this problem is necessary in order to properly predict the isotopic ratios; indeed, the non-monotonic behaviour of the second-order advection scheme results in spurious spikes in these ratios. It should be kept in mind that it is the first time that biogeochemical tracers are computed on-line with this model. Such tracers more closely reflect the ocean-interior circulation than do temperature and salinity, and it should be no surprise that they put in evidence any circulation shortcoming.

The chemical constants, the gas-exchange coefficients and other parameters of LOCH are computed from the temperature and salinity fields provided by CLIO. The piston velocity is determined from the wind field simulated by ECBilt. The growth rate of the phytoplankton biomass is set according to the same amount of available light at the sea surface (under the ice in ice-covered areas) as in CLIO; we however use a different extinction coefficient with depth. The sea-ice areal coverage modelled by CLIO is also taken into consideration in the calculation of the air–sea fluxes of gases.

VECODE provides annual mean values of the CO₂ fluxes between atmosphere and continents (soils and vegetation) on the same grid as ECBILT. The atmosphere in LOCH is defined on a grid with zonal bands which are equally spaced in latitude. A spatial interpolation procedure was then added to the coupled model in order to define the correspondence between both grids while preserving the latitudinal distribution of fluxes. Combining the carbon fluxes from the continents and from the ocean, LOCH computes a globally averaged, annual mean atmospheric CO₂ concentration which is transmitted to ECBILT and VECODE, where it impacts on the radiative transfer and fertilization, respectively.

In order to achieve computing efficiency, LOCH is first equilibrated off-line with a prescribed atmospheric CO₂ concentration (280 ppmv). This limits the adjustment time when the carbon cycle is fully interactive

2.6. AGISM

AGISM (Antarctic and Greenland Ice-Sheet Model) consists of two three-dimensional thermomechanical ice-dynamics models for each of the polar ice sheets. Both models are based on the same physics and formulations, however with the major distinction that the Antarctic component incorporates a coupled ice shelf and grounding line dynamics. Ice-shelf dynamics is missing from the Greenland

component as there is hardly any floating ice under present-day conditions, and this can be expected to disappear quickly under warmer conditions. Having a melt margin on land or a calving margin close to its coast for most of its glacial history, ice shelves probably played a minor role for Greenland also during colder conditions.

Both polar ice-sheet models have three main components which respectively describe the ice flow, the solid Earth's response and the mass balance at the ice-atmosphere and ice-ocean interfaces (Huybrechts and de Wolde, 1999; Huybrechts, 2002). Figure 1 shows the structure of the model. At the heart of these models is the simultaneous solution of two evolutionary equations for ice thickness and temperature, together with diagnostic representations of the ice-velocity components. In grounded ice, the flow results from both internal deformation and sliding over the bed in places where the temperature reaches the pressure melting point and a lubricating water layer is present. Ice deformation in the ice-sheet domain is caused by vertical shearing, most of which occurs near to the base. For the sliding velocity, a generalised Weertman's relation is adopted, taking into account the effect of the subglacial water pressure. Ice shelves are included by iteratively solving a coupled set of elliptic equations for ice-shelf spreading in two dimensions, including the effect of lateral shearing induced by sidewalls and ice rises. At the grounding line, longitudinal stresses are accounted for in the effective stress term of the flow law. These additional stress terms are found by iteratively solving three coupled equations for depth-averaged horizontal stress deviators. The temperature dependence of the rate factor in Glen's flow law is represented by an exponential Arrhenius' equation.

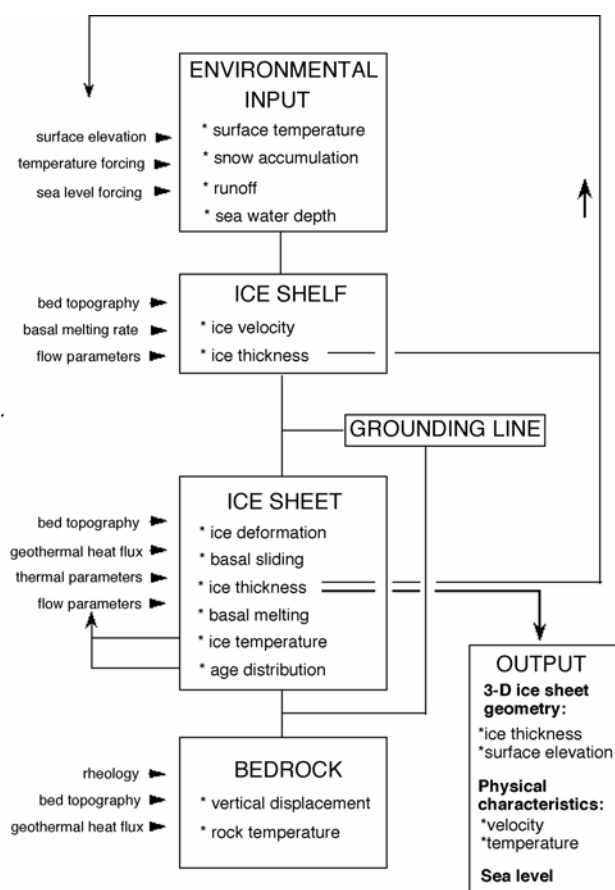


Figure 1: Structure of the three-dimensional ice-sheet model AGISM. The inputs are given at the left-hand side. Prescribed environmental variables drive the model, which has ice shelves, grounded ice and bed adjustment as major components. For the Antarctic component, the position of the grounding line is not prescribed, but internally generated. Ice thickness feeds back on surface elevation, an important parameter for the calculation of the mass balance. The model essentially outputs the time-dependent ice-sheet geometry and the coupled temperature and velocity fields.

Isostasy is taken into account for its effect on bed elevation near grounding lines and marginal ablation zones, where it matters most for ice-sheet dynamics, and because isostasy enables ice sheets to store 25–30% more ice than evident from their surface elevation alone. The bedrock adjustment model consists of a viscous asthenosphere, described by a single isostatic relaxation time, which underlies a rigid elastic plate (lithosphere). In this way, the isostatic compensation takes into consideration the effects of loading changes within an area several hundred kilometers wide, giving rise to deviations from local isostatic equilibrium. The value for the flexural rigidity (1×10^{25} N m) corresponds to a lithospheric thickness of 115 km; the characteristic relaxation time for the asthenosphere is 3000 years. This treatment produces results close to those from more sophisticated visco-elastic models, while at the same time being much more efficient in terms of computational

overhead. The loading accounts for contributions from both ice and ocean water within the respective grids, but ignores any ice loading changes beyond the Greenland and Antarctic continental areas.

Both models have a horizontal resolution of 10 km with 31 vertical layers in the ice, and another 9 layers in the bedrock for the calculation of the heat conduction in the crust. The inclusion of heat conduction in the bedrock gives rise to a variable geothermal heat flux at the ice-sheet base depending on the thermal history of the ice and rock. The 10-km grids represent a doubling of the horizontal resolution with respect to previous versions of the model. The opportunity was taken to implement upgraded geometric datasets for surface elevation, ice thickness and bed elevation incorporating the most recent observations (Liu et al., 1999; Lythe et al., 2001; Steinhage et al., 2001; Bamber et al., 2001). The higher horizontal resolution substantially improves the representation of the fast-flowing outlet glaciers and ice streams which are responsible for the bulk of the ice transport towards the margin. Other physics specific to these features such as higher-order stress components or subglacial sediment characteristics are not included, in common with the current generation of three-dimensional ice-sheet models.

Interaction with the atmosphere and the ocean is effectuated by prescribing the climatic input, consisting of the surface mass balance (accumulation minus ablation), surface temperature and the basal melting rate below the ice shelves surrounding the Antarctic component. The mass-balance model distinguishes between snow accumulation, rainfall and meltwater runoff, which components are all parameterised in terms of temperature. The melt and runoff model is based on the positive degree-day method and is identical to the recalibrated version as described in Janssens and Huybrechts (2000). It takes into account the process of meltwater retention by refreezing and capillary forces in the snowpack. This method to calculate the melt has been shown to be sufficiently accurate for most practical purposes. It moreover ensures that the calculations can take place on the detailed grids of the ice-sheet models so that one can properly incorporate the feedback of local elevation changes on the melt rate, features which cannot be represented well on the generally much coarser grid of a climate model. The melt model is also implemented for Antarctica, but since current summer temperatures remain generally below freezing, melt amounts are negligible. Because of their very low surface slopes, it is further assumed that meltwater produced on the surface of the Antarctic ice shelves, if any, refreezes in situ at the end of the summer season, and therefore does not escape to the ocean. Below the ice shelves, a uniform melting rate is applied which magnitude is linked to the heat input into the cavity, as explained further below.

2.7. Coupling of AGISM with ECBilt–CLIO–VECODE

The interactions between the different components of LOVECLIM and, in particular, between AGISM and ECBilt–CLIO–VECODE are illustrated in Figure 2. The key atmospheric variables needed as input for AGISM are surface temperature and precipitation. Because the details of the Greenland and Antarctica surface climates are not well captured on the coarse ECBilt grid, these boundary conditions consist of present-day observations as represented on the much finer AGISM grid onto which climate-change anomalies from ECBilt are superimposed. Monthly temperature differences and annual precipitation ratios, computed against a reference climate corresponding to the period 1970–2000, are interpolated from the ECBilt grid onto the AGISM grid and added to and multiplied with the observed surface temperatures and precipitation rates, respectively. The oceanic heat flux at the base of the Antarctic ice shelves is also calculated in perturbation mode using the parameterisation proposed by Beckmann and Goosse (2003).

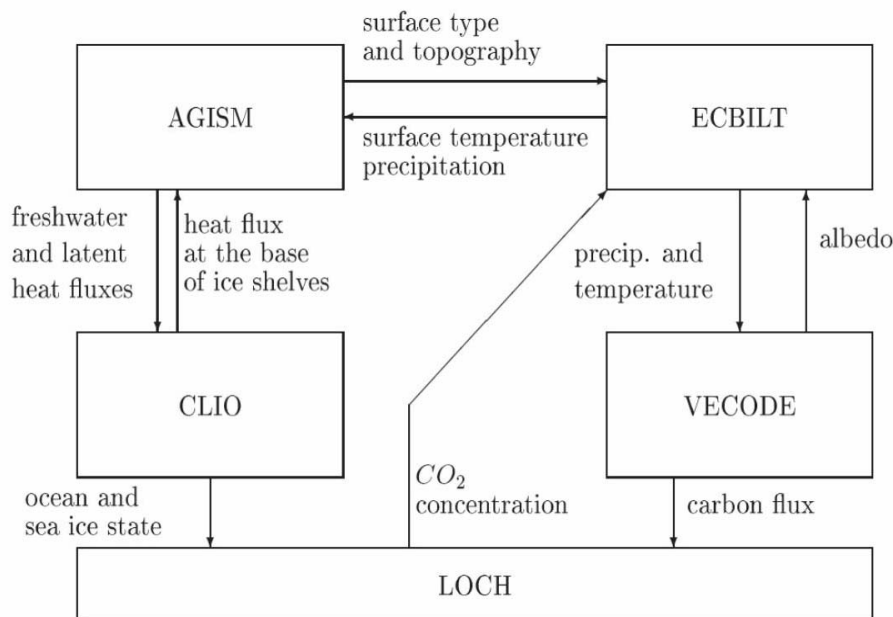


Figure 2: Sketch of the interactions between the various components of LOVECLIM. The interactions between ECBilt and CLIO are not represented in order to keep the figure simple. The following variables are exchanged between these two models: the surface wind stress, the surface heat and freshwater fluxes, the sea-surface temperature, the surface albedo and the thicknesses and concentrations of sea ice and snow.

After performing mass-balance and ice-dynamics computations, AGISM passes the calculated changes in land fraction covered by ice and orography to ECBilt and VECODE. In addition AGISM provides CLIO with the geographical distribution of the

annual mean freshwater flux resulting from ice-sheet runoff, iceberg calving, runoff from ice-free land and basal ice melting (Figures 3 and 4).

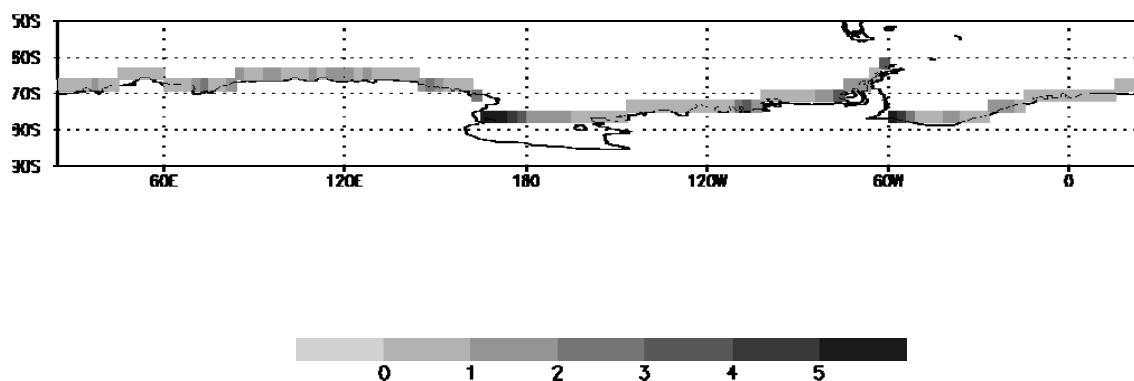
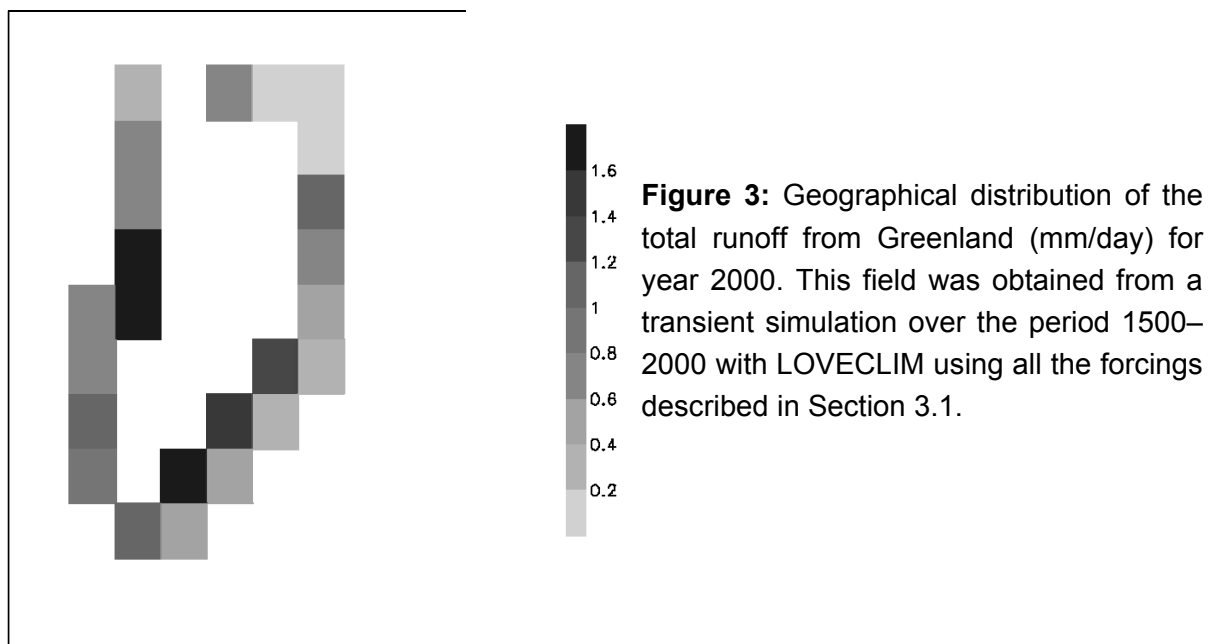


Figure 4: Geographical distribution of the total runoff from Antarctica (mm/day) for year 2000. This field was obtained from a transient simulation over the period 1500–2000 with LOVECLIM using all the forcings described in Section 3.1.

The transfer of data from AGISM to ECBilt is rather straightforward since the grid cells of ECBilt are much larger than the AGISM ones. Each AGISM grid cell is associated with an ECBilt grid cell, and an area average is made to determine the value of a specific variable on the ECBilt grid. For the interpolation of data from the ECBilt grid to the AGISM grid, we opted to first transform the AGISM points on the

ECBilt grid and subsequently apply a Lagrangian interpolation. The selected interpolation is a third-order Lagrange's polynomial. Four ECBilt grid points are taken into account in latitude and four in longitude to determine the polynomial providing the variable value at each particular AGISM grid point. Regarding the coupling between AGISM and CLIO, a simple procedure was set up to allocate the total freshwater flux from AGISM to the respective surface oceanic grid boxes of CLIO that border Greenland and Antarctica. It must also be mentioned that the latent heat associated with iceberg melting is pumped from these grid boxes.

The coupling technique described above leads to heat and water losses/gains in the coupled model. Due to the perturbation method employed and the use of a Lagrangian interpolation, the amount of water received by AGISM in the form of precipitation is not equal to the amount of water leaving ECBilt. Similarly, the heat available in ECBilt for the ice-sheet melting differs from the one in AGISM. Flux adjustments are therefore necessary to ensure strict conservation of heat and water. These are applied uniformly in a given oceanic area around each ice sheet. The water correction is treated as an additional freshwater flux and the heat correction as an additional latent heat flux associated with iceberg melting.

2.8. Global glacier-melt algorithm

The response of mountain glaciers and ice caps is accounted for by a global glacier-melt algorithm (Raper and Braithwaite, 2006). The algorithm is run in off-line mode and consists of a mass balance and a geometric glacier model. A separation is made between melt contributions from mountain glaciers and ice caps, as these have distinctly different geometric characteristics. The algorithm also has an improved treatment of volume shrinkage to take into consideration simultaneous changes in glacier area. This allows glaciers to reach a new equilibrium under climate warming, contrary to older models which use a time-constant sensitivity for mass balance, so that glaciers would melt away for any warming rather than approaching a new equilibrium (e.g., Gregory and Oerlemans, 1998; van de Wal and Wild, 2001).

The glacier- and ice-cap-melt algorithm works on glacier areas within a regular 1° grid (Raper and Braithwaite, 2005), for which size distributions of glacier area and volume have been made using scaling relationships (Bahr et al., 1997). The glacier areas do not include glaciers and ice caps around the Greenland and Antarctic ice sheets as these are already accounted for in AGISM. The mass-balance part of the model calculates mass-balance profiles for each grid cell with a degree-day model (Braithwaite et al., 2002). This is first done for seven regions with good glacier-inventory data to estimate the elevation of the average equilibrium line altitude (ELA), and is subsequently extrapolated to other regions. The profiles are approximated with two segments representing linear gradients of mass balance versus altitude in the

accumulation and ablation areas, respectively (Figure 5, left panel). The resulting balance gradients were regressed on annual precipitation and summer temperature from a gridded climatology to obtain mass-balance profiles over all other grid cells with glaciers.

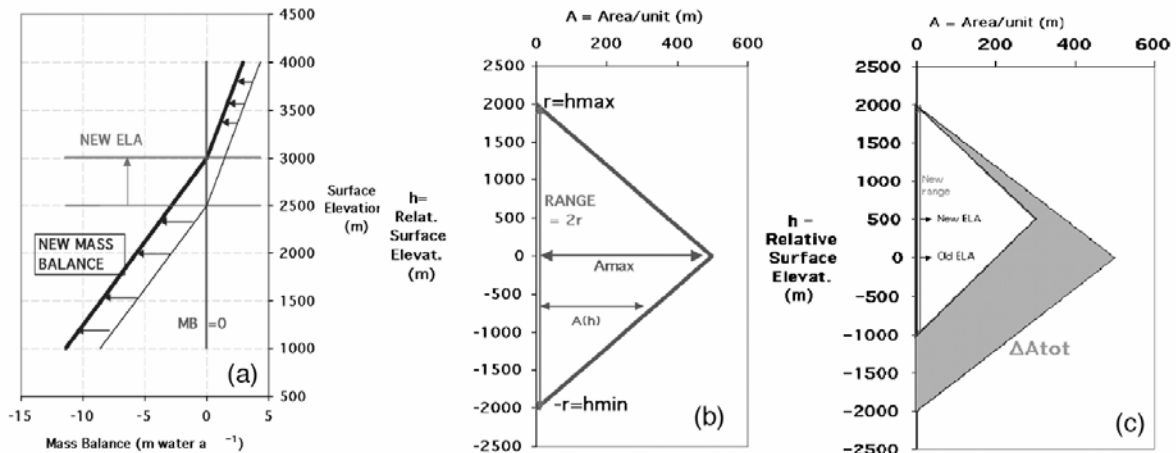


Figure 5: Aspects of the structure of the global glacier-melt algorithm. (a) The mass-balance profile relative to the ELA is represented by two linear segments; depending on the climate regime, balance gradients can vary by a factor of 10. (b) The hypsometry of mountain glaciers is represented by triangular shapes. (c) In a warmer climate, the glacier loses its area at the base.

The geometric part of the model (Raper et al., 2000) assumes that the hypsometry (area-elevation distribution) of mountain glaciers can be approximated by a triangular shape defined by the altitude range (minimum to maximum altitude) and the mean altitude where the glacier is widest (Figure 5, middle panel). For ice caps, a parabolic shape is supposed with a circular base. The altitude range of mountain glaciers and ice caps was estimated from a roughness characteristic derived from high-resolution topographic data using a linear regression equation calibrated with data from the seven regions where altitude ranges are known. The symmetry of the triangles is not affected by a temperature change. The glacier loses its area by increasing its minimum elevation followed by a proportional reduction of the glacier area over the total new range (Figure 5, right panel).

The algorithm is forced by applying annual temperature anomalies with respect to the 1961–1990 period. Precipitation changes are not considered in line with conclusions from several studies showing this to be of secondary importance (Braithwaite et al., 2002; van de Wal and Wild, 2001). Prior to forcing with any given climate scenario, all ELAs need to be slightly adjusted to make the model fit the

estimated global glacier mass balance of $-0.130 \pm 0.033 \text{ m yr}^{-1}$ for the 1961–1990 reference period (Raper and Braithwaite, 2006).

3. MODELLING THE EVOLUTION OF CLIMATE, SEA LEVEL AND CARBON CYCLE DURING THE LAST FEW CENTURIES

In order to assess the performance of LOVECLIM, a series of climate-change experiments covering the last 500 years were carried out with this model.

3.1. Forcings

Both natural and anthropogenic forcings were taken into account in those simulations. The forcings included were:

- *The variations in solar irradiance.* The evolution of solar irradiance followed the reconstruction of Lean et al. (1995) extended back in time by Bard et al. (2000) (Figure 6).
- *The volcanic activity.* The effect of volcanism was derived from Crowley (2000) and was incorporated through changes in solar irradiance (Figure 7).
- *The increase in tropospheric ozone concentration.* This forcing was applied to both shortwave and longwave fluxes as a time-varying external radiative forcing (different in each hemisphere), using values deduced from Bernsten et al. (2000) (Figure 8).
- *The increase in sulphate-aerosol load.* Only the direct effect of sulphate aerosols was considered. This effect was accounted for through a modification of the surface albedo (Charlson et al., 1991), the spatio-temporal distribution of the change being derived from Boucher and Pham (2002).
- *The increase in greenhouse-gas concentrations.* The observed evolution of 19 well-mixed greenhouse gases was prescribed according to Houghton et al. (2001) (Figure 9). Note that the atmospheric CO₂ concentration can also be modelled interactively. In this case (prognostic atmospheric CO₂), the anthropogenic fluxes to the atmosphere included fossil fuel emissions from Marland et al. (2003) and, if appropriate, the emissions from land-use change as reconstructed by Houghton and Hackler (2002) (Figure 10). A second scenario of total anthropogenic emissions provided by the Bern climate-carbon-cycle model (Bern-CC; Joos and Bruno, 1996) was utilised in some experiments (see Figure 10).

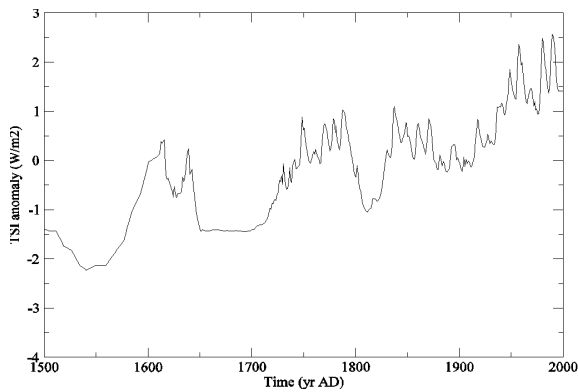


Figure 6: Variations in solar irradiance according to Bard et al. (2000) until 1610 AD and Lean et al. (1995) thereafter. The values have to be divided by 4 to obtain a quantity in $W m^{-2}$ at the top of the Earth’s atmosphere.

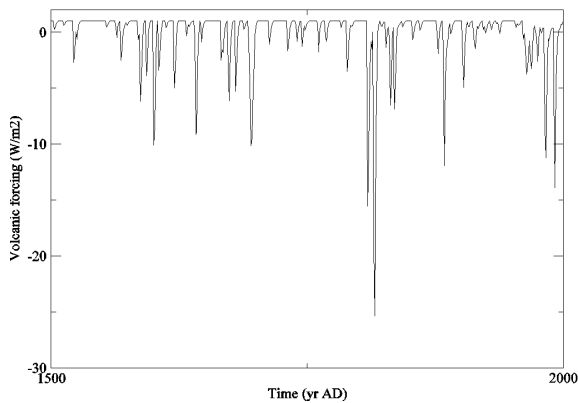
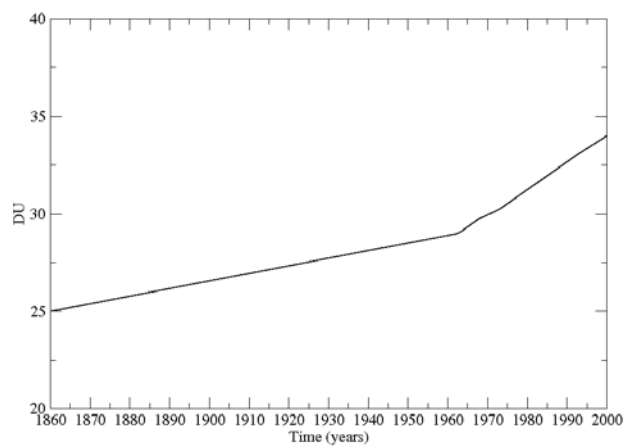


Figure 7: Global mean radiative forcing associated with volcanic activity (expressed in terms of solar irradiance anomaly) according to Crowley (2000). The values have to be divided by 4 to obtain a quantity in $W m^{-2}$ at the top of the Earth’s atmosphere.

Figure 8: Increase in globally averaged ozone abundance (DU) as obtained by applying a linear interpolation in time to Houghton et al.’s (2001) data.



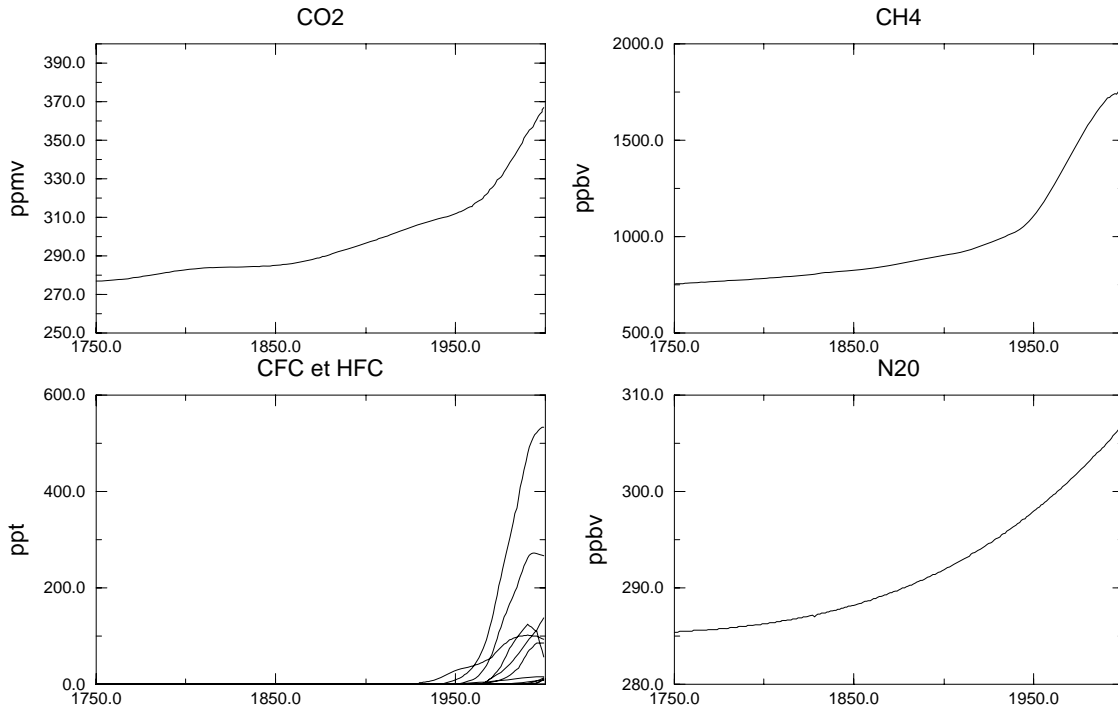


Figure 9: Changes in greenhouse-gas concentrations over the period 1750–2000 AD according to Houghton et al. (2001).

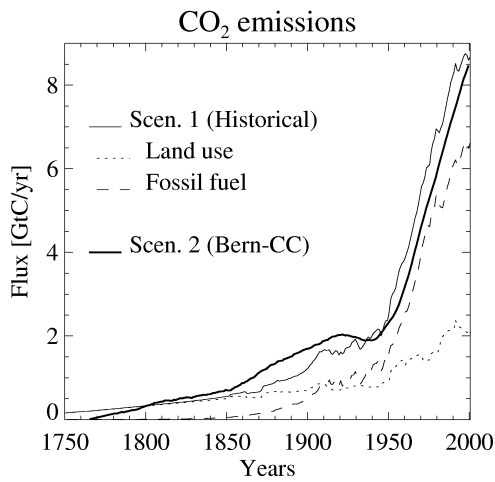


Figure 10: Anthropogenic CO₂ emissions from 1750 to 2000 AD. Fossil fuel burning data (dashed) from Houghton and Hackler (2002) added to the land-use values (dotted) from Marland et al. (2003) result in the thin solid curve. A second scenario (Bern-CC) is represented by the thick solid line.

- **Deforestation.** This forcing was implemented by assuming that the cropland fraction in each grid cell as given by Ramankutty and Foley (1999) represents the fraction of trees that has to be replaced by grass. It was not considered when land-use emissions were included in the anthropogenic fluxes (as in Figure 10).

3.2. Experimental design

An ensemble of five experiments was performed with the model. Ensemble simulations are multiple integrations using identical forcings but different initial conditions. They provide estimates of the variability of the response of a given model. Furthermore, the natural climate variability can be smoothed by averaging the different elements of the ensemble in order to obtain a better measure of the forced response of the system. The initial conditions were taken from model states at different times of a pre-industrial equilibrium control run (hereafter referred to as CTL). Several studies have demonstrated that the starting year of model integration can have a rather long-term impact on the simulated climate, especially in the Southern Ocean area (e.g., Fichefet and Tricot, 1992; Goosse and Renssen, 2005). According to those studies, it is necessary to begin the simulations at least two centuries before the period of interest in order to remove this influence. Here, we chose to start the experiments in AD 1500 and to analyse the model results over the period 1700–2000 AD. The initialization of AGISM is discussed in Section 3.3.2.

The equilibrium climate which served as initial condition for the experiments was obtained by constraining LOCH and VECODE with an atmospheric CO₂ concentration of 280 ppmv. Moreover, as the large turnover time of the ocean implies a long adjustment time of the oceanic carbon cycle, LOCH was first equilibrated off-line by forcing it with a 50-yr average of the dynamic fields of CLIO and ECBILT. Some parameters of LOCH also needed to be adjusted in the process. For instance, the constant used for computing the gas-exchange rate has been tuned in such a way that the gross air–sea CO₂ flux is close to 84 GtC yr⁻¹ during pre-industrial times.

3.3. Results

3.3.1. Climate

In this section and the following one, we briefly discuss results from runs in which the evolutions of the atmospheric CO₂ concentration and cropland fraction were prescribed. Over the last 140 years, the model simulates a global surface warming ranging from 0.33°C to 0.43°C, with a mean value of 0.38°C (Figure 11). This value is about 0.15°C lower than the observed one (Jones and Moberg, 2003; Rayner et al., 2003). LOVECLIM therefore tends to underestimate the global increase in surface temperature observed over the last century. This is not surprising as the sensitivity of this model to a CO₂ doubling (i.e. the globally averaged, annual mean surface temperature response at equilibrium to a doubling of the atmospheric CO₂ concentration) amounts to 1.7°C, which is at the lower end of the range of current estimates (Houghton et al., 2001).

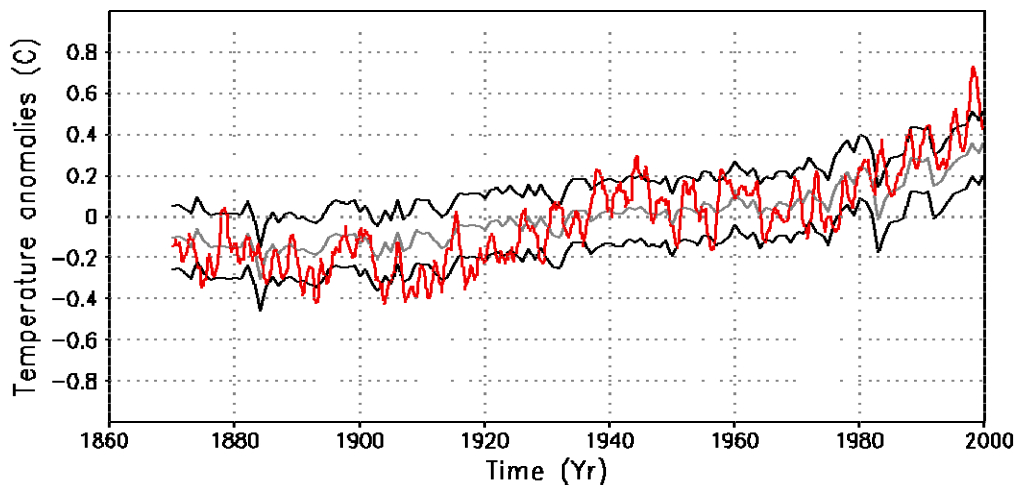


Figure 11: Globally averaged, annual mean surface temperature anomalies (in °C) over 1870–2000 AD. The reference period for the computation of the anomalies is 1870–2000 AD. The grey curve is the model ensemble mean, the black curves represent the ensemble mean plus and minus two standard deviations and the red curve corresponds to the observations of Jones and Moberg (2003) and Rayner et al. (2003).

During some time periods, the observation curve in Figure 11 is outside the modelled two-standard-deviation interval. In particular, LOVECLIM fails in reproducing the rapid warming observed during the last few decades as well as the coldest and warmest periods present in the observational record.

Over the last 300 years, the Northern Hemisphere averaged, annual mean surface temperature anomalies simulated by the model compare reasonably well with those reconstructed by Mann and Jones (2003). From Figure 12, it can be seen that the reconstruction always stays within the modelled two-standard-deviation interval. The overall warming depicted by the ensemble mean appears however slightly underestimated compared to the one obtained by Mann and Jones (2003). Nevertheless, it is worth mentioning that one particular simulation shows an increase in temperature comparable to the one found in the reconstruction.

Because of its coarse resolution and the simplifications made in its atmospheric component, LOVECLIM generally perform better at mid- and high latitudes than in the equatorial and tropical regions. As in many other models, the response of this particular model to a global perturbation (e.g., an increase in greenhouse-gas concentrations) is enhanced in polar regions due to a number of feedback mechanisms involving the cryosphere (e.g., Holland and Bitz, 2003). In all our ensemble members, the surface warming at 80°N is about 4 times larger than the globally averaged warming, while in the 2×CO₂ experiments discussed in Holland

and Bitz (2003), the models simulate at this latitude an increase in surface temperature from 1.8 to 3.1 times the global mean warming (these figures can be compared together since the warming patterns are more or less identical at the end of our simulations and in $2\times\text{CO}_2$ experiments with LOVECLIM). This strong polar amplification in LOVECLIM is caused by too weak a response of the model at low latitudes, as illustrated in Figures 13 and 14.

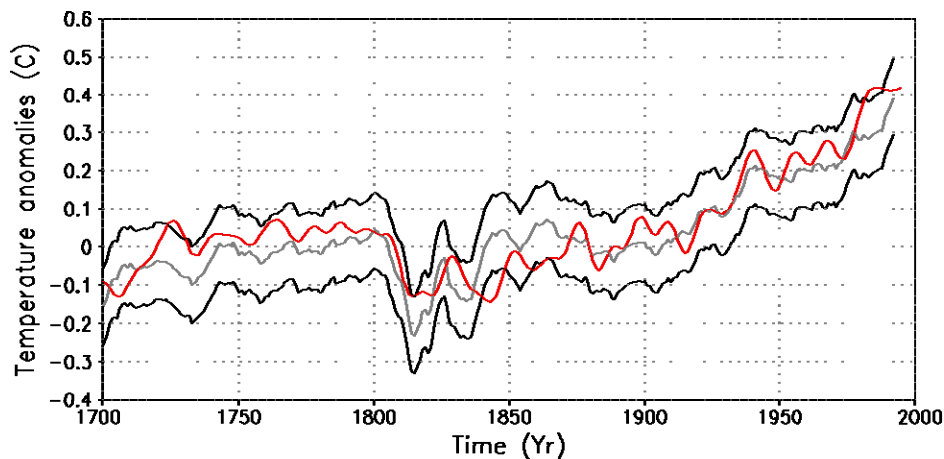


Figure 12: Annual mean surface temperature anomalies (in °C) averaged over the Northern Hemisphere during 1870–2000 AD. The reference period for the computation of the anomalies is 1500–1992 AD. The grey curve is the model ensemble mean, the black curves represent the ensemble mean plus and minus two standard deviations and the red curve corresponds to the reconstruction of Mann and Jones (2003). A 11-yr running average has been applied to the time series in order to highlight low-frequency variations.

These figures show that the model behaves relatively well at mid- and high latitudes. By contrast, at low latitudes, the agreement between the model results and observational estimates is less good, especially in the Southern Hemisphere. In these low-latitude regions, the model significantly underestimates the warming observed during the last few decades. Furthermore, in the Southern Hemisphere (Northern Hemisphere), the standard deviation of the temperature data is 2.6 (1.5) times larger than the modelled one over the period 1870–1950 AD. Also, the model intercomparison conducted by Brovkin et al. (2006) reveals that LOVECLIM is much less sensitive to the deforestation forcing between 30° N and 30° S than the majority of Earth system models of intermediate complexity (EMICs). Figure 15 demonstrates that, if we artificially increase the standard deviation of the simulated temperature time series as in Goosse et al. (2005) in order to have the same standard deviation as the dataset, the model results improve considerably.

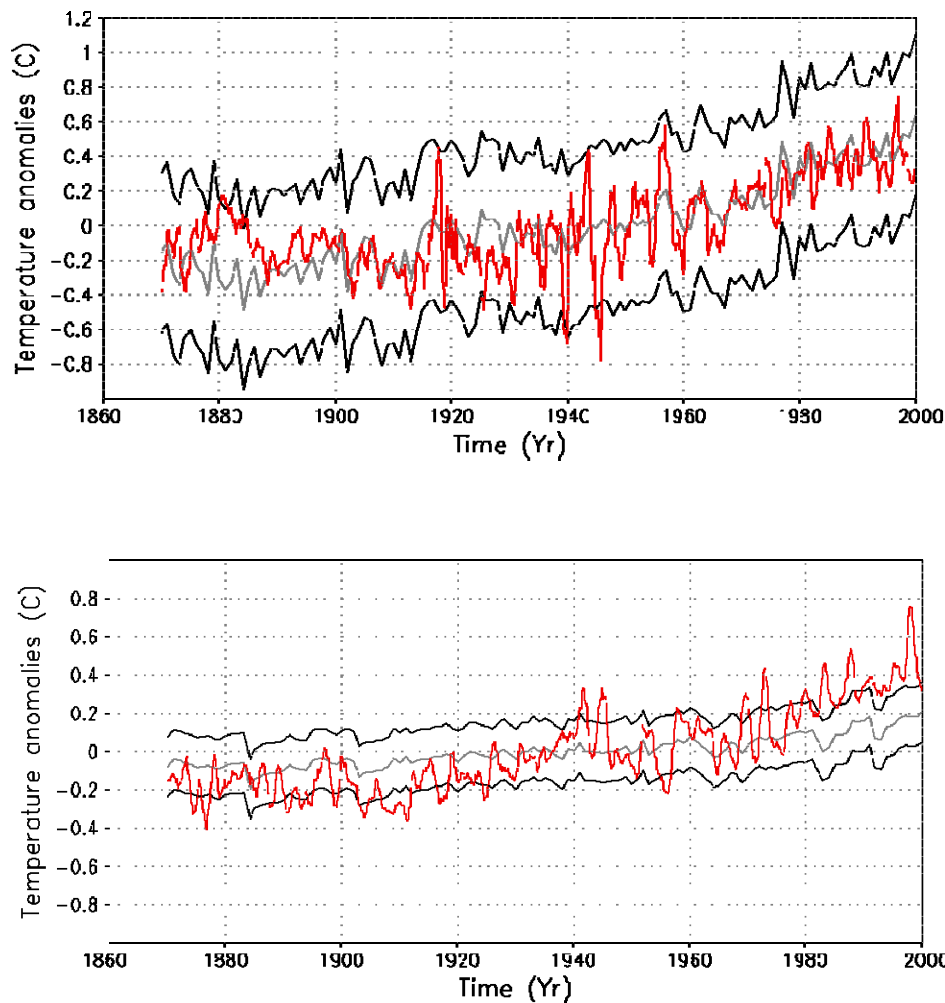


Figure 13: Zonally averaged, annual mean surface temperature anomalies (in °C) for the latitudinal bands 90° – 45° S (top) and 45° – 0° S (bottom) over 1870–2000 AD. The reference period for the computation of the anomalies is 1870–2000 AD. The grey curve is the model ensemble mean, the black curves represent the ensemble mean plus and minus two standard deviations and the red curve corresponds to the observations of Jones and Moberg (2003) and Rayner et al. (2003).

From this analysis, we can conclude that most of the discrepancies noticed at the global scale between the model results and observations are, to a large extent, due to an underestimation of the model variability/response at low latitudes, which is caused by the coarse resolution of the model and the simplified representation of the atmospheric dynamical and physical processes. We can nevertheless trust the model behaviour at mid- and high latitudes.

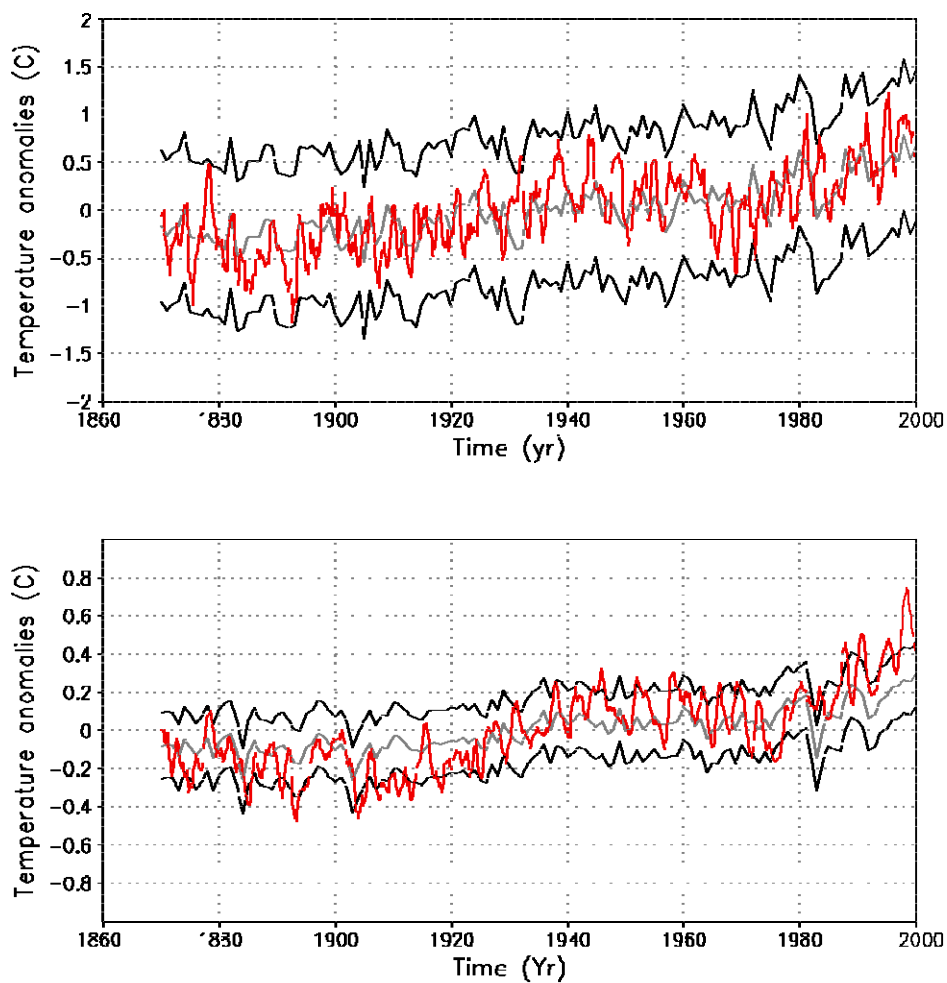


Figure 14: Zonally averaged, annual mean surface temperature anomalies (in °C) for the latitudinal bands 90° – 45° N (top) and 45° – 0° N (bottom) over 1870–2000 AD. The reference period for the computation of the anomalies is 1870–2000 AD. The grey curve is the model ensemble mean, the black curves represent the ensemble mean plus and minus two standard deviations and the red curve corresponds to the observations of Jones and Moberg (2003) and Rayner et al. (2003).

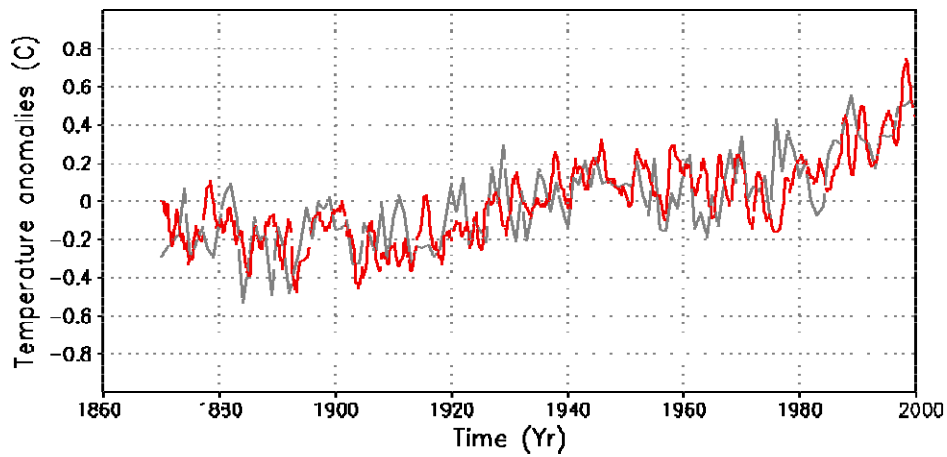


Figure 15: Zonally averaged, annual mean surface temperature anomalies (in °C) for the latitudinal band 45° – 0° N over 1870–2000 AD. The reference period for the computation of the anomalies is 1870–2000 AD. The grey curve represents the model results for a particular simulation (n^3) scaled by a factor 1.5 in order to have the same standard deviation as in the real world and the red curve corresponds to the observations of Jones and Moberg (2003) and Rayner et al. (2003).

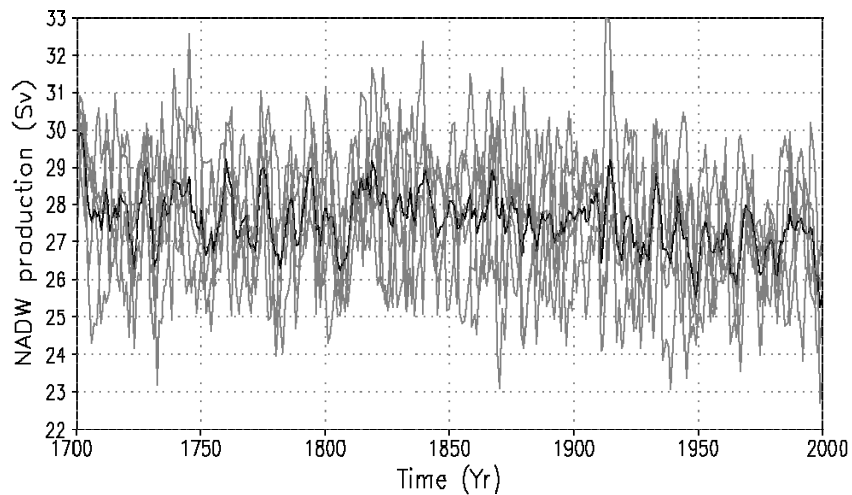


Figure 16: Evolution over the last 300 years of the maximum value of the annual mean meridional overturning streamfunction below the surface layer between 45° and 75° N in the model Atlantic basin. The grey curves correspond to the ensemble members and the black curve is the ensemble mean.

Figure 16 illustrates the evolution over the last 300 years of the maximum value of the annual mean meridional overturning streamfunction in the Atlantic basin, which

an index of the MOC intensity. In accordance with other modelling studies (e.g., Dixon and Lanzante, 1999; Houghton et al., 2001; Latif et al., 2004), a weakening of the MOC of about 1 Sv ($1 \text{ Sv} = 10^6 \text{ m}^3 \text{ s}^{-1}$) is simulated during the industrial era. This feature is associated with a decrease of convection depth in the Norwegian and Labrador Seas. Regarding the production rate of Antarctic bottom water (AABW), it experiences a decrease of about 2 Sv over the same time period (Figure 17). However, the export of this water mass into the Atlantic basin undergoes nearly no change. This reduced AABW formation is related to a slight weakening of the convection activity in the Bellingshausen–Amundsen Seas and in the Indian sector of the Southern Ocean.

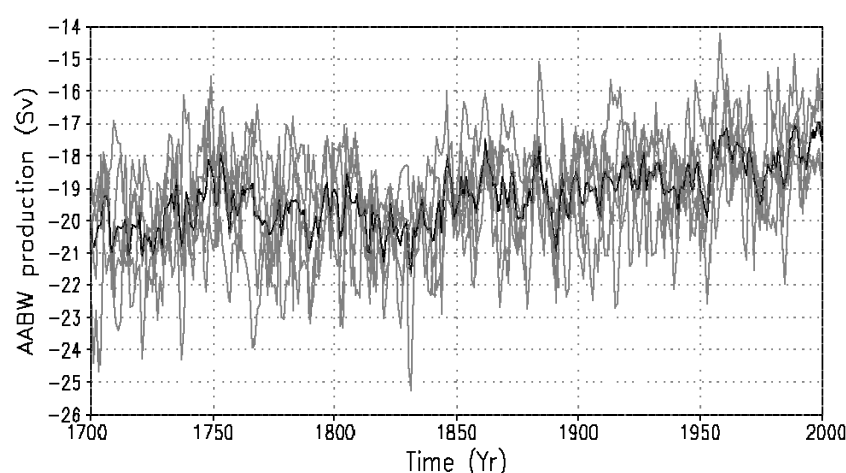


Figure 17: Evolution over the last 300 years of the minimum value of the annual mean meridional overturning streamfunction below the surface layer in the Southern Ocean, which is an index of the production rate of Antarctic bottom water. The grey curves correspond to the ensemble members and the black curve is the ensemble mean.

We refer the reader to Driesschaert (2005) for further details on the simulated climate.

3.3.2. Ice sheets, glaciers and sea level

Because of the long response time-scales associated with polar ice-sheet evolution (of the order of thousands of years and longer), it is necessary to start the calculations early enough in the past to assess the current ice-sheet evolution that would occur irrespective of any future anthropogenic forcing. To that end, both GISM and AISM were first run over the last few glacial cycles. The model forcing was derived from recent ice-core and sediment-core records. For Greenland, temperature and precipitation changes were prescribed from a synthesized climate record

assembled from the GRIP $\delta^{18}\text{O}$ record for the last 100 kyr and the Vostok δD record for the period older than 100 kyr to circumvent known defects with the Greenland data during the Eemian (Huybrechts, 2002). Sea-level changes were prescribed from a linear scaling of the SPECMAP stack such that the maximum sea-level depression is -130 m at 19 kyr BP and $+6$ m during the last interglacial at 122 kyr before present (BP). GISM was run over the last two glacial cycles under these forcing conditions. The same SPECMAP stack also served to prescribe sea-level changes for AISM, with temperature and precipitation changes coming from the Vostok deuterium record for the last four glacial cycles. Basal melting below the ice shelves was forced to follow the temperature forcing with the parameterisation given in Huybrechts (2002) for a reference value of 0.25 m yr^{-1} for present conditions.

The initialization experiments were first conducted on grid of 20-km resolution to save on computer time. At the time of the Last Glacial Maximum (LGM; 18 kyr BP), all relevant data were interpolated on the final 10-km resolution grid for the subsequent simulation of the glacial-interglacial transition and of the Holocene. After year 1500 AD, the forcing came from direct interaction with LOVECLIM according to the data described in Section 3.1. Two more experiments were conducted over the period 1500–2000 AD to assess the impact of the forcing as provided by LOVECLIM. These either kept the forcing fixed at year 1500 AD or continued the ice-core and sediment-core proxy forcing for the last 500 years in stand-alone mode. Those results are not discussed in detail here, but enable to distinguish the response arising from contemporary or past climatic forcing, and bring to light the quality of LOVECLIM forcing as compared to direct forcing from ice core proxy records. LOVECLIM experiments beyond 1500 AD did not consider variable sea-level forcing. Although sea-level change is an intrinsic output of the model and could therefore be applied in an internally consistent way, this option was not pursued further as the forcing is deemed small compared to the last 20,000 years.

For the Greenland ice sheet, we find a slightly increasing ice volume during the period 1700–2000 AD (Figure 18). This trend is largely explained as a residual response to the late Holocene forcing, in particular to the Little Ice Age cooling after year 1500 AD. The effect is not particularly large, however, amounting to only 1.2 cm of global sea-level rise over the entire period. The growing trend stabilizes during the 20th century, with almost no net effect on ice volume. Only during the last decades of the 20th century, the ice volume starts to decrease in response to the imposed warming. The latter volume changes are predominantly driven by an increase in ice melt and runoff (see lower panel of Figure 18) that ultimately becomes slightly larger than the flux from iceberg calving. For all of the historical period, the annual accumulation is nearly balanced by runoff and iceberg calving, roughly in equal shares, in full agreement with available field data (Reeh, 1999).

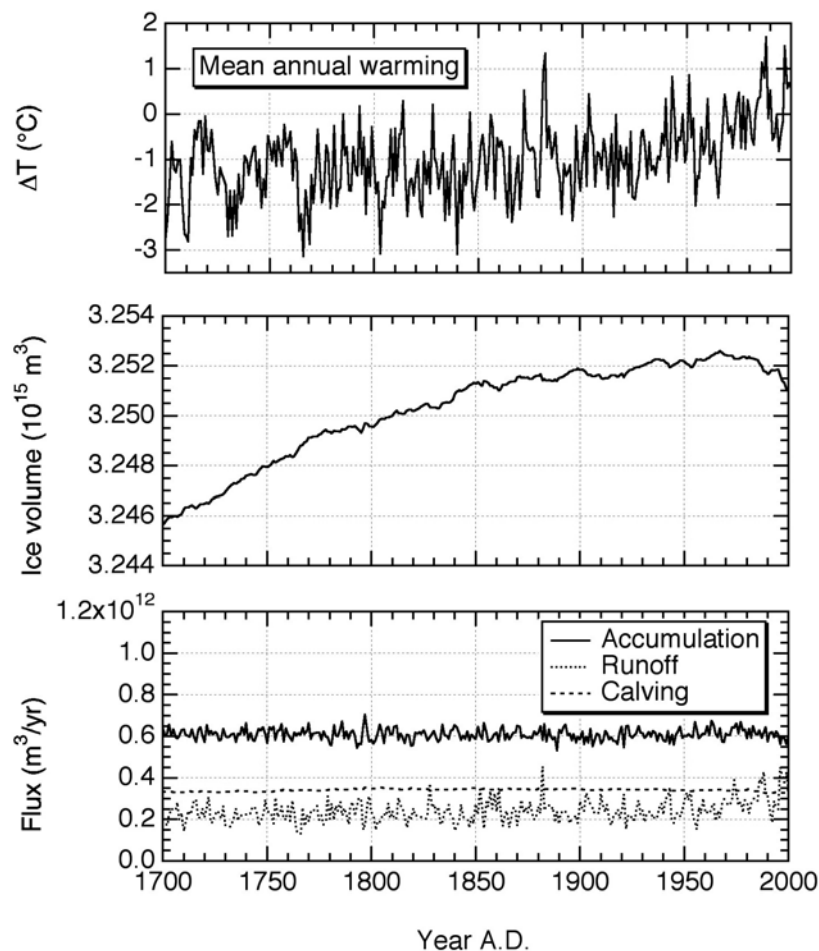


Figure 18: Evolution of Greenland temperature forcing, ice volume and mass-balance components over the period 1700–2000 AD.

For the period between 1700 and 2000 AD, the environmental forcing equally shows little trend over Antarctica (Figure 19). Despite a late 20th century warming of perhaps 1°C, defined here as the mean annual warming over the grounded ice-sheet proper, there are no clear trends in both the accumulation rate of snow and the basal melting rate below the surrounding ice shelves. These two mass-balance components represent the main forcing as surface runoff is negligibly small owing to the low surface temperatures over Antarctica even during the summer months. Nevertheless, we find the Antarctic ice sheet to be retreating slowly at a rate equivalent to a global sea-level rise of about 1.7 cm during the 20th century. This evolution is mostly due to the long-term background trend of +2.6 cm, mitigated by about 0.9 cm from slightly rising accumulation rates over the same period. These results agree well with similar experiments performed under IPCC forcing (Huybrechts et al., 2004). The ongoing dominance of past climatic changes on the contemporary ice-sheet evolution is a fine illustration of the inertia encountered when

studying the response of large continental ice sheets. In this case, it is mainly due to ongoing grounding-line retreat in West Antarctica following rising sea levels since the LGM.

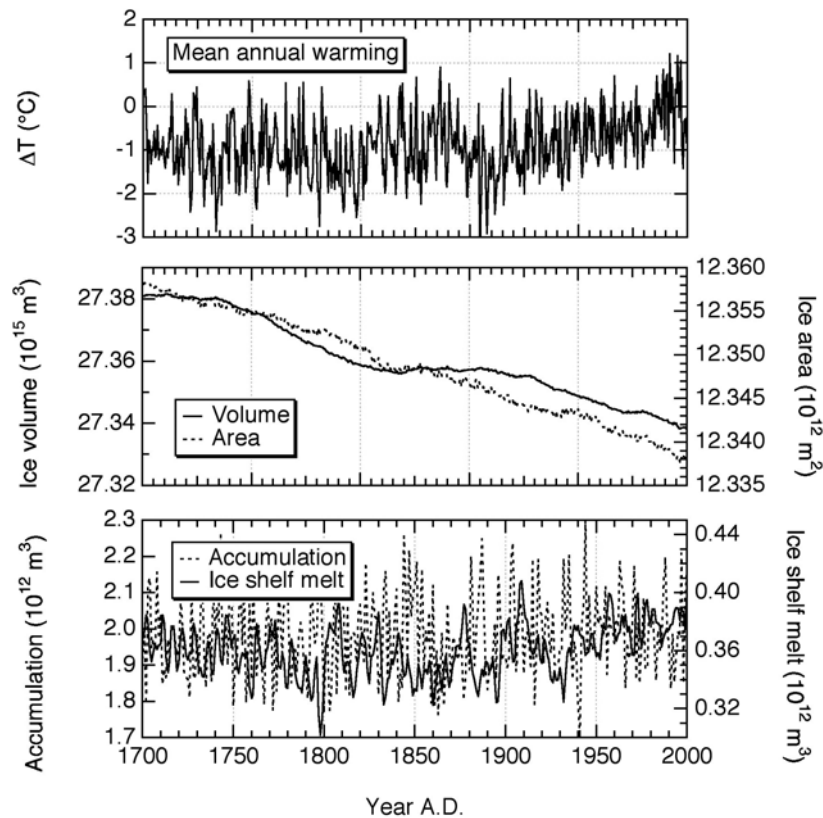


Figure 19: Evolution of Antarctic temperature forcing, ice volume and ice area, and mass-balance components over the period 1700–2000 AD.

The evolution of mountain glaciers and small ice caps as calculated in off-line mode is shown in Figure 20. The mean annual temperature over grid boxes containing either small ice caps or mountain glaciers is found to rise by about 1°C over the 20th century, most of it during the last two decades. These warmings are about double the global mean in accordance with the more poleward position of these ice bodies and the substantial polar temperature amplification in LOVECLIM (see Section 3.3.1). The interannual variability is largest over the small ice caps as these represent a more limited circum-arctic geographical zone in the Northern Hemisphere, characterized by more in-phase temperature variations. For the grid boxes over mountain glaciers, the variability is dampened by regional variations in the interannual variability as these grid boxes have a much larger geographical spread and can be found in both hemispheres.

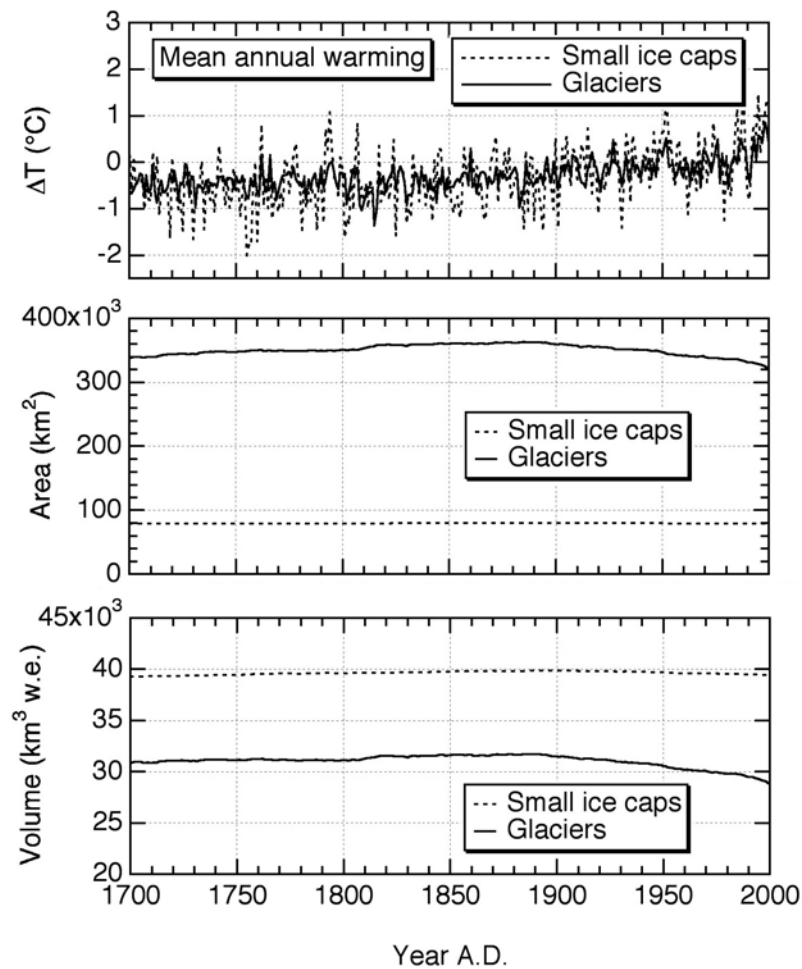


Figure 20: Evolution of mountain glaciers and small ice caps over the period 1700–2000 AD.

Global glacier area and volume are found to reach a maximum in the late 19th century corresponding to the Little Ice Age, but this maximum and the ensuing 20th century glacier retreat are not very pronounced. Over the last hundred years, the model predicts an ice loss equivalent to only 0.89 cm of sea-level rise. This value is at the lower end compared to other assessments (Church et al., 2001). One reason is the low total ice volume assumed by the algorithm of about $4 \times 10^4 \text{ km}^3$ for ice caps and $3 \times 10^4 \text{ km}^3$ for mountain glaciers (Raper and Braithwaite, 2005). That corresponds to about 20 cm of total sea-level rise, a factor 2.5 less than previous estimates which however included small ice bodies around the Greenland and Antarctic ice sheets (Church et al., 2001). A second reason is the prescribed global ice mass balance for the 1961–1990 reference period of 0.19 mm yr^{-1} (Raper and Braithwaite, 2006), also at the lower end of other simulations (Meier, 1984; Gregory and Oerlemans, 1998; van de Wal and Wild, 2001).

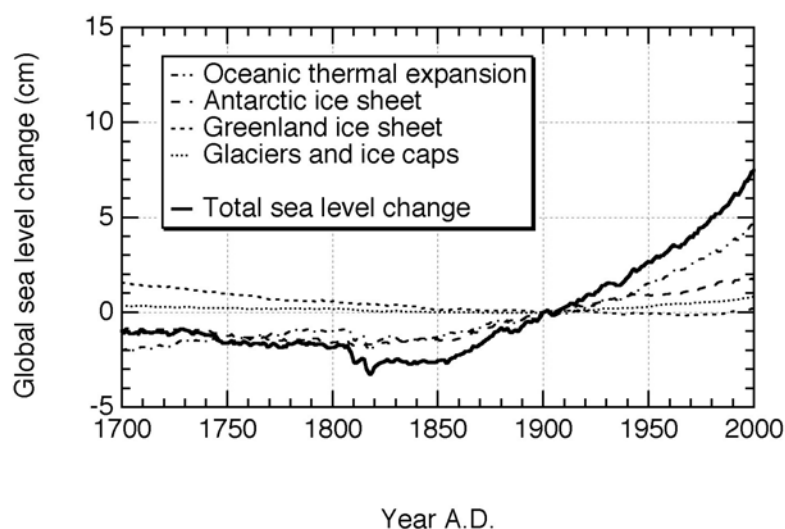


Figure 21: Contributions to global sea-level rise for the period between 1700 and 2000 AD as predicted by LOVECLIM. The reference date is 1900 AD.

The total sea-level rise from all contributions considered in LOVECLIM (ocean thermal expansion, small ice caps and mountain glaciers, Antarctic and Greenland ice sheets) is summarized in Figure 21. For the 20th century, LOVECLIM explains about 7.6 cm of sea-level rise. The bulk of that value, about 4.7 cm, comes from thermal expansion of the World Ocean. The Antarctic and Greenland ice sheets combined lead to a sea-level rise of 2 cm, and glaciers and ice caps are responsible for about 0.9 cm of sea-level rise. These numbers are similar to those that have been derived for the IPCC Third Assessment Report (TAR; Church et al., 2001) for the same components except for the lower glacier contribution as found here. Therefore, our numbers suffer from the same problem as the IPCC TAR estimates in that they are biased low with respect to the observed range of sea-level rise of between 10 and 20 cm for the entire 20th century. A possible explanation for the mismatch is the very large uncertainty on the terrestrial storage term arising from dam building and groundwater mining.

3.3.3. Carbon cycle

Two types of experiments were conducted with the aim of assessing the performance of the carbon-cycle component of LOVECLIM. In a first group, the evolution of the atmospheric CO₂ concentration was prescribed in order to allow the comparison with other modelling studies (e.g., the Ocean Carbon Model Intercomparison Project 2 – OCMIP2) as well as with the results previously obtained with the individual model components. In the second group, the CO₂ abundance was no longer constrained and evolved in response to anthropogenic emissions over the industrial era.

Name	Atm. CO ₂	RF	Biology	LCC	FF flux	LU flux
C_C	Historical	Yes	No	No	-	-
C_O	Historical	No	No	No	-	-
C_B	Historical	Yes	Yes	No	-	-
C_CD	Historical	Yes	No	Yes	-	-
C_D	Constant	No	No	Yes	-	-
E_C	Free	Yes	No	No	Yes	Yes
E_R	Free	No	No	No	Yes	Yes
E_CD	Free	Yes	No	Yes	Yes	No
EC_SP	Free	CO ₂ only	No	No	Yes	Yes

Table 1: Description of the CO₂ experiments performed over the historical period. The atmospheric CO₂ concentration was prescribed in experiments whose names start with a C and followed the reconstruction shown in Figure 9, except for C_D in which the atmospheric CO₂ concentration was kept fixed to its pre-industrial value. Experiments with prognostic atmospheric CO₂ (name starting with E) were run with anthropogenic emissions from fossil fuel burning and land use (FF and LU; columns 6 and 7). Scenario 1 from Figure 10 applied, except for EC_SP which was run under scenario 2 (Bern-CC). The anthropogenic emissions for experiment E_CD only included the fossil fuel contribution as the land-cover change (LCC) scenario from Ramankutty and Foley (1999) (see Section 3.1) was activated. The radiative forcing (RF; column 3), when present, included all contributions given in Section 3.1, except for EC_SP in which the sole contribution from carbon dioxide was considered. Column 4 describes the consideration or not of biological activity in the ocean.

Within each category of experiments, sensitivity analyses were carried out. The impact of processes such as oceanic biological activity, deforestation or radiative forcing were evaluated (the complete details are given in Table 1). In parallel, a control experiment was run with the same duration and initial conditions as individual experiments but in which the pre-industrial forcing conditions prevailed; this control run guarantees that the estimates of carbon fluxes between reservoirs are not affected by residual drift and/or inherent variability. The initial conditions were derived from an equilibrium run which spanned over 2000 years, allowing for the long adjustment times of soils and the deep ocean to the pre-industrial conditions.

Figure 22 displays the annual mean air–sea differences in CO₂ partial pressure as reconstructed by Takahashi et al. (2002) and as obtained in experiment C_B for years 1950 and 2000 AD. Overall, the observed features are reproduced by the model: strong out-gassing in the equatorial regions, uptake in the high-latitude areas and quasi-equilibrium at mid-latitudes. However, several discrepancies exist between the model results and the climatology. Some of these departures do not necessarily indicate a shortcoming in the carbon-cycle model. First, the oceanic surface temperatures and salinities are not identical in the model and in the climatology. Second, the climatology was constructed with the assumption that the oceanic CO₂ pressure at intermediate latitudes (50° S – 45° N) immediately adjusts to the atmospheric CO₂. New analyses indicate that this condition is not met (Takahashi et al., 2006). The strong sink predicted by the model in the Southern Ocean seems, on the contrary, overestimated compared to direct or indirect analyses in that area (Mikaloff Fletcher et al., 2006; Gruber et al., 2006). These local departures do however not necessarily affect the global rate of the CO₂ exchange with the atmosphere.

We present in Table 2 the globally averaged, annual mean values of the net air–sea CO₂ flux for the 1980s and the 1990s for all experiments. The results from experiment C_O may be directly compared to those obtained with a previous version of the model which was run in off-line mode as well as with the OCMIP2 estimates. The figure provided by C_O fall within the range of OCMIP2 estimates. This is in contrast with the number obtained with older versions of CLIO and LOCH that run in uncoupled mode (Matsumoto et al., 2004). The causes for the decrease in the net oceanic uptake when compared to previous results are of multiple origins. Among them are the overestimated convective mixing in off-line runs, the numerical diffusion stemming from the upwind scheme used in previous versions and the fact that the present version of the model exhibits a low response of the deep ocean to atmospheric forcings.

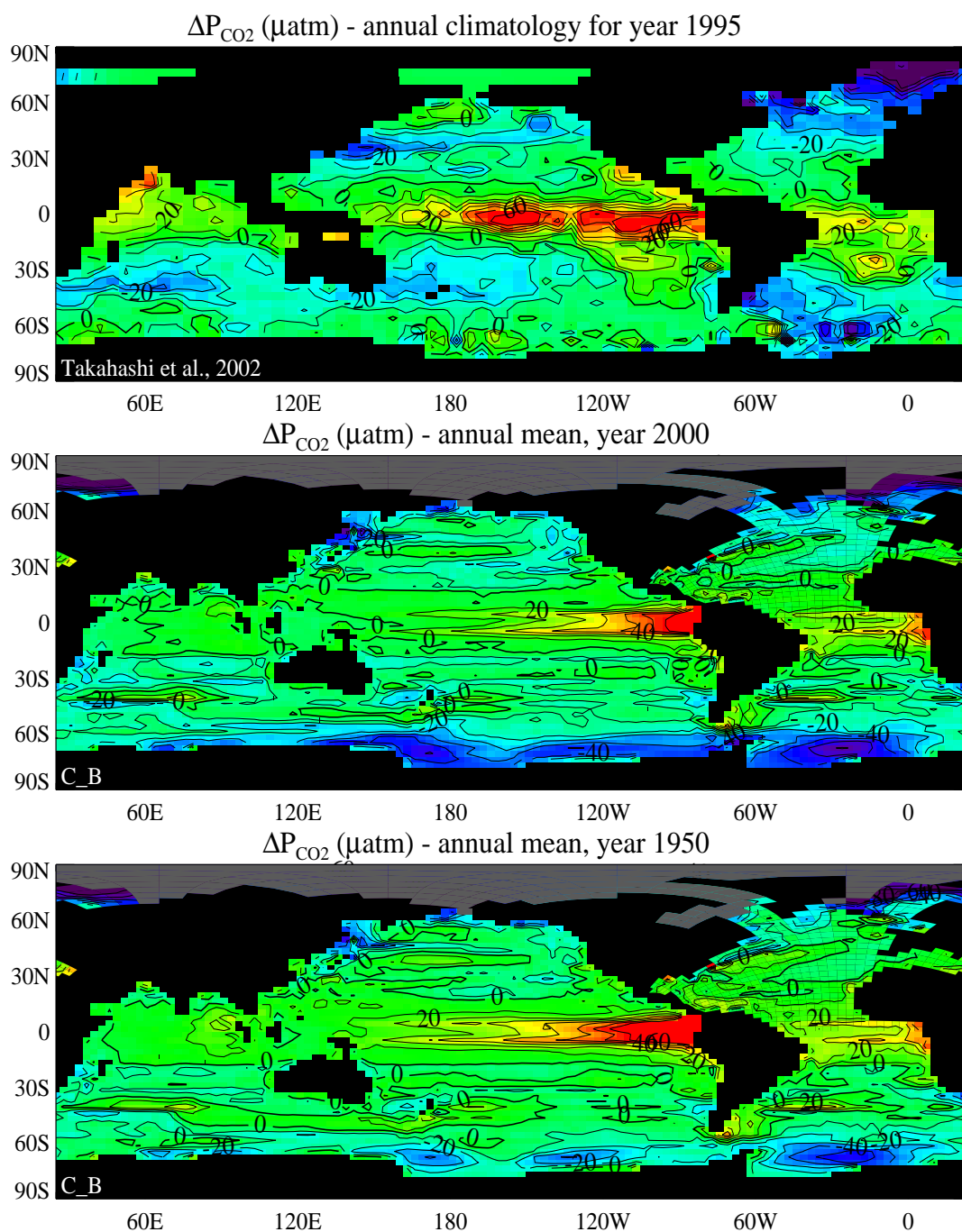


Figure 22: Annual mean air–sea differences in CO₂ partial pressure. The upper panel corresponds to the reconstruction of Takahashi et al. (2002) for year 1995 AD. The lower two panels show the model results for experiment C_B in 2000 and 1950 AD. The colour scale is the same for the three panels: blue and purple indicate CO₂ oceanic sinks, while yellow and red correspond to out-gassing areas. The grey colour indicates areas with permanent sea-ice cover.

Exp.	Year	Atm. CO ₂ μatm	Air–sea flux PgC yr ⁻¹	Air–sea flux PgC yr ⁻¹
		2000	1980–1989	1990–1999
Off-line		369.76	2.52	–
C_C		369.76	1.57	1.80
C_O		369.76	1.64	1.91
C_B		369.76	1.55	1.73
C_CD		369.76	1.56	1.80
E_C		385.04	1.78	2.10
E_R		392.21	1.96	2.41
E_CD		365.82	1.49	1.74
EC_SP		377.98	1.70	1.94
Estimates		369.76	1.56–2.42	1.80–2.80

Table 2: Annual mean atmospheric CO₂ concentrations in 2000 AD and globally averaged net air–sea CO₂ fluxes for the 1980s and 1990s as obtained in the various experiments. The last line gives the corresponding observed and OCMIP2-derived values.

When the evolution of the atmospheric CO₂ concentration is prescribed, the oceanic uptake simulated by the model is in the lower range of current estimates; this is also the case for the oceanic carbon inventory (Figure 23). While the experiment with no climate change exhibits the largest air–sea flux, the differences among the various experiments are smaller than the temporal variability observed within one experiment. Most of the differences between C_B and C_C, which share the same radiative forcing, may be explained by a different initial state, hence a different climate (these differences are clearly evidenced by the terrestrial carbon inventory curves in Figure 23). Biological activity in the ocean does not impact the carbon cycle at this time-scale. Indeed, on the one hand, CO₂ does not influence photosynthesis and, on the other hand, alkalinity in abiotic runs is set so that its surface distribution takes into account the neglect of biological processes.

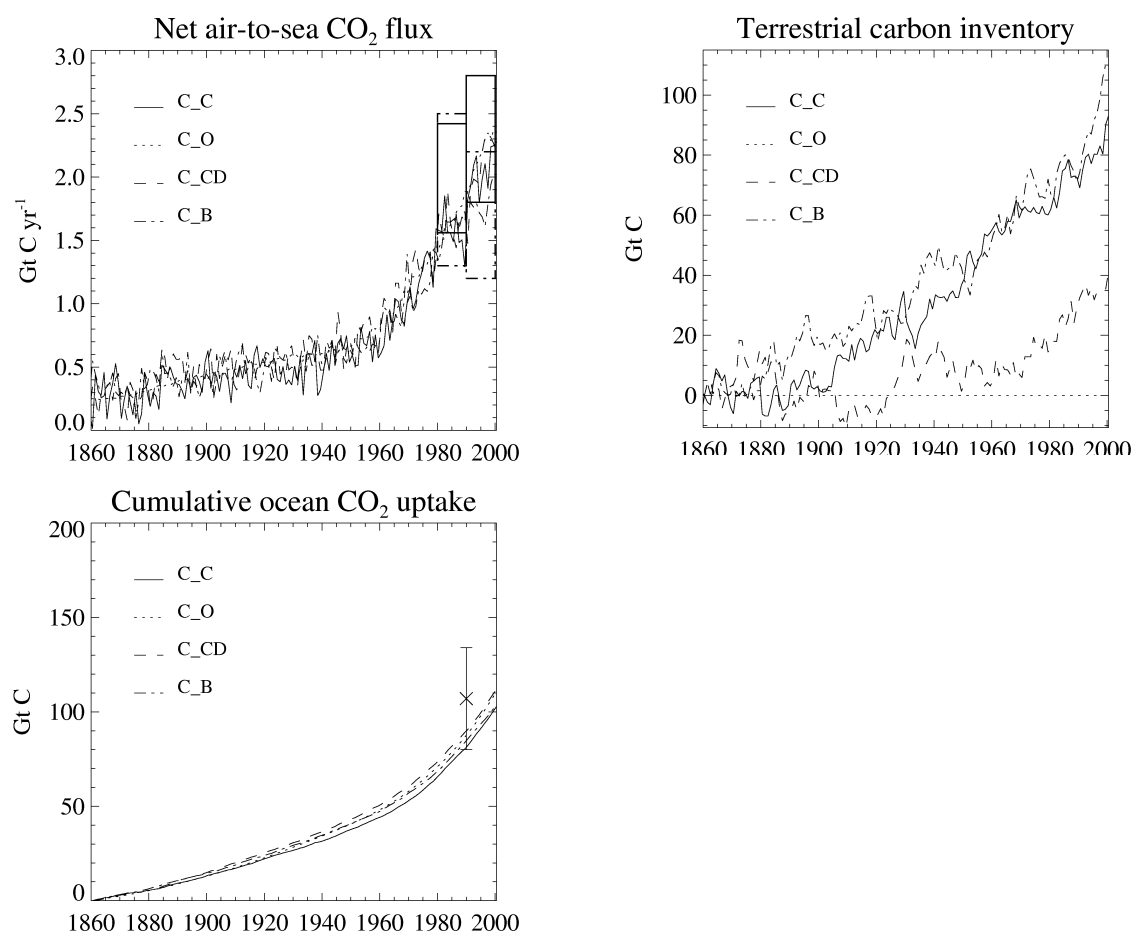


Figure 23: Results from the experiments in which the evolution of the atmospheric CO_2 concentration was prescribed (acronyms refer to Table 1): globally averaged, annual mean net air–sea flux (top, left) and oceanic and terrestrial carbon inventories (bottom, left and top, right, respectively). Inventories are relative to year 1860 AD so that they may be compared with available estimates. In the upper left panel, the boxes represent the mean values over a decade as from OCMIP2 (solid boxes) and from IPCC (dash-dot boxes). In the lower panel, the estimated oceanic DIC inventory in 1990 from Houghton et al. (2001) together with its standard deviation are given by the cross and the vertical bar, respectively.

Larger differences between experiments are noticed when the atmospheric CO_2 concentration is interactive in the model (Figure 24). This is mainly due to the fact that the CO_2 level is not the same in all experiments. Among the three runs which were performed with the same scenario of fossil fuel emission (E_C, E_R and E_CD), the one with no climate change results in the largest atmospheric CO_2 abundance in year 2000 AD (see Table 2). This is caused by a reduced uptake of carbon by the continental vegetation. The moderate climate change over the 20th century (see Section 3.2) seems to significantly affect the terrestrial carbon uptake (see Figure 24), which in this case constitutes a negative feedback on the

atmospheric CO₂ concentration. It should be noted that the CO₂ fertilization effect on terrestrial plants is included in all of the experiments presented in Figure 24. The atmospheric CO₂ differences from one experiment to the other not only result from differences in the forcing (emission scenario) but also from significant differences in oceanic and terrestrial cumulative uptake.

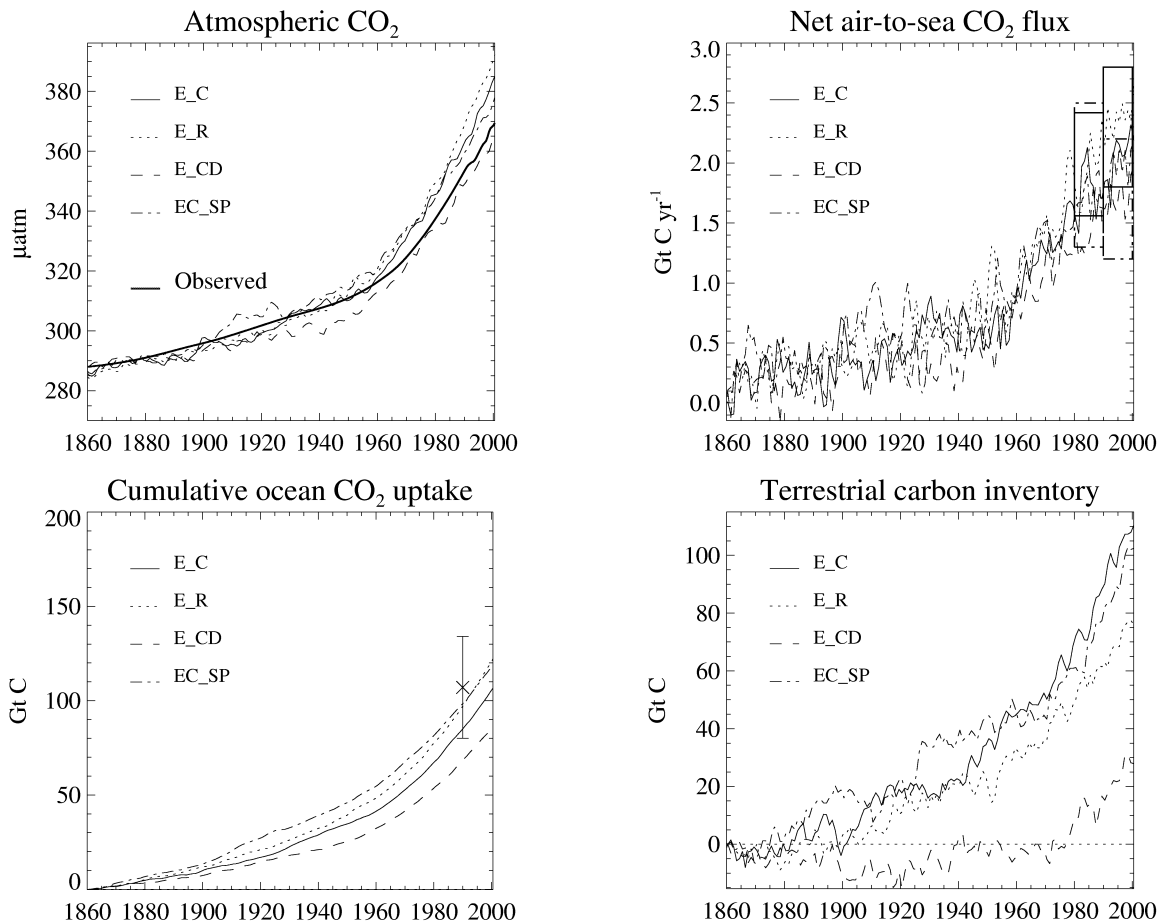


Figure 24: Results from the experiments with prognostic atmospheric CO₂ (acronyms refer to Table 1): predicted atmospheric CO₂ concentrations (top, left) and globally averaged, annual mean net air–sea flux (top, right) and oceanic and terrestrial carbon inventories (bottom, left and right, respectively). Inventories are relative to year 1860 AD so that they may be compared with available estimates. The observed atmospheric CO₂ concentration in the upper left panel was obtained from the spline fit provided by the NOCES project (NOCES HowTo, 2003). In that panel, the boxes represent the mean values over a decade as from OCMIP2 (solid boxes) and from IPCC (dash-dot boxes). In the lower left panel, the estimated oceanic DIC inventory in 1990 from IPCC (2002) together with its standard deviation are given by the cross and the vertical bar, respectively.

The lower values simulated in EC_SP and E_CD also results from lower anthropogenic emissions (see Figure 10). In the latter experiment, the computed

carbon fluxes from land-use change are much smaller than those given by Houghton and Hackler (2002). This point is illustrated in Figure 25. The net CO₂ flux resulting from the land-cover scenario of Ramankutty and Foley (1999) is estimated by calculating the difference in terrestrial carbon inventory between experiments differing only in the LCC scenario. It is clear from Figure 25 that the LU emissions under the LCC scenario are much lower in the second half of the 20th century than those from Houghton and Hackler (2002). The LCC scenario only prescribes the area covered with grass and cultures. The carbon fluxes from this activity represent the fraction of tree that grew on areas where they are to be eliminated. At this stage, it is hard to tell whether the model underestimates the tree biomass in those areas or the LCC scenario overestimates the surface in which forests regressed.

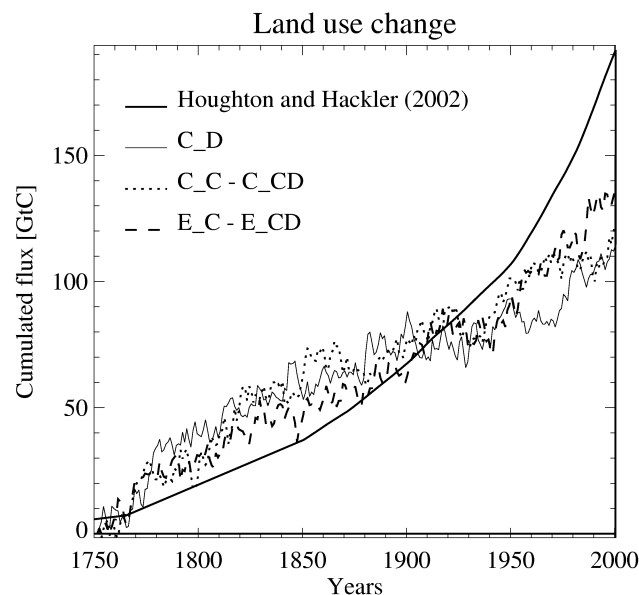


Figure 25: Cumulated CO₂ emissions from land-cover change over the industrial era. The solid line represents the values from Houghton and Hackler (2002). The three other curves give the fluxes from the experiments in which the land-use scenario from Ramankutty and Foley (1999) was used.

3.4. Conclusions

Although a number of shortcomings have been identified, the results discussed in the previous section demonstrate that the model shows acceptably good agreement with enough aspects of the behaviour of the real climate system over the last few centuries to permit a useful study of the future evolution of climate, sea level and carbon cycle in response to human activities.

4. PROJECTIONS OF CLIMATE, SEA-LEVEL AND CARBON-CYCLE CHANGES OVER THE 21ST CENTURY

In this section, we present some results from a number of projections carried out with LOVECLIM over the 21st century.

4.1. Forcing scenarios

In these experiments, the model was driven by changes in greenhouse-gas, tropospheric ozone and sulphate-aerosol concentrations following the IPCC SRES scenarios B1, A1B and A2 (Houghton et al., 2001; Figure 26). The solar constant was kept fixed to its 2000 AD value and no volcanic eruption was assumed to occur. Furthermore, in the simulations analysed in Sections 4.3.1 and 4.3.2, the deforestation forcing was not accounted for. Some projections were also performed in which the model was forced by scenarios of anthropogenic CO₂ emissions (fossil fuel and land-use; Figure 27). Results from those runs with prognostic atmospheric CO₂ are presented in Section 4.3.3.

4.2. Experimental design

For all scenarios, the experiments spanned the time interval 2000–2100 AD. Initial conditions for the runs discussed in Sections 4.3.1 and 4.3.2 consisted of outputs for year 2000 AD of a simulation conducted over the last 500 years. This experiment was similar to the one presented in Section 3, except that the deforestation forcing was not taken into consideration. Only one simulation was carried out for each scenario.

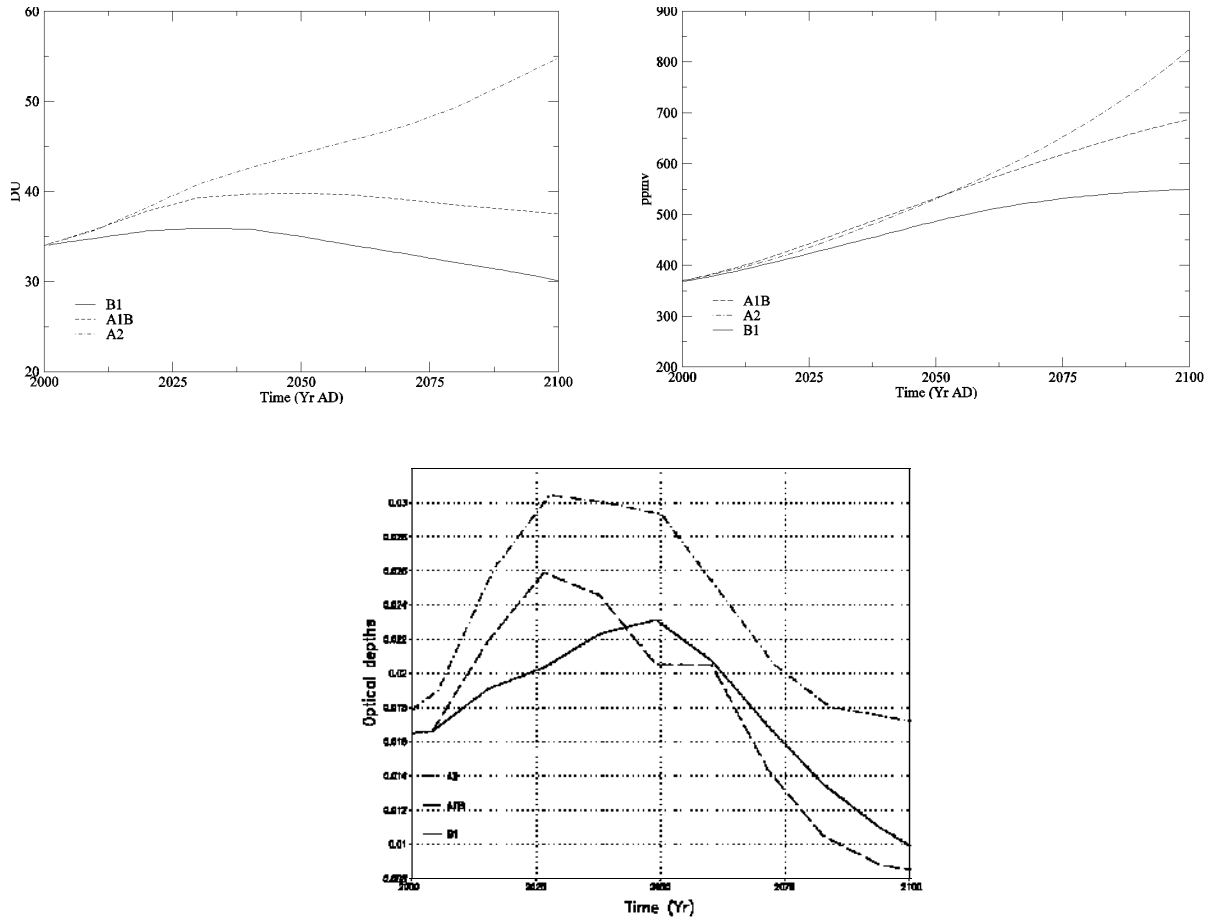


Figure 26: Evolution over the 21st century of the abundances of tropospheric ozone (top, left), carbon dioxide (top, right) and sulphate aerosols (bottom) according to the IPCC SRES scenarios B1, A1B and A2.

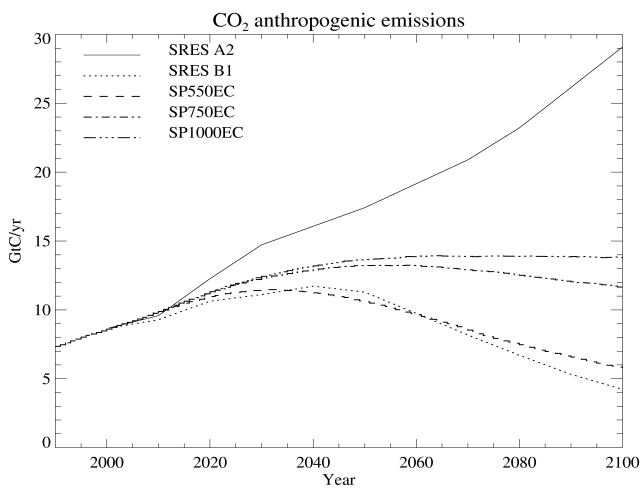


Figure 27: Selected anthropogenic CO₂-emission scenarios for the 21st century.

4.3. Results

4.3.1. Climate

Surface temperature. Table 3 gives the globally averaged, annual mean surface warmings simulated by the model at the end of the 21st century for the three forcing scenarios together with the IPCC estimates (Houghton et al., 2001). The model response appears too weak at the global scale. The cause of this problem, which was also encountered in the simulations covering the last few centuries, has already been discussed (see Section 3.3.1). The geographical distribution of the warming will be examined in Section 5.

Scenario	LOVECLIM	Simple climate models
SRES B1	1°C	1.4–2.6°C
SRES A1B	1.4°C	2.1–3.8°C
SRES A2	1.8°C	2.7–4.7°C

Table 3: Increases in globally averaged, annual mean surface temperature between 1990 and 2100 AD for the three forcing scenarios considered. The column "LOVECLIM" lists the temperature differences between the period 1980–2000 AD and the period 2090–2110 AD; the column "Simple climate models" gives the corresponding values from simple climate models tuned to CGCM results (Houghton et al., 2001). The upper boundary of the ranges corresponds to a sensitivity of 3.7°C and the lower one to a sensitivity of 2.1°C.

Precipitation. On an annual average, the global mean precipitation simulated by LOVECLIM at the end of the 21st century is enhanced by 6.6% in SRES A2, 5.1% in SRES A1B and 3.6% in SRES B1. These changes fall within the range of CGCM results (Houghton et al., 2001). For instance, under the SRES A2 forcing scenario, CGCMs produce an increase in precipitation ranging between 1.3 and 6.8%, with a mean value of 3.9%. Consistently with CGCM results, precipitation increases over the Sahara area and at mid- and high latitudes in both hemispheres. However, the magnitude of the increase seems slightly underestimated at the northern high latitudes. Furthermore, LOVECLIM fails in reproducing the strong decrease in precipitation simulated by CGCMs in tropical regions (Houghton et al., 2001). Decreases in precipitation are however observed over the entire North America as well as over south-eastern Europe.

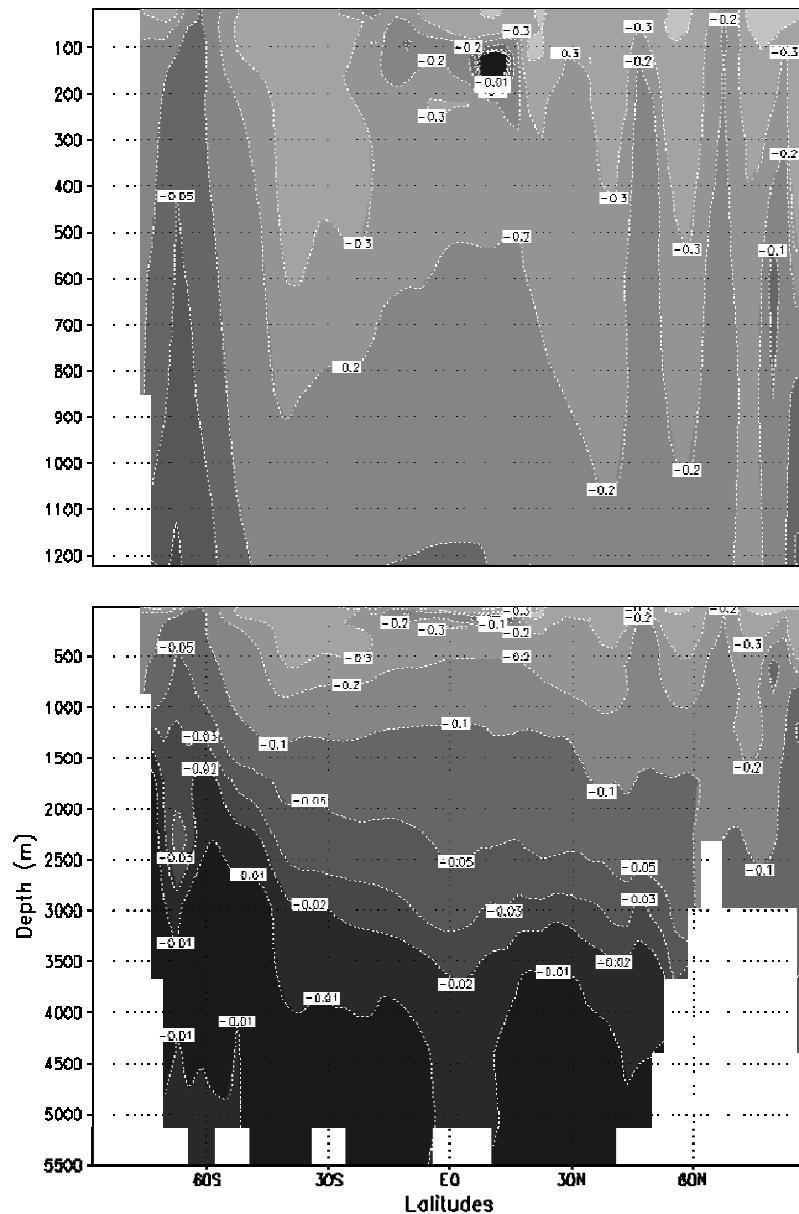


Figure 28: Latitude–depth distribution of the change in zonally averaged, annual mean potential density (in kg m^{-3}) in the Atlantic basin at the end of the simulation SRES A2. The plotted changes are relative to the values obtained in CTL.

MOC. A weakening of the MOC is noticed in all runs. At the end of the 21st century, the decrease in the maximum value of the annual mean meridional overturning streamfunction below the surface layer between 45° and 75° N in the Atlantic basin reaches 27% in SRES A2, 21% in SRES A1B and 19% in SRES B1 (those changes are relative to the value obtained in CTL). To understand the causes of this behaviour, we analyse here the changes in potential density simulated by the model in the Atlantic Ocean. Any of those changes can be split into a temperature contribution and a salinity contribution:

$$\Delta\sigma = \sigma_{EXP} - \sigma_{CTL} \approx \Delta_T\sigma + \Delta_S\sigma,$$

where σ represents the potential density. The subscript EXP denotes any of the three SRES experiments. $\Delta_T\sigma$ and $\Delta_S\sigma$ are the temperature contribution and salinity contribution to the density change, respectively. This method is valid as long as the mixed terms in the equation of state for potential density involving products of salinity and temperature are small. Figure 28 shows that the potential density in the high latitudes of the North Atlantic Ocean and in the Arctic Ocean decreases in a wide depth range, thus reducing the horizontal depth-integrated density gradient (steric height) between 30° S and 80° N, which drives the NADW cell. Figure 29 indicates that the salinity effect is mainly responsible for the decrease north of 70°N. Around 60°N, i.e. the area of NADW formation, the temperature contribution dominates. Since temperature and salinity changes result from modifications in the oceanic circulation that are themselves associated with changes in both the surface heat and freshwater fluxes, it is not possible to directly determine if they are induced by surface heat or freshwater fluxes. To answer this question, Gregory et al. (2005) performed with a variety of models a series of four simulations aiming at assessing the relative impact of the surface heat and freshwater fluxes on the MOC weakening in a 4×CO₂ experiment. Two baseline integrations with either fixed or increasing atmospheric CO₂ concentration were first carried out. In two additional runs (partially coupled experiments), the surface freshwater flux was no longer simulated but prescribed according to one of the fully coupled experiments. The conclusion of this study was that, in the eleven models involved, the MOC weakening was caused more by changes in surface heat flux than by changes in surface freshwater flux. As ECBilt–CLIO–VECODE participated to this model intercomparison, one can anticipate that the decrease of the MOC intensity in our simulations is mostly due to the increase of the heat flux towards the ocean. This was confirmed by a sensitivity experiment in which the ice-sheet component of the model was not activated.

Sea ice. Table 4 compares the trends in Arctic annual mean ice area for all forcing scenarios to the corresponding ones simulated by the CGCMs that were used for the IPCC Fourth Assessment Report (AR4). It can be seen that the trends produced by LOVECLIM are smaller than CGCMs ones. This discrepancy is partly caused by an overestimation of the ice thickness in the Eurasian sector of the Arctic basin under modern forcing conditions, which is associated with an erroneous wind pattern in this region.

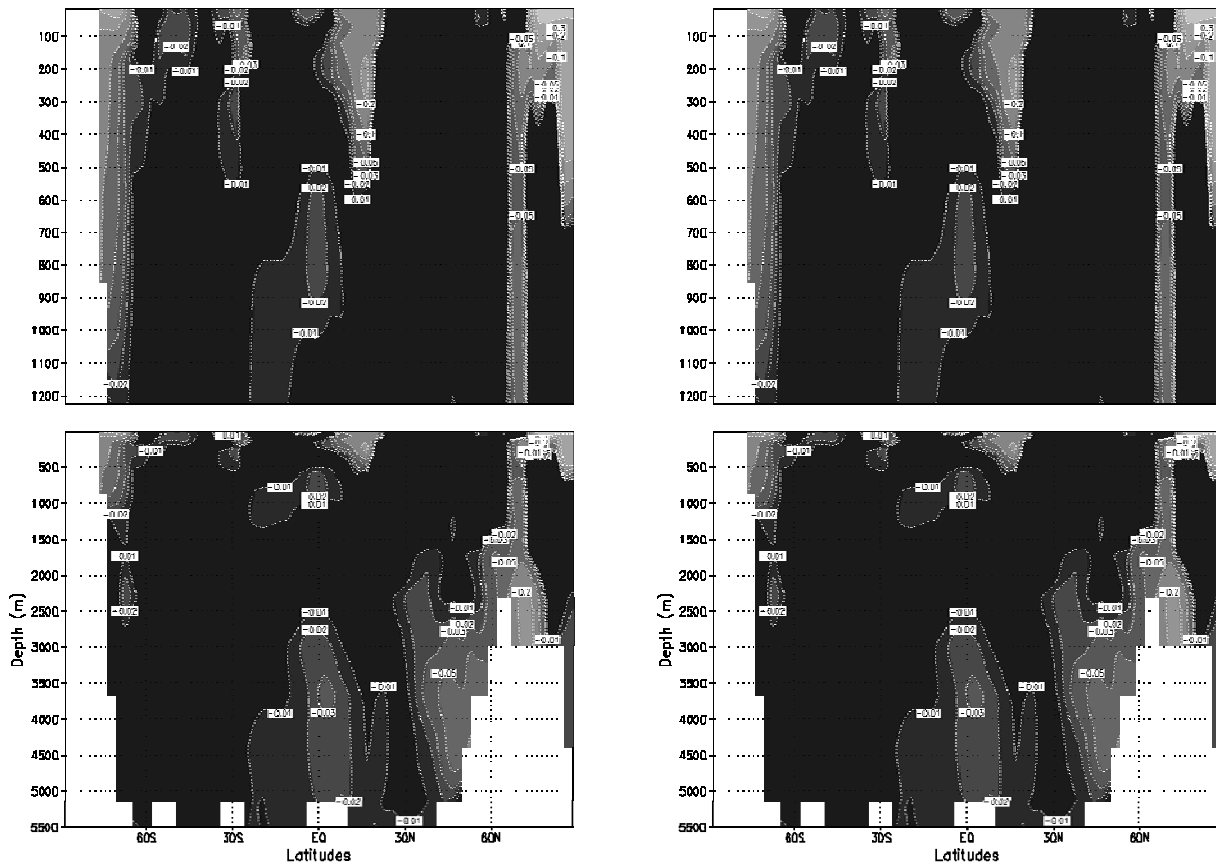


Figure 29: Latitude–depth distribution of the salinity (left) and temperature (right) contributions to the change in zonally averaged, annual mean potential density (in kg m^{-3}) in the Atlantic basin at the end of the simulation SRES A2. The plotted changes are relative to the values obtained in CTL.

Scenario	LOVECLIM	IPCC AR4 CGCMs
SRES B1	-1.0×10^5	$-2.4 \pm 1.2 \times 10^5$
SRES A1B	-1.9×10^5	$-3.8 \pm 1.8 \times 10^5$
SRES A2	-2.3×10^5	$-4.1 \pm 1.3 \times 10^5$

Table 4: Average trends in Arctic annual mean ice area (in km^2 per decade) over the 21st century as simulated by LOVECLIM and the IPCC AR4 CGCMs.

4.3.2. Ice sheets, glaciers and sea level

In this section, we mainly focus on the response of the continental cryosphere and global sea level for the mid-scenario A1B.

Whereas we found little response for the Greenland ice sheet during the 20th century, changes are definitely more profound for the 21st century. Mean annual

warming over Greenland rises to about 3°C by 2100 AD (Figure 30). This 3°C is often cited as the threshold for a balanced surface mass budget, beyond which the Greenland ice sheet can no longer be sustained and will eventually fully disintegrate (Gregory et al., 2004a; Gregory and Huybrechts, 2006). This threshold is confirmed by LOVECLIM as shown in the lower panel of Figure 30. By the end of the 21st century, the amount of surface runoff roughly doubles to become of equal magnitude than the total accumulation, indicative of a balanced surface budget. The iceberg-calving flux, on the other hand, decreases by 40% as less ice borders the ocean, making the total mass budget negative so that the ice sheet starts to shrink. Under these circumstances, the Greenland ice sheet loses 0.7% of its ice volume and 1% of its area after 100 years, equivalent to a sea-level rise of a little more than 5 cm.

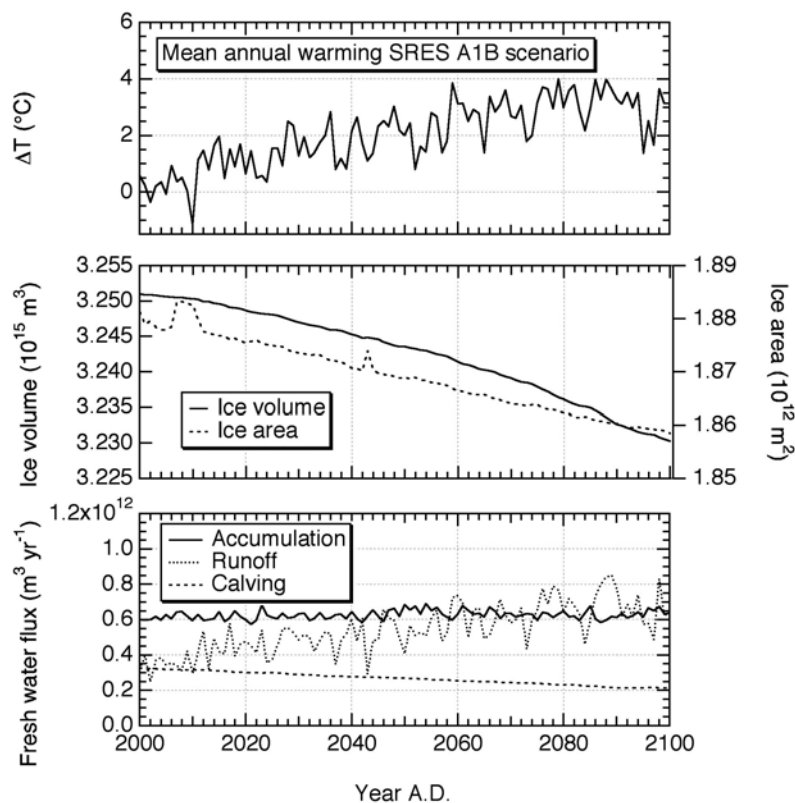


Figure 30: Predicted evolution of the Greenland mean annual temperature, ice volume and area, and mass-balance components for the 21st century under SRES scenario A1B.

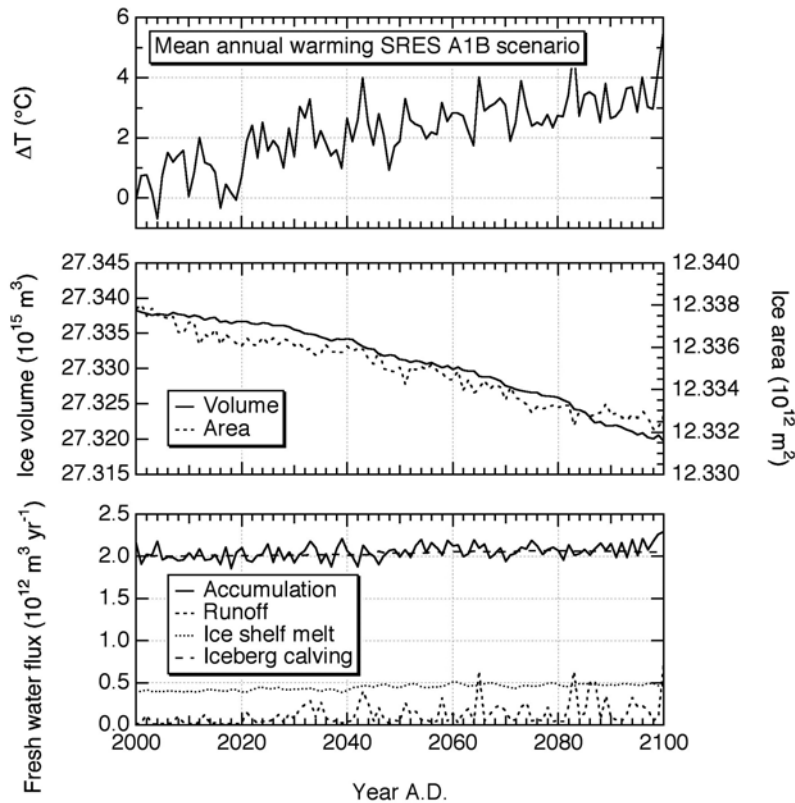


Figure 31: Predicted evolution of the Antarctic mean annual temperature, ice volume and area, and mass-balance components for the 21st century under SRES scenario A1B.

Over Antarctica, we find comparatively little changes during the 21st century. Despite a modelled warming trend over the ice sheet of about 4°C during the next hundred years, driving mass-balance terms such as total accumulation and ice-shelf melt show only a small response (Figure 31). The combination of rising temperatures and almost constant accumulation is striking in the light of the generally positive correlation between temperature and precipitation of $5.1 \pm 1.5\% \text{ } ^\circ\text{C}^{-1}$ as found in IPCC AR4 CGCMs (Gregory and Huybrechts, 2006). The amount of basal melting below the ice shelves similarly has only a very small rising trend, but this can be explained by the thermal inertia of the Southern Ocean and the time it takes for the ocean to equilibrate with the higher atmospheric temperatures. At the same time, coastal warming initiates some meltwater runoff at the ice-sheet margin, which reaches up to 15% of the accumulation during peak warm years. Consequently, also during the 21st century, the response of the Antarctic ice sheet is dominated by the continuing long-term background trend, which explains more than 70% of the total ice-volume loss. In contrast to most other studies (Wild et al., 2003; Huybrechts et al., 2004), this volume loss is not counteracted by the effect of increased snowfall. On the contrary, increased runoff during the 21st century already accounts for about 1 cm of sea-level rise. The LOVECLIM results therefore do not support most other future simulations

which predict net Antarctic ice-sheet growth because of higher accumulation rates in combination with still negligible surface runoff.

By year 2100 AD, mountain glaciers are found to have lost about 45% of their area and 38% of their year 2000 volume for the SRES scenario A1B (Figure 32). The melting of small ice caps, on the other hand, is found to proceed at a lower rate owing to their more poleward position and generally lower climate sensitivities typical for their drier climate regimes.

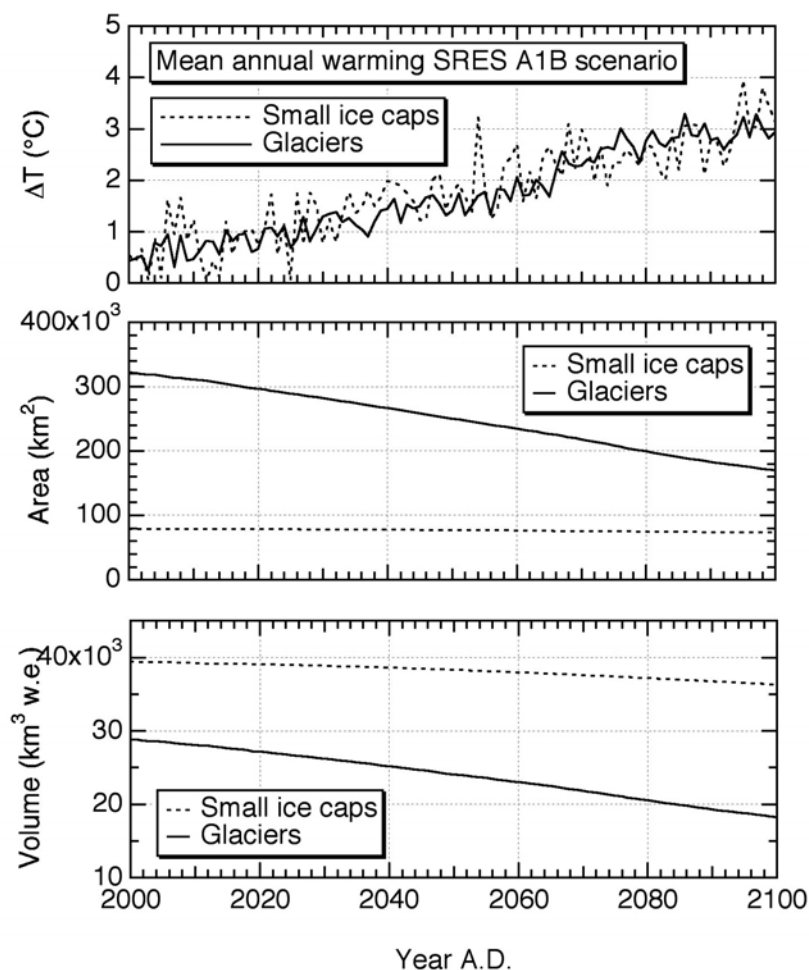


Figure 32: Predicted evolution of mountain glaciers and small ice caps for the 21st century under SRES scenario A1B.

Figure 33 summarizes total sea-level change and its components for the SRES scenario A1B. During the 21st century, all components are found to contribute positively for a total sea-level rise of 31.3 cm. As for the 20th century, the most important contributor is the oceanic thermal expansion (+18.8 cm), followed by the contributions from the Greenland ice sheet (+5.2 cm), glaciers and ice caps (+3.8 cm) and the Antarctic ice sheet (+3.5 cm). The total rise is equivalent to a quadrupling of the sea-level rise of 7.5 cm simulated for the 20th century. Our sea-

level value is somewhat lower than the central estimate for the same four components of about 40 cm in the IPCC TAR predictions (Church et al., 2001). This can be explained by the low climate sensitivity of LOVECLIM, and hence the lower global temperature rise, which mostly affects the largest contribution of thermal expansion of the World Ocean. Another major difference with the IPCC TAR predictions is the positive contribution from Antarctica of several cm of sea-level rise. That is in contrast to most other simulations showing a growing ice sheet and a negative contribution to global sea level of typically between -5 and -20 cm. The IPCC TAR also found a generally larger contribution from mountain glaciers and small ice caps. Our glacier-volume loss is smaller because of the lower initial glacier volume assumed by the glacier-melt algorithm.

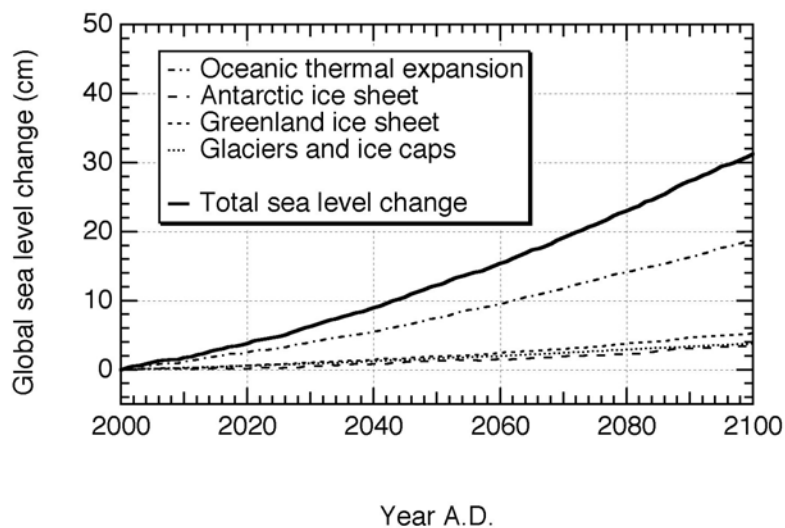


Figure 33: Predicted sea-level change and its components for the 21st century under SRES scenario A1B.

The total predicted sea-level rise for the 21st century is only slightly affected by the scenario itself (Figure 34), in good agreement with the results reported by Church et al. (2001). For the range of SRES scenarios used by LOVECLIM, total sea-level rise is found to vary between +22 and +35 cm by year 2100 AD. The much larger range of between +9 and +88 cm obtained for the IPCC TAR arose mainly from the inclusion of model uncertainties, and not from the greenhouse-gas-forcing scenarios employed.

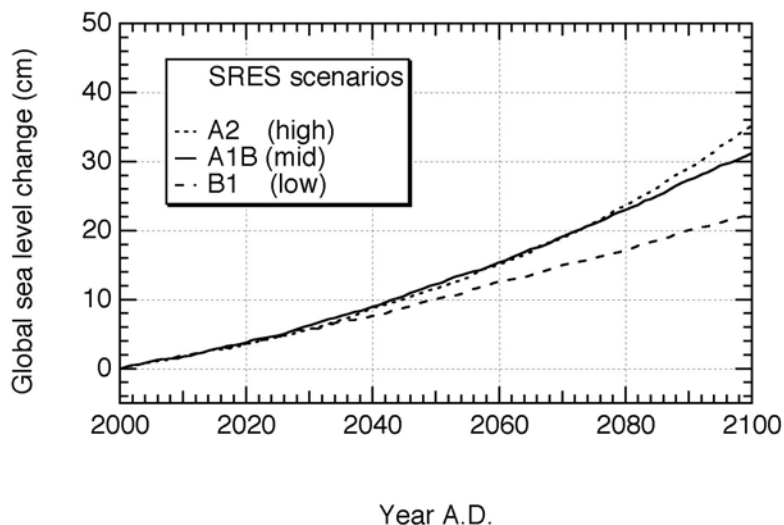


Figure 34: Predicted total sea-level rise for SRES scenarios B1, A1B and A2 during the 21st century.

4.3.3. Carbon cycle

Many experiments were conducted with LOVECLIM over the 21st century under various atmospheric CO₂ concentration or anthropogenic emission scenarios. Most of these simulations will be analyzed in Section 5, while we restrict our discussion in the present section to experiments which may be compared to other modelling studies.

Experiments with prescribed evolution of the atmospheric CO₂ concentration

Figure 35 illustrates the results obtained under SRES scenario A2 over the 21st century. The different experiments shown are those described in Section 3.3.3 (see Table 1). From year 2000 AD, they were continued by applying the SRES A2 scenario for the atmospheric CO₂ concentration. For the land-cover-change scenario (experiment C_CD), the crop fraction was kept fixed to that in 1992 AD, which corresponds to the last year of the dataset of Ramankutty and Foley (1999). Each of these simulations was accompanied by a control run so that our results reflect coherent changes in the carbon cycle. As expected, climate change impacts the air–sea CO₂ exchange by lowering the solubility and hence the net oceanic uptake. The difference between the cumulative oceanic uptake between the situation with climate change and that without is however modest (472 GtC against 514, or less than 10%). The reason for such a small change is mainly to be found in the moderate increase in globally averaged, annual mean sea-surface temperature predicted by our model (~1.2°C in 2100 AD, see Figure 35).

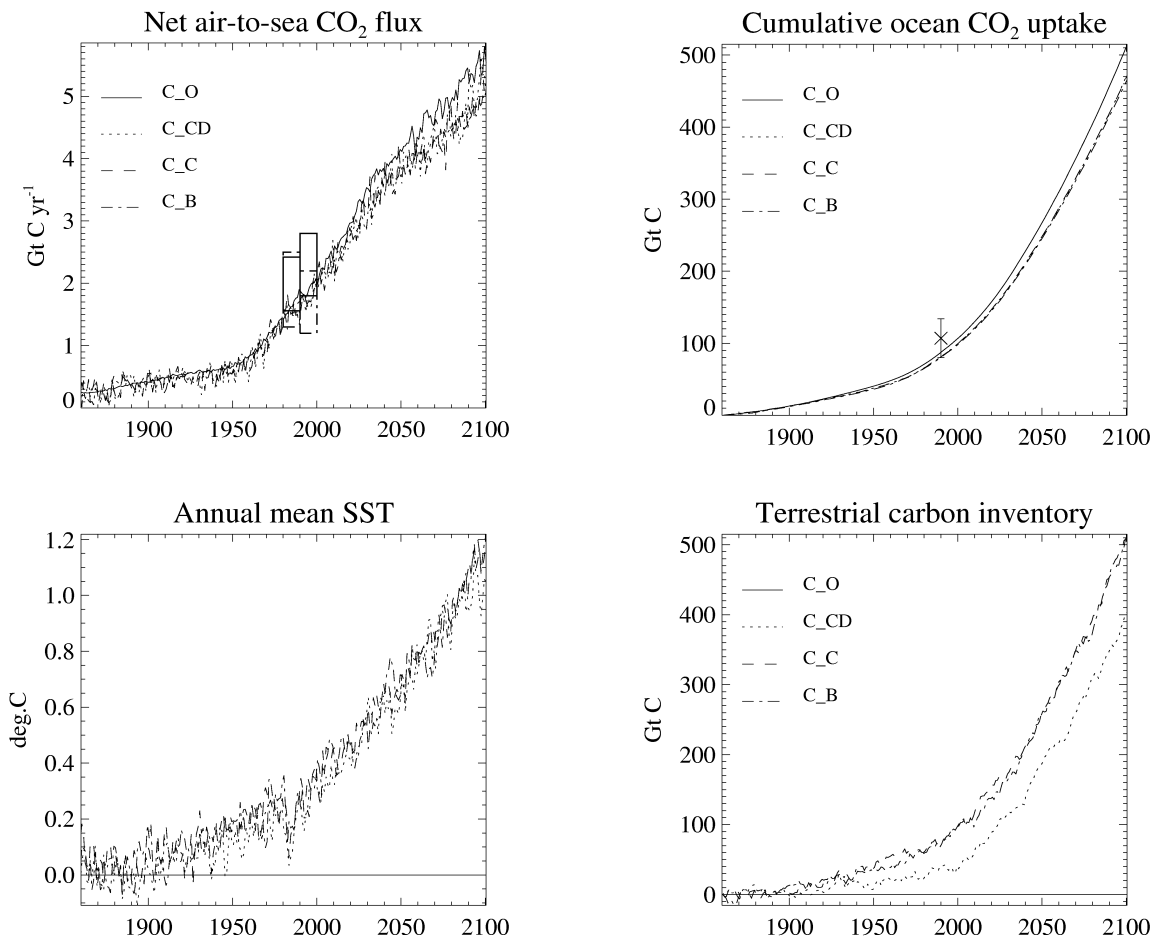


Figure 35: Results from the experiments in which the evolution of the atmospheric CO₂ concentration followed the SRES scenario A2 (acronyms refer to Table 1): globally averaged, annual mean net air–sea flux (top, left), oceanic and terrestrial carbon inventories (top, right and bottom right, right, respectively), and sea-surface temperature (bottom left). Inventories are relative to year 1860 AD. In the upper left panel, the boxes represent the mean values over a decade as from OCMIP2 (solid boxes) and from IPCC (dash-dot boxes). In the upper right panel, the estimated oceanic DIC inventory in 1990 from Houghton et al. (2001) together with its standard deviation are given by the cross and the vertical bar, respectively.

Contrary to some predictions (e.g., Sarmiento et al., 1998), we do not observe any significant change in the oceanic biology at the global scale during the 21st century. None of the physical changes described earlier do seem to affect noticeably the global oceanic carbon cycle over that period in our model. The picture is a bit different regarding the terrestrial carbon cycle. Both the climate and fertilization effects strongly enhance the carbon uptake in VECODE. Moreover, the deforestation results in a slight cooling (see bottom right panel of Figure 35); this effect, however minimal, constitutes a negative feedback.

Experiments with prognostic atmospheric CO₂

We focus here on experiments in which anthropogenic CO₂ emissions followed the SRES scenario A2, as did the other radiative forcings. We consider three cases: full climate change with no land-cover change (experiment E_C), no climate change (experiment E_R) and an experiment with both climate and land-cover changes (experiment E_CD). In the third case, the land-use component of the anthropogenic forcing was no longer directly included in the emissions but was indirectly provided by the deforestation scenario. For the land-cover change, the crop fraction was kept fixed to that in 1992 AD as above. The initial conditions were provided by the results obtained in year 2000 AD (see Section 3.3.3). A control run was also performed so that the figures presented in this section represent anomalies. This ensures that any model drift does not bias the results.

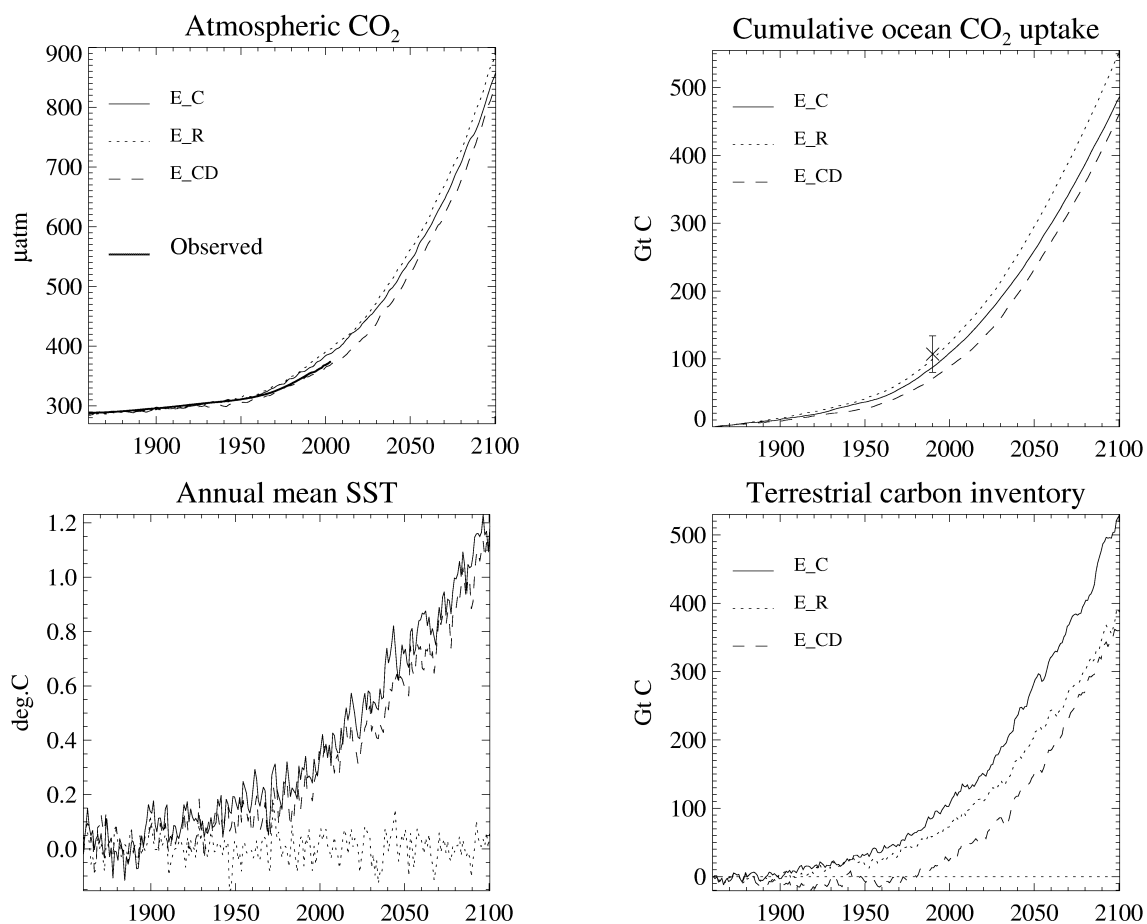


Figure 36: Results from the experiments in which the evolution of the anthropogenic CO₂ emissions followed the SRES scenario A2 (acronyms refer to Table 1): globally averaged, annual mean net air–sea flux (top, left), oceanic and terrestrial carbon inventories (top, right and bottom right, respectively), and sea-surface temperature (bottom left). Inventories are relative to year 1860 AD. In the upper right panel, the estimated oceanic DIC inventory in 1990 from Houghton et al. (2001) together with its standard deviation are given by the cross and the vertical bar, respectively.

Figure 36 depicts the evolutions over the 20th and 21st centuries of the atmospheric CO₂ concentration and of the globally averaged, annual mean oceanic and terrestrial carbon inventories and sea-surface temperature. The lower level of atmospheric CO₂ in 2100 AD obtained in E_CD is due to smaller cumulated land-use emissions. This lower CO₂ level together with the cooling accompanying deforestation is responsible for a slightly lower sea-surface temperature. However, the climatic effect on the terrestrial carbon is strong enough to cancel any difference between terrestrial carbon stocks by the year 2100 AD between experiments E_R and E_CD.

	Carbon inventories in 2100 AD (GtC)				pCO ₂ (µatm)	
	Ocean		Continents		in 2100 AD	
	E_R	E_C	E_R	E_C	E_R	E_C
LOVECLIM	545	478	386	531	891	858
Dufresne et al. (2002)	670	700	680	480	695	770
Cox et al. (2000)	370	490	630	-100	700	980

Table 5: Carbon inventories and atmospheric CO₂ partial pressure in 2100 AD obtained under the emission SRES scenario A2 in LOVECLIM and in two other modelling studies. Carbon inventories are relative to the year 1860. The results are reported for the two experiments E_C and E_R (with and without climate change, respectively).

Interestingly enough, the atmospheric CO₂ concentration is lower in the climate-change experiment than in the experiment with no radiative forcing. This is in contrast with two other modelling studies (Cox et al., 2000; Dufresne et al., 2002) which concluded in larger atmospheric CO₂ levels at the end of the 21st century under climate change. We applied exactly the same procedure as that followed by Dufresne et al. (2002). On the other hand, our results may only be qualitatively compared to the study of Cox et al. (2000) as their experimental setup differed in several aspects, the main difference lying in their use of the IS92a emission scenario instead of the A2 one. Table 5 lists the carbon inventories and the atmospheric CO₂ pressures in 2100 AD obtained with LOVECLIM and the two other models. The atmospheric pCO₂ predicted by LOVECLIM differs by less than 5% between the experiments with and without climate change. This contrasts with the large changes

simulated by the two other models (11% and 40%). Also, the CO₂ level in 2100 AD computed by LOVECLIM is larger than the one obtained by Dufresne et al. (2002) under the same scenario.

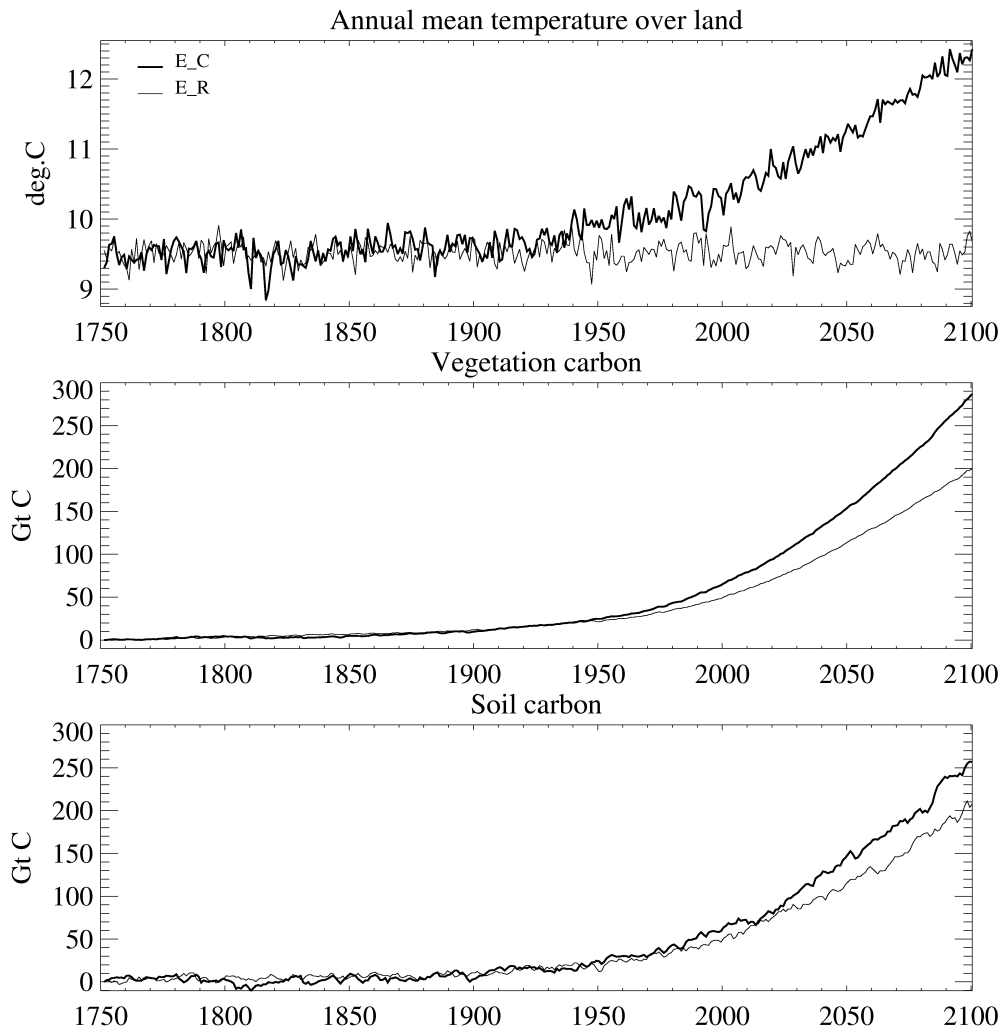


Figure 37: Evolution over 1750–2100 AD of the carbon stocks in vegetation (middle) and in soil (bottom) for experiments E_C and E_R. The upper panel shows the evolution of the globally averaged, annual mean surface temperature over land for the same period.

It was already mentioned in Section 3.3.3 that the oceanic carbon uptake over the industrial era is in the lower range of available estimates. This factor together with the lower uptake by the continental biosphere in LOVECLIM when compared to the other studies explains the higher CO₂ level. On the other hand, LOVECLIM predicts an increase of the carbon uptake by the continental biosphere under climate change. In experiment E_C, the oceanic uptake decreases as a consequence of both the larger sea-surface temperature (+1.2°C) and the lower pCO₂, but the continental carbon inventory is larger in E_C than in E_R. As the CO₂ fertilization effect is taken

into account in both experiments, this is a direct consequence of the enhanced precipitation and of the temperature increase. The climatic effect is responsible for approximately 38% of the increase in the continental carbon uptake. The models quoted in Table 5 simulate a much larger temperature increase over the continents than does our model. The Cox et al.'s (2000) study predicts a global increase of about 8°C over continents, while the change in our experiments amounts to only 2.5°C (Figure 37). The large temperature increase in the Cox et al.'s (2000) study leads to a drier climate at low latitudes which has dramatic consequences on equatorial forests; this explains the opposite response from their model. Figure 37 also illustrates the distribution among reservoirs on the continents. Most of the carbon is incorporated into the living vegetation (leaves and stems) and, as a consequence, the soil-reservoir increase lags behind. From that figure, we may deduce that up to 70% of the response of the vegetation-carbon stock comes from the fertilization effect, while the climate is responsible for the remaining part. However, one must keep in mind that most of the uncertainty about the global carbon cycle comes from the continental vegetation response to climate and CO₂ changes (Houghton et al., 2001). Processes in soil are still very badly known and there is a lot of discussion going on about the role of moisture and temperature in their degradation rate.

5. PROJECTIONS OF CLIMATE, SEA-LEVEL AND CARBON-CYCLE CHANGES OVER THE NEXT MILLENNIA

The aim of this section is to discuss results from simulations of climate, sea-level and carbon-cycle changes conducted with LOVECLIM over the next millennia.

5.1. Forcing scenarios and experimental design

A series of 25 experiments were performed. These can be divided into four groups.

Experiments under idealized CO₂ forcings. These simulations started from outputs of the pre-industrial equilibrium control run CTL and lasted 3000 years. In three of them, the atmospheric CO₂ concentration was enhanced to two times its pre-industrial value. The difference between the three experiments lay in the rate of increase: 0.5% per year until CO₂ doubling in IS2×0.5, 1% per year until CO₂ doubling in IS2×1.0 and 2% per year until CO₂ doubling in IS2×2.0. Once the 2×CO₂ level was reached, the concentration was kept constant until the end of the simulations (Figure 38). The same experimental design was repeated for a 4×CO₂ (see Figure 38). Three last experiments were carried out in which the CO₂ concentration was enhanced to 4×CO₂ and then decreased to its pre-industrial level with the same rate of reduction in the three experiments (see Figure 38). Those simulations are idealized because they neglect other forcings than CO₂ and the transition between the increasing and decreasing phases is very abrupt. Their objective was to assess the model response to simple forcing scenarios and to compare it to the one obtained by other models.

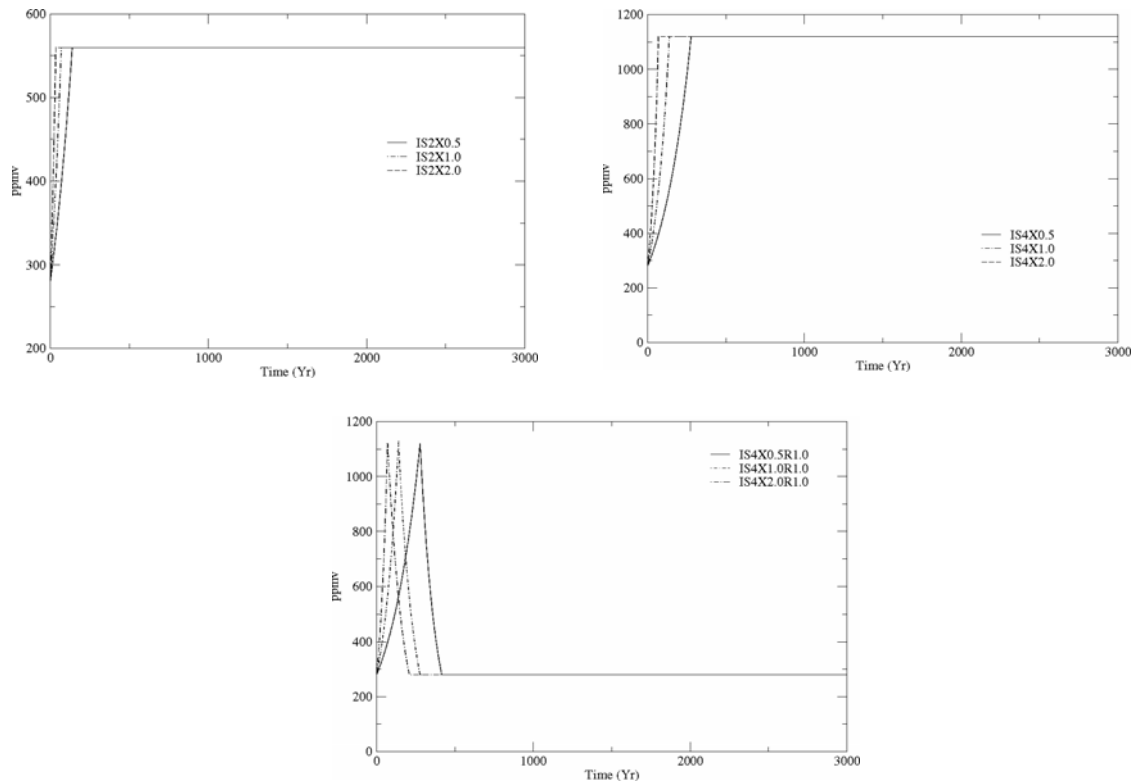


Figure 38: Evolution of the atmospheric CO₂ concentration in the first group of experiments.

Experiments under more realistic CO₂-stabilization profiles. These experiments began from results of CTL, which were assumed to represent the climate state in 1765 AD, and ended 1235 years later. As in the previous group of runs, only the CO₂ concentration was varied. A description of the stabilization-pathway construction can be obtained at the following address: <http://www.climate.unibe.ch/emicAR4/stab.txt>. The evolution of the atmospheric CO₂ concentration from 1765 AD to 2000 AD was derived from ice-core and atmospheric measurements. Thereafter, the model was driven by a range of CO₂-stabilization profiles (SP) intended for the IPCC AR4. The selected set of scenarios included stabilization of atmospheric CO₂ at levels of 350, 450, 550, 650, 750 and 1000 ppmv (Figure 39). For two of them (450 and 550 ppmv), a delayed turning point (DSP) was considered (see Figure 39). For the stabilizations at 350 and 450 ppmv, an overshooting of approximately 100 ppmv was also considered (see Figure 39). Those CO₂ scenarios are more realistic than the idealized stabilizations, i.e. they do not present discontinuities and they can be obtained from real CO₂ emissions.

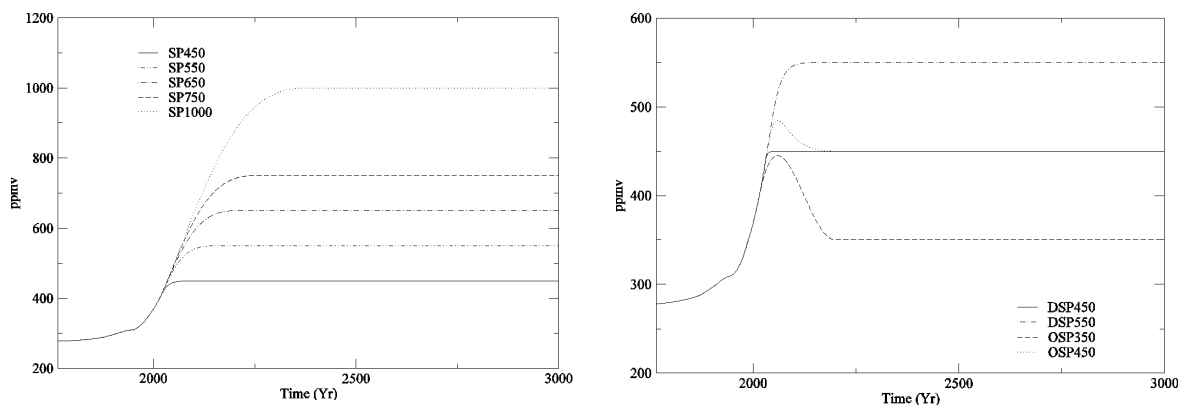


Figure 39: Evolution of the atmospheric CO₂ concentration in the second group of experiments.

Experiments under SRES scenarios for greenhouse-gas, tropospheric ozone and sulphate-aerosol forcings. Three projections were conducted with the greenhouse-gas, tropospheric ozone and sulphate-aerosol forcings following to the IPCC SRES scenarios B1, A1B and A2 during 100 years (see Figure 26) and held constant afterwards. The solar constant was kept fixed to its 2000 AD level and no volcanic eruption was supposed to occur. Initial conditions consisted of outputs for year 2000 AD of a simulation carried out over the last 500 years. This simulation was similar to the one presented in Section 3, except that the deforestation forcing was not accounted for. All experiments were 1000-yr long, except A2 which run for 2000 years.

Experiments with prognostic atmospheric CO₂. In these simulations, only the CO₂ forcing was taken into account. They started in 1765 AD from outputs of CTL and run until year 3000 AD. Contrary to the other experiments, the model was forced by anthropogenic CO₂ emissions. For the historical period, the CO₂ influxes followed the reconstructed fossil fuel and deforestation emissions (curve Bern-CC in Figure 10). Over the 21st century, the anthropogenic CO₂ emissions were derived from stabilization-profile scenarios which were used to drive the Bern carbon-cycle model (Houghton et al., 2001). Thereafter, they were set to zero (Figure 40).

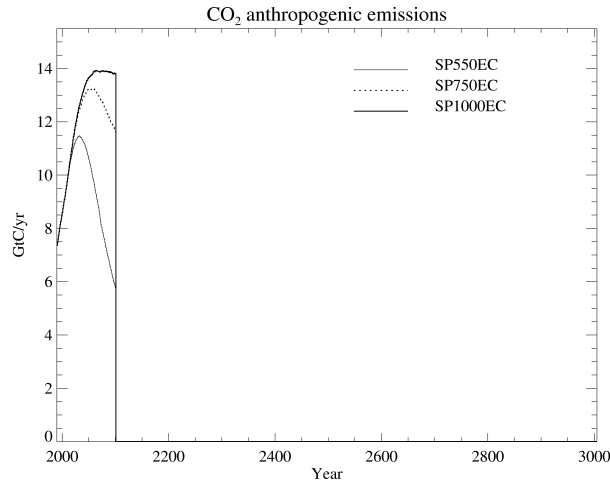


Figure 40: Anthropogenic carbon-emission scenarios used in the fourth group of experiments.

Figure 41 gives the radiative forcing value during the last years of each simulation in which this forcing was constant at the end of the model integration and different from the pre-industrial one.

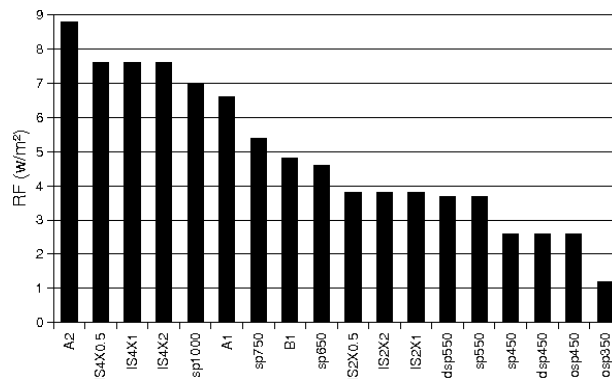


Figure 41: Radiative forcing at the end of each experiment. The simulations included in this figure are those in which the radiative forcing at the end of the model integration was constant and different from the pre-industrial one.

5.2. Results

5.2.1. Climate

Surface temperature

It is generally admitted that the relationship between the global surface temperature increase ΔT and a radiative perturbation ΔF at the tropopause may be written as (Houghton et al., 2001):

$$\Delta F = \lambda \Delta T + \Delta H,$$

where ΔH is the rate of heat storage in the system (i.e. a measure of the non-equilibrium of the system). The atmosphere reaching an equilibrium state within a few years, ΔH can be considered as the rate of heat uptake by the ocean (Raper et al., 2001). At equilibrium, it is obvious that $\Delta H = 0$. λ is the feedback parameter. It is related to the amplification by the model of a radiative perturbation: the higher λ , the weaker the amplification by feedbacks. This is actually a measure of the integrated effect of feedback processes taking place in the climate system (e.g., albedo–temperature feedback, cloud feedback, water-vapour feedback, ...).

Figure 42 displays the response of the globally averaged, annual mean surface temperature versus the radiative forcing minus the global oceanic heat uptake at the end of each simulation included in Figure 41. ΔH is the largest in sp1000, with a value of 0.3 W m^{-2} . This simulation exhibits the strongest disequilibrium because it is the one presenting the highest radiative forcing amongst the shortest simulations. The model is therefore not fully at equilibrium in all experiments. However, the globally averaged, annual mean surface temperature is close enough to equilibrium in all simulations to consider the values given in Figure 42 as equilibrium ones. We can therefore state that the equilibrium warming predicted by the model ranges from 0.55 to 3.75°C for the set of radiative forcings selected.

Figure 42 suggests that λ in LOVECLIM amounts to $2.28 \text{ W m}^{-2} \text{ }^\circ\text{C}^{-1}$. This value is higher than the ones found by Raper et al. (2001) in the second phase of the Coupled Model Intercomparison Project (CMIP2; $0.9\text{--}2.1 \text{ W m}^{-2} \text{ }^\circ\text{C}^{-1}$). It is also larger than the estimates obtained by Gregory et al. (2004b) with various versions of their CGCM ($0.91\text{--}2.0 \text{ W m}^{-2} \text{ }^\circ\text{C}^{-1}$). Thus, the sensitivity of our model is:

$$\frac{\Delta F}{\lambda} = \Delta T_{2X} = \frac{3.80 \text{ W m}^{-2}}{2.28 \text{ W m}^{-2} \text{ }^\circ\text{C}^{-1}} = 1.66^\circ\text{C},$$

which corresponds to the lower limit of the range of observationally-based estimates (Gregory et al., 2002).

Some experiments are several tenths of a degree away from the regression line shown in Figure 42. In the three $2\times\text{CO}_2$ runs, the model simulates a $\Delta T_{2\times}$ higher (1.76 °C) than the one predicted by the equation above. One could speculate that this is a manifestation of small non-linearities in the temperature response of the model to a radiative perturbation.

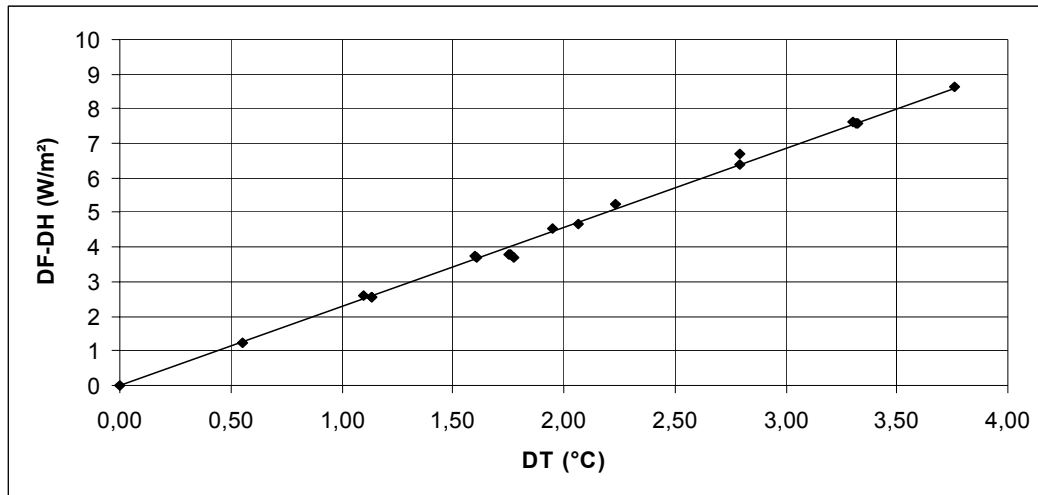


Figure 42: Regression of the global surface warming ΔT onto the global radiative forcing minus the oceanic heat uptake $\Delta F - \Delta H$. Each lozenge represents one particular simulation of Figure 41. ΔT is computed as the difference between the last 50 years of each transient simulation and the last 50 years of CTL. The equation of the regression line is $\Delta F - \Delta H = 2.28\Delta T$.

The fact that λ is almost the same in all simulations counteracts the hypothesis of any abrupt climate change at the global scale for the range of forcings used. Abrupt changes are non-linear processes that would manifest themselves by an abrupt variation of λ , i.e. a discontinuity in the relation between ΔF , ΔH and ΔT . The only possibility for this diagnostic to miss such a global abrupt event would be that the event appears before the end of the integration and that the system has come back to a state corresponding to a linear response. This is however not observed in the experiments we performed.

Figures 43 show the geographical distribution of the change in annual mean surface temperature at the end of IS4 \times 1.0 and osp350, which are two extreme experiments amongst the ones taking into account only variations in atmospheric CO_2 concentration. The warming pattern is roughly the same for both experiments. In particular, a strong polar amplification is observed in both hemispheres. North America experiences a significant warming, while the increase in temperature is rather modest over western Europe. South Australia and the Sahara region are dry

areas with little vegetation in CTL. They both undergo a relatively large warming compared to other regions at the same latitudes.

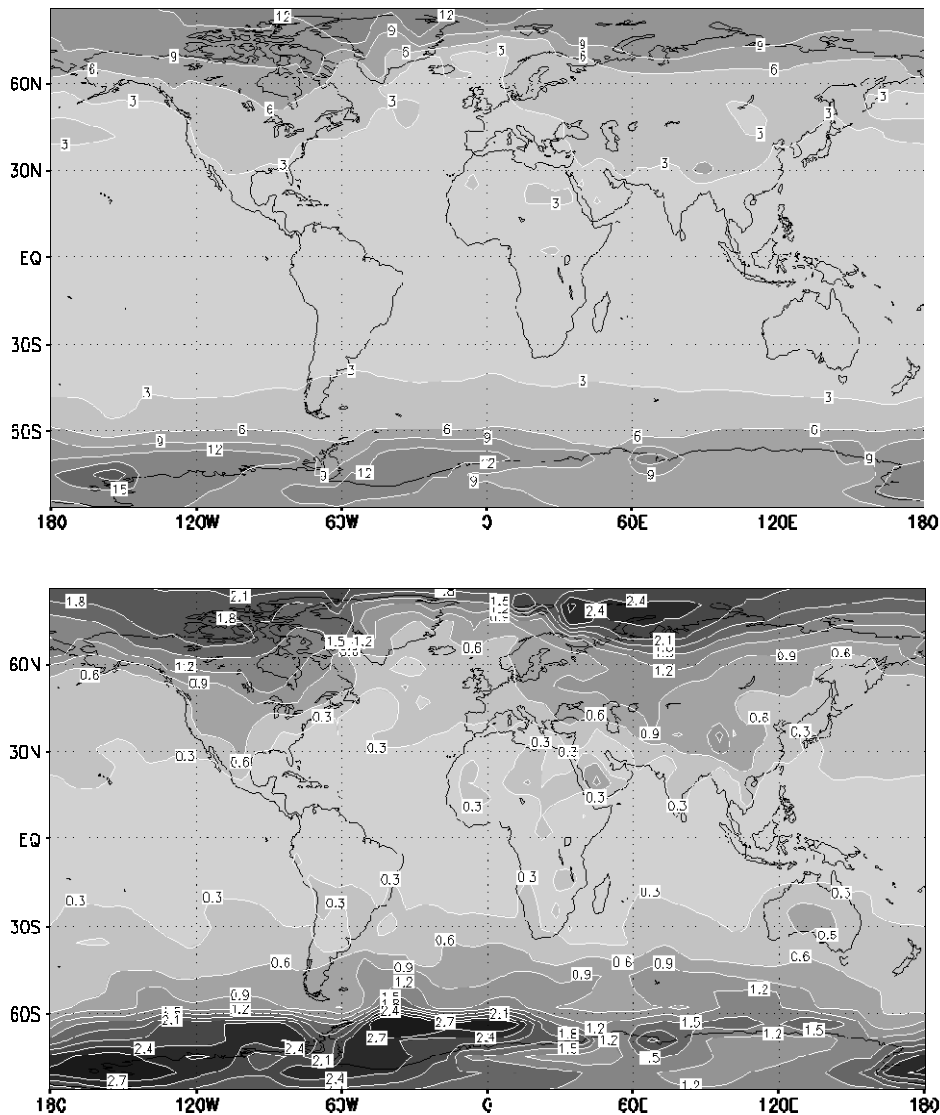


Figure 43: Anomalies of annual mean surface temperature at the end of IS4x1.0 (top) and osp350 (bottom). The anomalies are computed as the difference between the last 50 years of IS4x1.0/osp350 and the last 50 years of CTL. The contour interval is 3°C in the top panel and 0.3°C in the bottom panel.

Ocean temperature

The global mean ocean temperature is enhanced by 0.2°C at the end of osp350, which corresponds to a heat uptake of 1.15×10^{23} J. The highest scenario, A2, has not reached an equilibrium, but the warming already amounts to 2.8°C (corresponding to a heat uptake of 1.6×10^{24} J) after two millennia of integration. The associated thermal expansion leads to a sea-level rise ranging between 0.1 and 1.6 m.

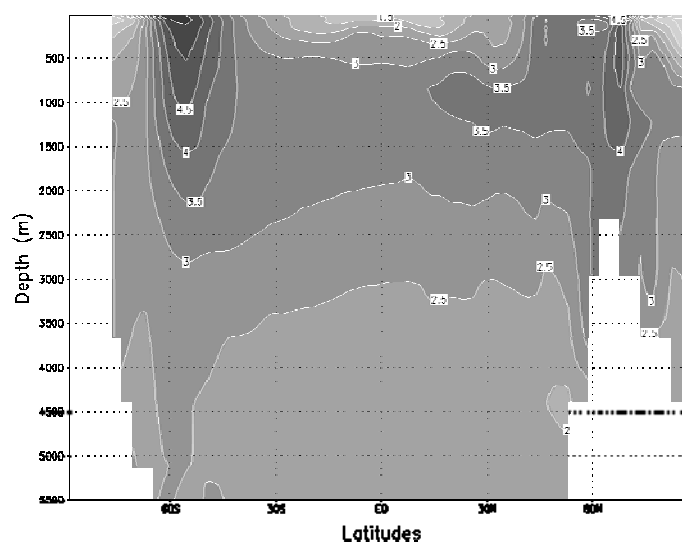


Figure 44: Latitude–depth distribution of the change in zonally averaged, annual mean potential temperature in the World Ocean between the last 50 years of A2 and the last 50 years of CTL. The contour interval is 0.5°C .

The structure of the warming at the end of A2 in the World Ocean is illustrated in Figure 44. Near the surface, the warming is maximum around 55°S and 70°N . In regions of sea ice, at high latitudes, there is a minimum in the warming close to the surface due to the presence of sea ice, which anchors the temperature near the freezing point of seawater. This minimum is rather shallow due to the halocline, which exists under sea ice. A minimum in the warming is also noticed near the surface in the equatorial regions. The weak maximum seen around the depths of 1–1.5 km between 50°S and 50°N is found mainly in the Atlantic Ocean. This is apparently the result of changes in the depth of the outflow of NADW. In spite of these few areas, the uniformity of the warming throughout the entire depth of the World Ocean is remarkable, in agreement with the results of Stouffer and Manabe (2003).

MOC

The warming of the Arctic and North Atlantic Oceans induces a noticeable weakening of the Atlantic MOC at the beginning of each simulation (Figure 45). This occurs when the net radiative perturbation increases with time, causing a decrease in the surface heat loss during wintertime in regions of NADW formation. This initial decrease is followed by a partial or quasi-total recovery in all experiments. For the lowest radiative forcings, the recovery is quasi-total. For the highest radiative forcings, the MOC stays relatively weak for a few hundred years before returning to a

more active state. But, no simulation exhibits a full recovery to the CTL level, even the longest ones.

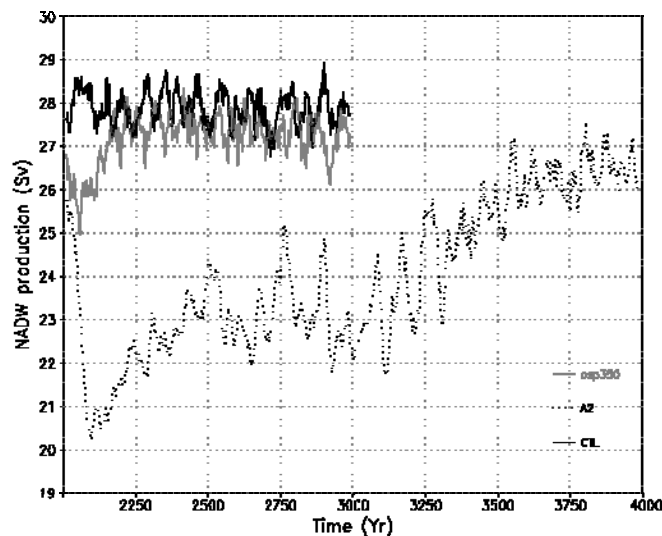


Figure 45: Evolution of the maximum value of the annual mean meridional overturning streamfunction below the surface layer between 45° and 75° N in the Atlantic basin for CTL (black, solid line), osp350 (grey, solid line) and A2 (black, dotted line). A 21-yr running mean has been applied to all time series.

In A2, the MOC remains reduced in year 3000 AD (see Figure 45). At this time, the leading contribution to the density decrease observed at northern high latitudes is clearly freshening (Figure 46). By the end of this simulation, the depth-integrated meridional density gradient is not as small as in year 3000 AD but is still weaker than in CTL. The freshening at northern high latitudes is less pronounced than in year 3000 AD, although still present. This reduces the density anomaly north of 60° N, thus strengthening the NADW cell. The decrease in freshening is mostly due to the reduction in meltwater runoff from Greenland associated with the disappearance of the ice sheet (see Section 5.2.2). All this suggests that the enhanced freshwater flux from the Greenland ice sheet is the main factor responsible for the fact that the MOC remains in a weak state during several centuries. In osp350, the model does not simulate such a large freshening north of 60° N, which is consistent with the fact that the Greenland ice sheet experiences almost no reduction in volume. From the examination of the time series of the export of NADW in all the experiments, we can conclude that all the simulations in Figure 41 seem to be affected by the increased freshwater flux from Greenland, except those in which the atmospheric CO₂ concentration stabilizes at levels lower than 550 ppmv.

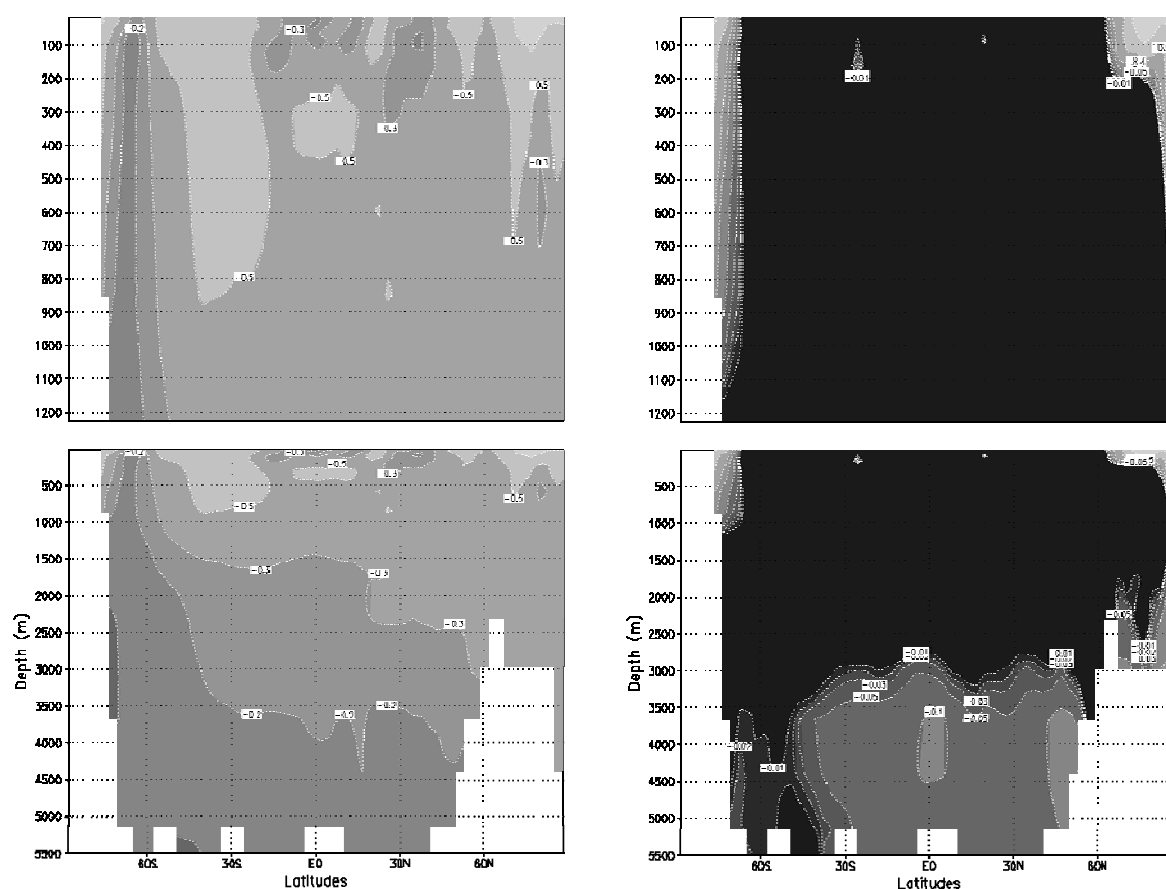


Figure 46: Latitude–depth distributions of the change in zonally averaged, annual mean potential density (left) and of the salinity contribution to this change (right) in the Atlantic basin at the end of A2. The changes are computed as the difference between years 2950–3000 AD of A2 and the last 50 years of CTL. Units are kg m^{-3} .

The NADW cell at the end of A2 is still slightly weaker and shallower than in CTL (Figure 47). In short, one can say that the sharp weakening of the MOC at the beginning of the simulation is not a collapse but an adjustment of the oceanic circulation to the radiative perturbation imposed by the atmosphere. Later, the MOC seems to respond to the Greenland freshwater forcing by a slight decrease of the NADW cell intensity at 30° S. The perturbation lasts until this freshwater forcing has significantly decreased. The MOC then recovers. The recovery is not complete because the freshening at northern high latitudes persists due to, for instance, sea-ice melting, the intensification of precipitation or a change in oceanic circulation.

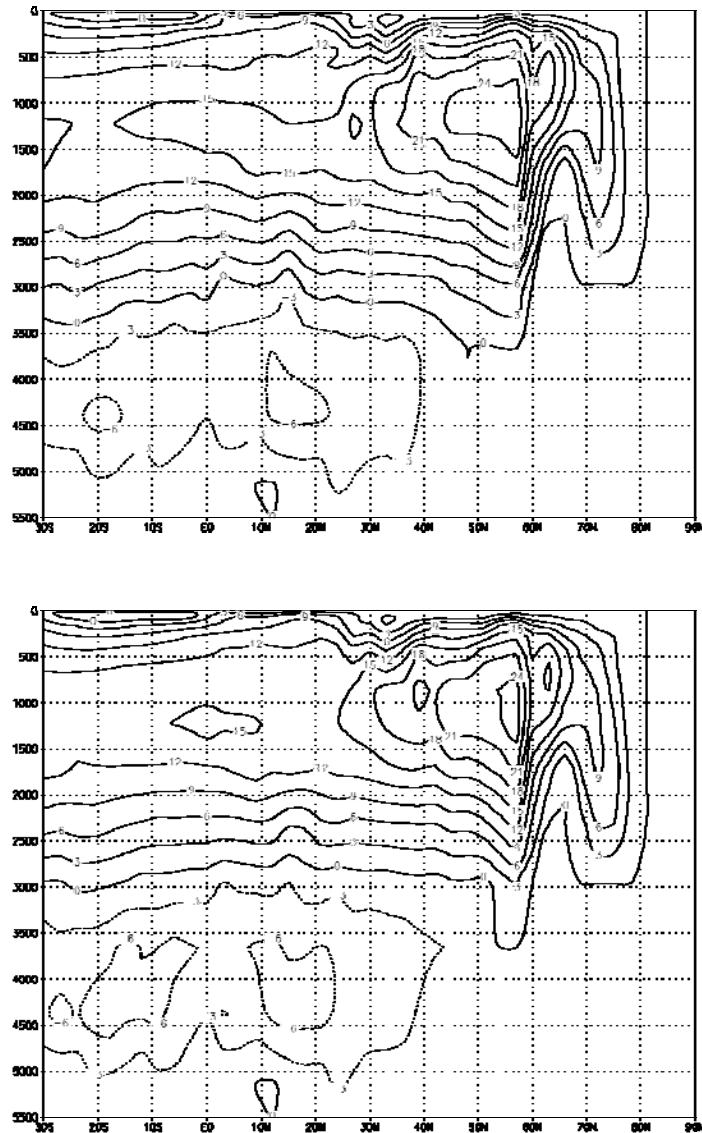


Figure 47: Annual mean meridional overturning streamfunction in the Atlantic basin averaged over the last 50 years of CTL (top) and A2 (bottom). The flow is clockwise around solid contours. The contour interval is 3 Sv.

Sea ice

In summer, the various experiments exhibit a wide range of sea-ice responses in the Northern Hemisphere. Osp350 shows only a slight modification in effective sea-ice area, while sea ice has almost completely disappeared from the Arctic Ocean at the end of A2 (Figure 48). It is also worth stressing that the relationship between the radiative forcing and the change in effective sea-ice area is far from being linear. Figure 49 displays the position of the summer sea-ice edge in the Arctic after 1000 years of integration for four forcing scenarios. At that time, the sea-ice cover is already considerably reduced in A2. A small ice pack nevertheless remains in the

East Siberian Sea, probably because of the overestimated ice thickness in this sector in CTL. In the other experiments, the summer sea-ice cover appears more extensive. So, no simulation predicts an ice-free Arctic Ocean during summertime at the millennium time-scale.

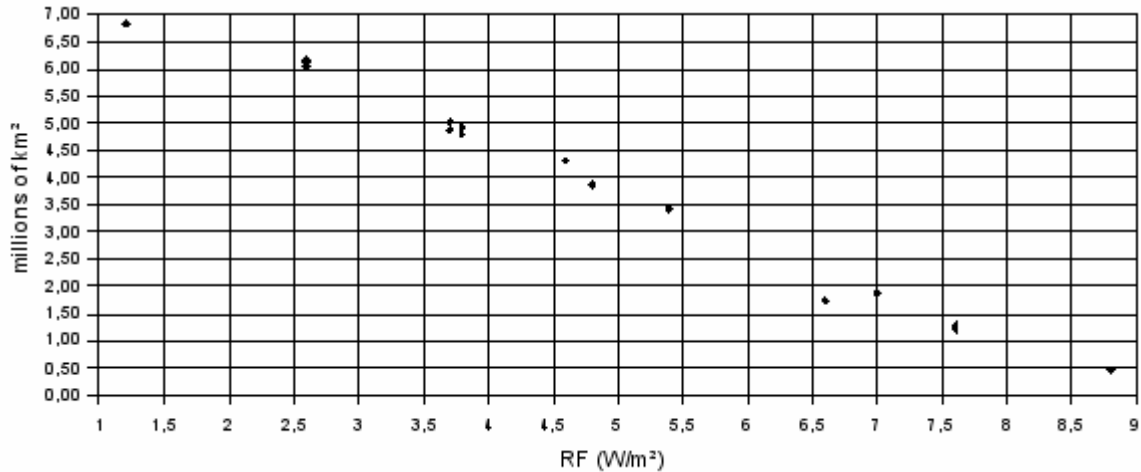


Figure 48: Radiative forcing versus Arctic effective sea-ice area in August averaged over the last 50 years of the experiments included in Figure 41.

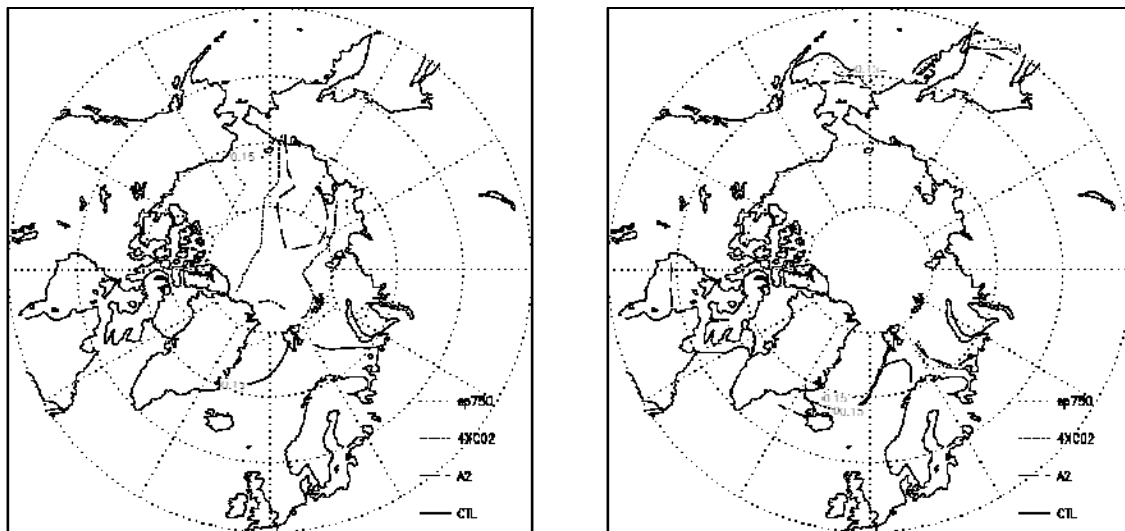


Figure 49: Positions of the Arctic sea-ice edge during September (left) and March (right) after 1000 years in CTL, sp750, IS4×1.0 and A2. The sea-ice edge is defined as the 15% ice concentration contour.

The response of the Arctic sea ice in winter is much less spread across the experiments. No scenario shows a decrease in effective ice area larger than 30% at the end of the model integration. Experiments A2 and IS4×1.0 present an increase in sea-ice areal coverage starting after 500 and 1000 years, respectively (Figure 50). This behaviour is associated with an expansion of the ice cover in the Iceland Sea at that time (see Figure 49). A temporary weakening of deep convection in this region is responsible for this feature. In parallel, a northward retreat of the ice pack is simulated in Hudson Bay and in the Barents Sea as a consequence of global warming. Later, the ice edge also moves northwards in the Iceland and Greenland Seas.

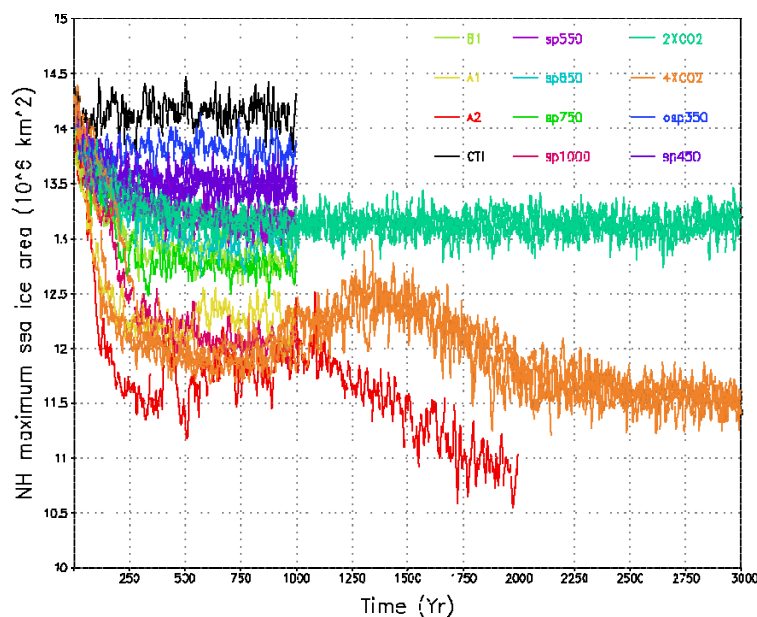


Figure 50: Evolution of the Arctic effective sea-ice area at the time of the winter maximum for a number of experiments. A 10-yr running mean has been applied to all time series. Year 0 corresponds to the beginning of each simulation.

In the Southern Ocean area, the characteristic time-scale of the ocean–sea-ice system is rather large (e.g., Goosse and Renssen, 2005). Figure 51 reveals that, in this region, only the sea-ice packs in CTL, osp350, sp450, IS2×1.0, IS4×1.0 and A2 can be considered as being at equilibrium.

Like in the Northern Hemisphere, during summertime, the sea-ice response in the Southern Hemisphere strongly depends on the radiative forcing (Figure 52). Here again, this response is not linear. Interestingly enough, the Antarctic sea ice experiences larger changes than the Arctic one. For instance, at the end of osp350, the decrease in effective ice area in the Northern Hemisphere amounts to only ~10%, whereas it reaches about 50% in the Southern Hemisphere. At the end of A2, sea

ice has disappeared everywhere in summer except off the Ross and Filchner-Ronne ice shelves. In the other experiments, some additional ice remains in the western Ross Sea.

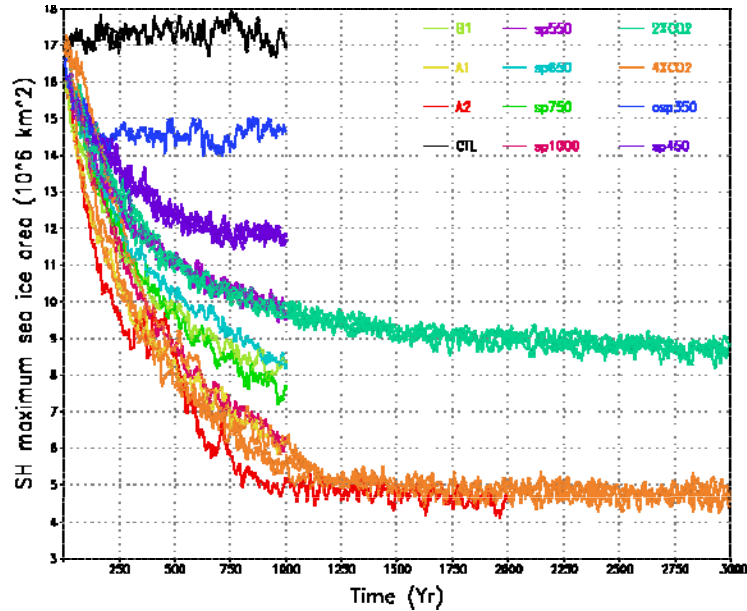


Figure 51: Evolution of the Antarctic effective sea-ice area at the time of the winter maximum for a number of experiments. A 10-yr running mean has been applied to all time series. Year 0 corresponds to the beginning of each simulation.

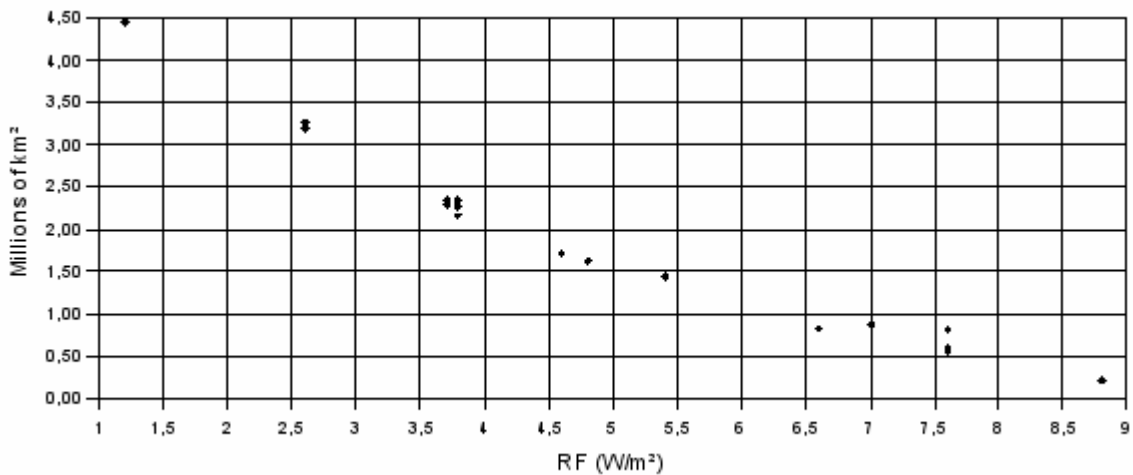


Figure 52: Radiative forcing versus Antarctic effective sea-ice area in February averaged over the last 50 years of the experiments included in Figure 41.

During wintertime, the reduction in sea-ice areal coverage is very significant in the Southern Hemisphere. In contrast with the Northern Hemisphere where the

decrease is rather modest, the shrink of the ice pack ranges from 15% to 70% (Figure 51). This reduction is observed all around Antarctica, with a complete disappearance of the ice cover from 15° E to 60° E and from 120° E to 150° E at the end of A2. Flato et al. (2004) have shown that the majority of CGCMs participating to CMIP2 also predict a larger decrease in sea-ice areal coverage in the Southern Hemisphere than in the Northern Hemisphere. The decrease in annual mean sea-ice extent averaged over all CGCMs amounts to 2×10^6 km² after 70 years of a IS2x1.0-like experiment. LOVECLIM simulates a reduction of only 1×10^6 km² in the same conditions.

Vegetation

On a global average, a forest expansion and an increase in grass area is noticed in all experiments (Figure 53). Actually, the vegetation cover becomes larger in four main areas: the Sahara desert, the Gobi desert, over the high-latitude Eurasian and American continents, and in Greenland. The greening of Greenland depends of course on the degree of melting of the ice sheet. Greenland is therefore not completely green in the simulations still presenting at the end a non-negligible fraction of ice. In osp350, for instance, only a few grid cells in South Greenland become greener.

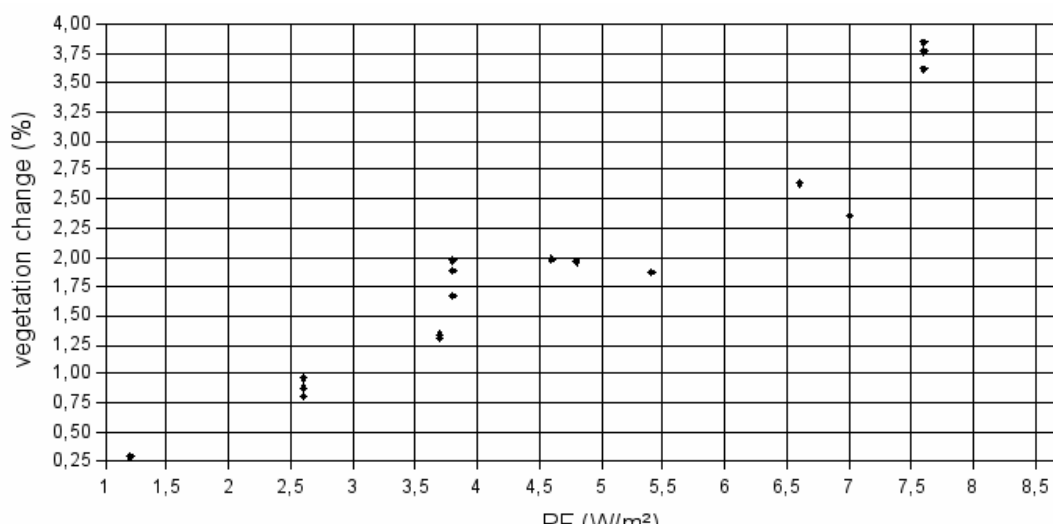


Figure 53: Radiative forcing versus change in globally averaged, annual mean vegetation fraction. Each dot represents one particular simulation of Figure 41. The change in vegetation fraction is computed as the difference between the last 50 years of each transient experiment and the last 50 years of CTL.

The Sahara and Gobi deserts are substantially greener at the end of our simulations. The precipitation increase makes the conditions more favourable to vegetation growth there. The mean vegetation and precipitation in these regions show indeed the same temporal evolution. The precipitation change could be a consequence of the change in vegetation through modifications of evaporation or temperature. As our model does not take evapotranspiration into account, the effect of vegetation on evaporation is limited to the temperature effect in LOVECLIM. However, the temperature curve (not shown) does not have the same shape as the precipitation curve. Precipitation can then be considered as the leading factor for this vegetation expansion. Voldoire (2005) found the same behaviour over Sahara under the SRES A2 forcing scenario in a CGCM coupled to a much more comprehensive vegetation model than ours. Furthermore, Cramer et al. (2001) examined the response of six dynamical vegetation models to an increase in atmospheric CO₂ concentration to 800 ppmv until the end of the 21st century. They reported a northward displacement of the southern limit of the Sahara desert as well as a shrink of the Gobi desert, in accordance with our results.

The tree line in the model northern high latitudes moves northwards except in a small region north of America, where the growing degree-day (GDD) and precipitation remain rather low. Grass (i.e. tundra) also expands in regions where bare soil previously prevailed. The limiting factor that prevents vegetation to expand in those areas under present-day conditions is the GDD index. The warming, helped by an increase in precipitation, is thus assumed to be the main cause of this greening at high latitudes. Similar results were found by Voldoire (2005) and Cramer et al. (2001), except in northern North America, where the boreal forest was observed to expand. There is some proxy and modelling evidence that the boreal forest spread further north during the early Holocene (Brovkin et al., 2002; Renssen et al., 2005), when the temperature was higher in summer. Moreover, the forest expansion is thought to be responsible for an amplification of the warming (Foley et al., 1994) and, consequently, of the precipitation in that latitudinal belt.

The greening of Greenland is associated with the ice-sheet retreat. The warming induces the melting of the ice, which is replaced by less-reflecting vegetation, thus enhancing the initial warming. Moreover, the melting of the ice substantially lowers the Greenland topography leading to an adiabatic heating. The conditions are then more favourable for vegetation. At the end of A2, Greenland is almost entirely covered by vegetation, tundra everywhere and forest along the southern and eastern coasts. An increase in precipitation over the eastern coast contributes to the tree growth there. Lunt et al. (2004) also studied the effect of a disappearance of the Greenland ice sheet on climate in a CGCM. They removed the ice sheet in their model, allowing for isostatic rebound, and kept the atmospheric CO₂ concentration to

its present-day level. They also found a growing of forest south of Greenland, but, contrary to our results, they obtained an expansion of trees along the western coast.

North America undergoes a decrease of vegetation in the region of the Great Plains from 10% in osp350 to 30% in A2 compared to CTL. This feature is due to a reduction in rainfall during summertime.

5.2.2. Ice sheets, glaciers and sea level

As the results for the continental cryosphere and sea level are similar for similar warmings and scale well with the rate and amount of radiative forcing, we discuss here the results of only a few LOVECLIM runs. The most interesting scenario for investigating the response of the polar ice sheets is the one in which the atmospheric CO₂ concentration rises to four times its pre-industrial value at a rate of 1% per year and is kept constant after that for a total duration of 3000 years (IS4×1.0). This scenario is at the higher end of currently available scenarios but, by no means, extreme as a 4×CO₂ level is likely attained by the end of this century or the beginning of the 22nd century if no drastic measures to curb present-day emissions are taken. This experiment ensures that a wide range of possible future climate scenarios is crossed and is long enough for the ice sheets to exhibit a meaningful dynamic response. Moreover, the results can be compared with studies with other coupled models under the same radiative forcing conditions (e.g., Ridley et al., 2005). The initial condition for this 4×CO₂ experiment was the pre-industrial reference state (CTL) at year 1500 AD.

Figure 54 shows the radiative forcing in this experiment as well as the ensuing mean annual temperature changes predicted by the model over the ice sheets. These temperature changes are taken as the spatial average over all of the Greenland continent and all of the grounded ice of the Antarctic ice sheet, respectively. Over both ice sheets, this scenario eventually leads to warmings of about 10°C, half of which is reached within the first two to three centuries. These warmings are about a factor three higher than the global average of a little more than 3°C (see Section 5.2.1) because of the polar amplification seen in LOVECLIM. Such a polar amplification is a robust characteristic of the climate system but is stronger in LOVECLIM than in most other models. Gregory and Huybrechts (2006) typically found a polar amplification of around 1.5 for a representative suite of IPCC AR4 CGCMs. The stronger polar amplification in LOVECLIM nicely combines with its lower climate sensitivity to yield polar temperature changes for a given radiative forcing that are much more in line with the more comprehensive CGCMs.

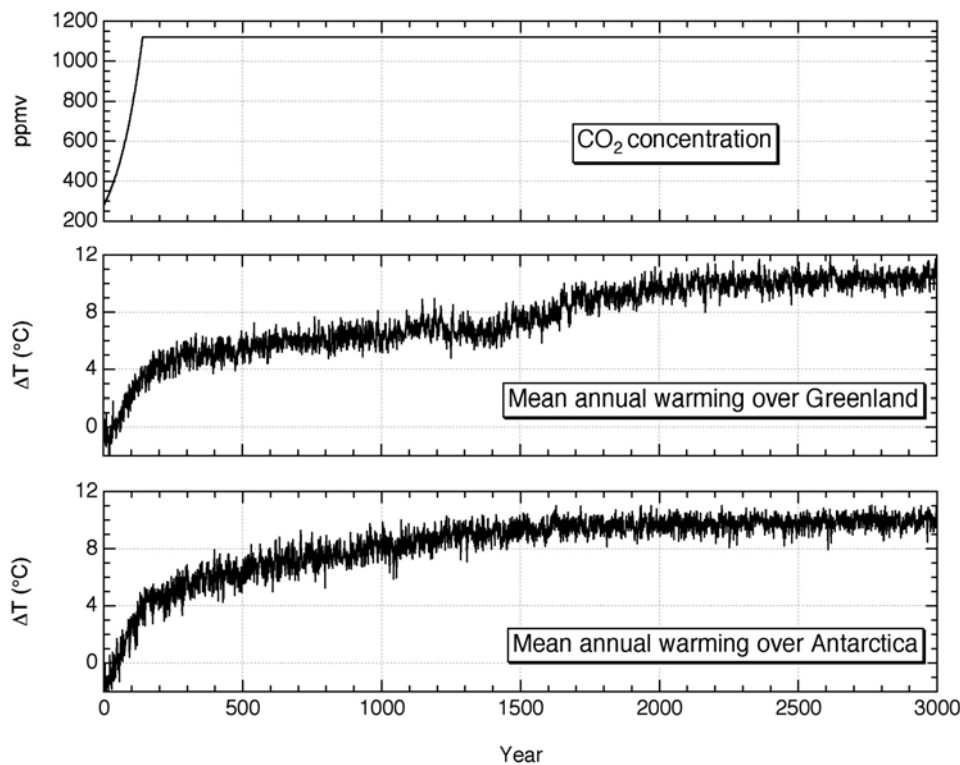


Figure 54: Evolutions of the atmospheric CO₂ concentration and of the mean annual temperature change over the polar ice sheets in the 4×CO₂ experiment discussed in this section. The starting time is the pre-industrial state at 1500 AD.

The most drastic response to a sustained 4×CO₂ forcing concerns the fate of the Greenland ice sheet. Whereas for present conditions the volume of meltwater runoff is only half the volume of snow accumulation, under 4×CO₂ conditions the threshold for a balanced surface budget is quickly reached, and runoff entirely dominates the freshwater budget of the Greenland ice sheet (Figure 55). Peak runoff rates approach 0.1 Sv for a volume which is up to a factor 10 larger than the snow accumulation. Calving becomes negligible after two centuries because the ice sheet no longer borders the ocean. The freshwater fluxes decrease after about 1200 years when the ice sheet becomes smaller. After 3000 years, the Greenland ice sheet almost entirely disappears, ultimately causing a global sea-level rise of about 8 m, at a peak rate of 6 mm per year or 60 cm per century. At this time, the freshwater budget of Greenland can no longer draw on the ice reservoir and the total freshwater flux equals the yearly runoff from the ice-free tundra. Our time-scale for ice-sheet decay compares well with the one found in a similar 4×CO₂ simulation made with a CGCM coupled to the same Greenland ice-sheet model as ours (Ridley et al., 2005), indicating similar levels of climate change and mechanisms of response.

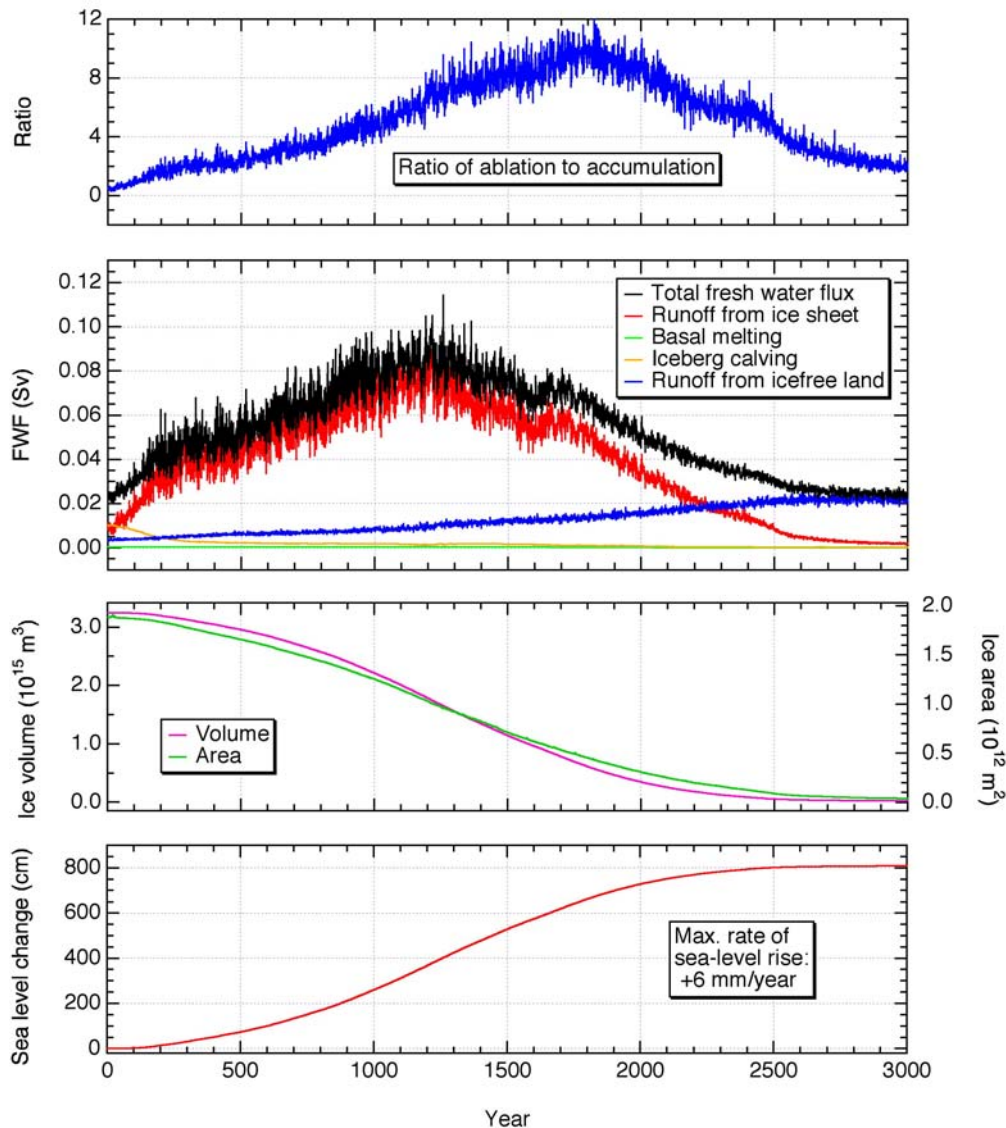


Figure 55: Response of the Greenland ice sheet to $4\times\text{CO}_2$ climate forcing during 3000 years. Shown are changes in ice-sheet size and mass-balance components. FWF is the freshwater flux expressed in Sv.

Snapshots of the retreating ice sheet are given in Figure 56. These show how the ice-sheet retreat first occurs in the southwest, where already today a 300-km wide band of tundra is present. After several centuries of retreat, the Greenland ice sheet becomes fully land-based. The central dome survives longest at an almost constant elevation of around 3000 m. This makes the ice-sheet flanks steeper and the ice flow faster to accommodate for the higher mass-balance gradients in a warmer climate. The steeper margins represent a counteracting effect on the ice-sheet retreat. They dynamically reduce the area below the equilibrium line and thus reduce the area over which runoff can take place. Compared to experiments without this effect, the ensuing rate of ice-sheet decay is about 20% smaller (Huybrechts and de Wolde, 1999; Huybrechts et al., 2002). The ice sheet ultimately retreats to the eastern

mountains, gradually exposing bare land which can heat up much more during the summer than the ice cover because of a lower albedo, which process is responsible for the second step observed in Greenland warming simulated after the year 1500 (see Figure 54). As the Greenland ice sheet retreats, the bedrock slowly rebounds with a characteristic time lag of several thousand years. Initially, this causes a series of big inland lakes on beds below sea level. After 3000 years, almost all initial areas depressed below sea level have risen above sea level, but several endogenous depressions without exit to the ocean still exist, as can be seen in the series of pictures in Figure 56.

It is of large interest to find out whether the decay of the Greenland ice sheet can be reversed once set in motion in case climatic conditions were to return to near present-day conditions. Experiments conducted by Toniazzi et al. (2004) suggest that the Greenland ice sheet would not regrow on an ice-free continent under pre-industrial conditions. This indicates hysteresis with two stable states: the current ice sheet and no ice sheet. If so, it also means that there must be a point-of-no-return along the disintegration path beyond which the ice-sheet decay becomes self-sustained and cannot be halted even by a cooling climate. The experiments performed with LOVECLIM so far are however not able to conclusively answer this question. The three experiments with reversing CO₂ concentrations (IS4×0.5R1.0, IS4×1.0R1.0, IS4×2.0R1.0; see Figure 38) made the ice sheet grow again concurrent with the applied cooling. Apparently, only 280 years of increased warming to 4×CO₂ levels (experiment IS4×0.5R1.0) is insufficient to cross such a point-of-no-return, if at all it were to exist. In the latter experiment, Greenland ice volume is only reduced by maximally 2.5% after 400 years of integration, and the shrinkage in area is only 4%. After that, the pre-industrial ice-sheet configuration is gradually restored over a time period of several centuries.

For the Antarctic ice sheet, the response is much less drastic than for the Greenland ice sheet. But also here, we see an accelerated reduction in ice volume and ice area after 200 years of warming (Figure 57). After 3000 years of 4×CO₂ forcing, the Antarctic grounded ice volume and area are reduced by 8% and 4%, respectively. This corresponds to a total sea-level rise of 4.2 m, less than the volume loss suggests as part of the lost ice has been merely replaced by ocean water. The mechanisms responsible for this shrinking behaviour are an increase in surface meltwater runoff from the grounded ice sheet and of the melt below the ice shelves. Under the applied 4×CO₂ forcing, we also find a large dampening effect from the Southern Ocean. Oceanic heat input eventually leads to quadrupling of the average ice-shelf melt rate, but on a time-scale of centuries given by the thermal inertia of the ocean. This increase seems low compared to some studies indicating up to a tenfold increase for a 1°C ocean warming (Shepherd et al., 2004).

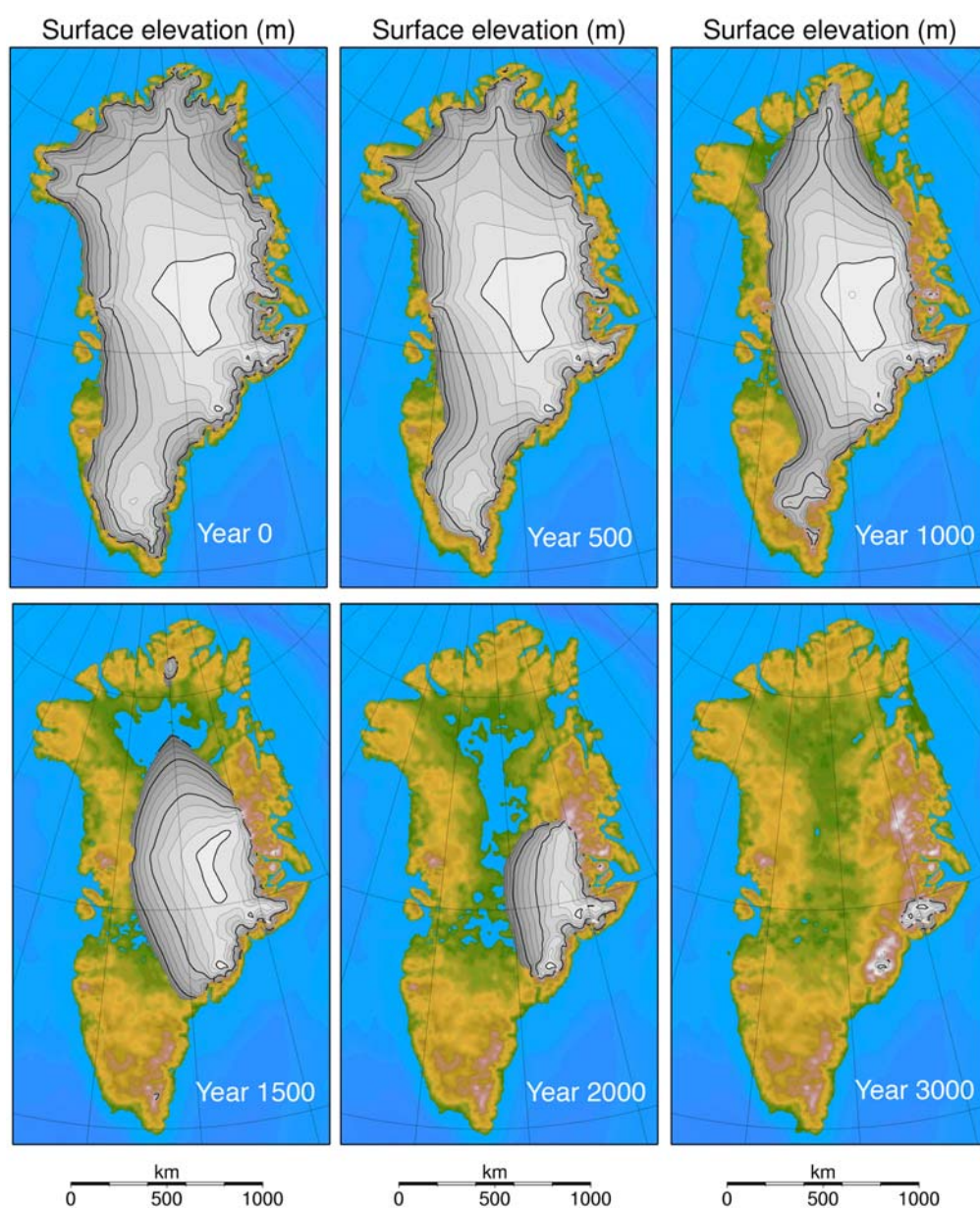


Figure 56: Snapshots of the Greenland ice-sheet evolution under $4\times\text{CO}_2$ climate forcing during 3000 years. Shown is surface elevation. Blue colours are for the ocean and land below sea level, the brown and green colours represent ice-free tundra and grey colours are for the ice sheet. Contour interval over the ice is 250 m, the thick lines are for every 1000 m of surface elevation.

However, the scheme developed here applies to average conditions for the cavities under the big ice shelves and is probably less valid for ice shelves in direct contact with ocean water at intermediate depths. The latter ice shelves, one example being the much studied Pine Island Bay glacier tongues, already experience today high melt rates in excess of several tens of meters per year (Rignot and Jacobs, 2002). Conditions below the three large ice shelves (Ross, Amery and Ronne-Filchner ice shelves) differ substantially, and areas of moderate melting co-exist

with areas of basal accretion (Oerter et al., 1992; Gerdes et al., 1999). So far, a clear relation between climate change, oceanic circulation and basal melting rates has however proven hard to establish (Williams et al., 1998).

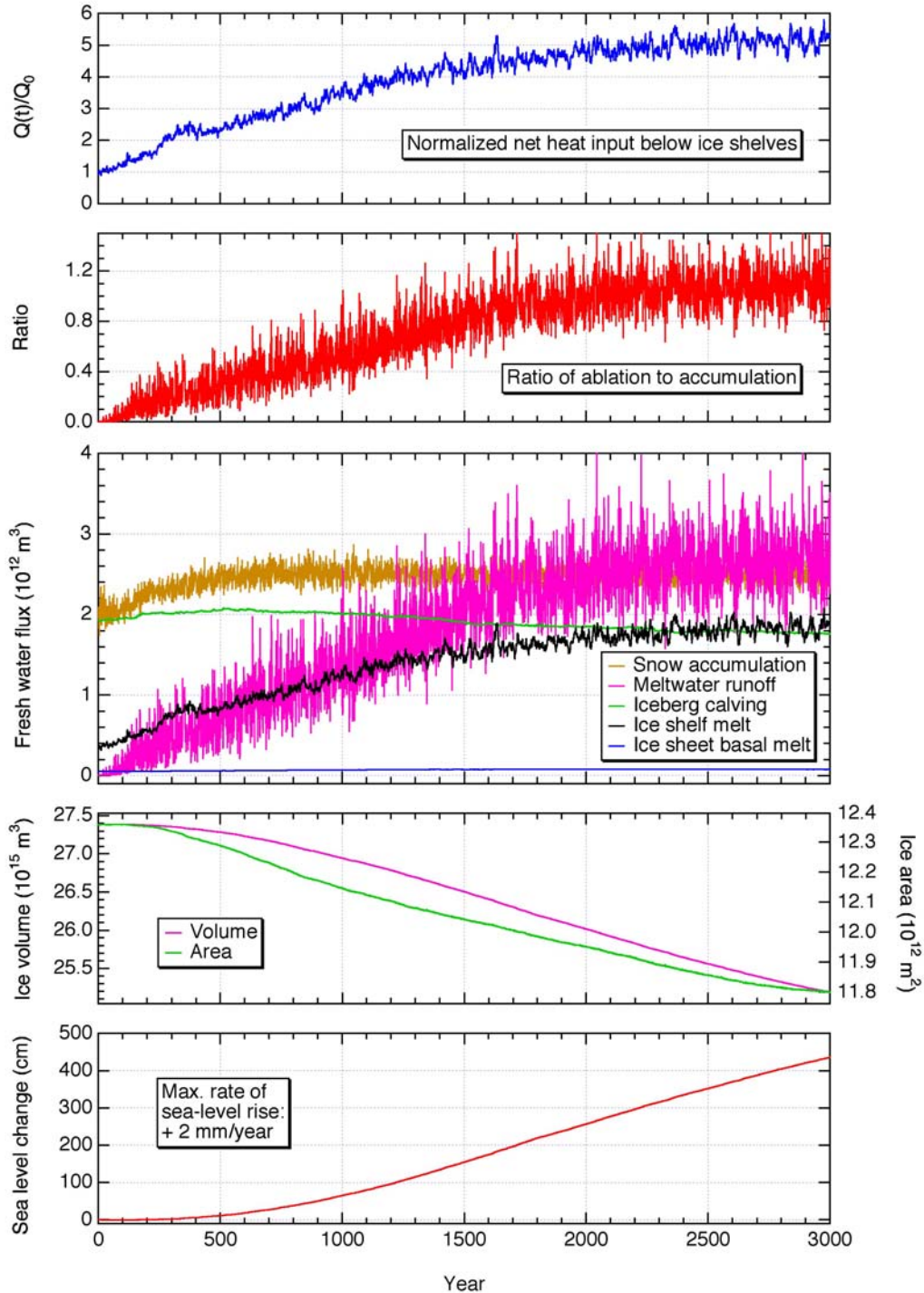


Figure 57: Response of the Antarctic ice sheet to $4\times\text{CO}_2$ climate forcing during 3000 years. Shown are changes in mass-balance components and the ensuing changes in ice-sheet size.

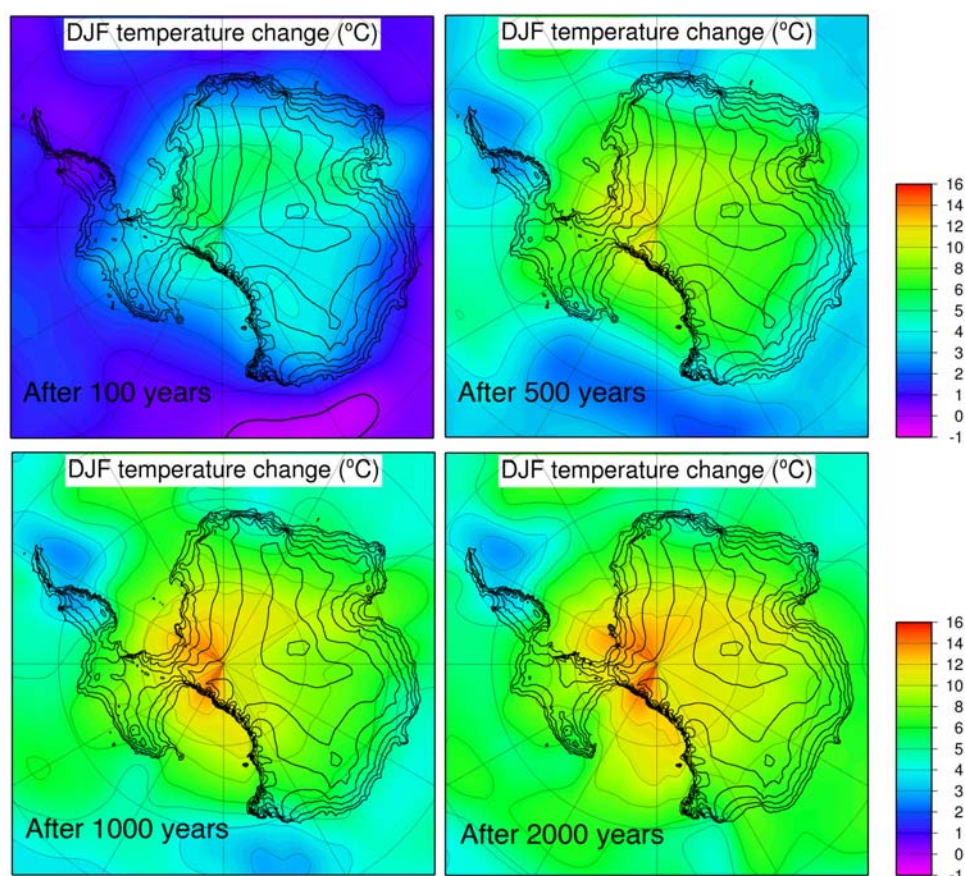


Figure 58: Summer temperature anomalies over Antarctica as predicted by LOVECLIM under sustained $4\times\text{CO}_2$ conditions starting at year 0.

Although surface melting on Antarctica does not play a very large role for the next few centuries, Figure 57 also demonstrates how this component gradually becomes more important, and ultimately becomes as important as surface accumulation, long after the forcing has stabilized and equally on a time-scale controlled by the ocean. To our knowledge, this is the first time that so much surface melting in simulations of the future evolution of the Antarctic ice sheet has been seen. The reason is the delayed warming of the ocean which takes place on a time-scale of many centuries but ultimately causes a coastal warming by up to $10\text{ }^\circ\text{C}$ (Figure 58). In that case, surface conditions along the Antarctic ice-sheet margin take on characteristics of the present-day Greenland ice sheet. At the same time, the accumulation increase is much weaker than can be expected on purely thermodynamic grounds, which suggest a 5 to 10% increase per $^\circ\text{C}$ concomitant with a Clausius-Clapeyron type of argument linking precipitation rates to the saturated vapour pressure, and found to be valid for glacial-interglacial climate shifts in results from ice cores (e.g., Robin, 1977).

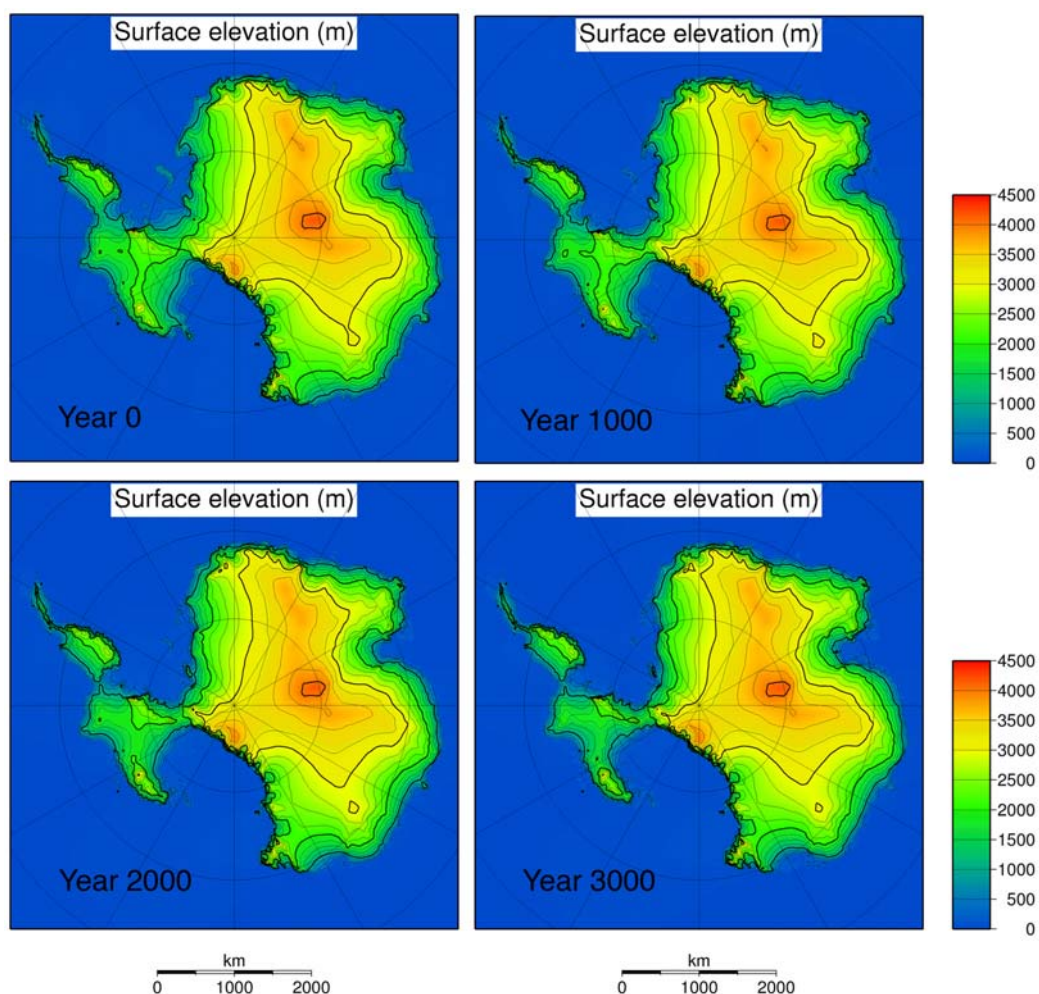


Figure 59: Snapshots of the Antarctic ice-sheet evolution under $4\times\text{CO}_2$ climate forcing. Shown is surface elevation. Contour interval is 250 m; the thick lines are for every 1000 m.

On the evolution plots presented in Figure 59, it can be seen that the most important change is grounding-line retreat for the West Antarctic ice sheet and along overdeepened glaciers of East Antarctica. At the millennial time-scale considered here, elevations in central East Antarctica remain largely unaffected. The positive contribution to sea-level rise at a more or less steady rate of 2 mm yr^{-1} indicates that the Antarctic ice sheet is still far from equilibrium with the imposed climate change. In effect, very long time-scales of the order of 10^4 years are required before the Antarctic ice sheet eventually reaches a new steady state with less ice. The response observed here can hardly be called a catastrophic collapse, but is probably an underestimate in case the large ice shelves would break up and calving could take place at grounding lines. These effects are not well represented in the current model, which was developed for generally colder conditions with ice shelves present. It is probably fair to state that this modelling is still in its infancy. In combination with the higher basal melt rates below the ice shelves, it seems unlikely

that in a $4\times\text{CO}_2$ scenario the large ice shelves can be sustained, and they may well disintegrate after 500 to 1000 years (Warner and Budd, 1998). Once again, this experiment seems to bring to light another long-term slow process in the climate system with potentially large consequences that may already be set in motion during the next few decades.

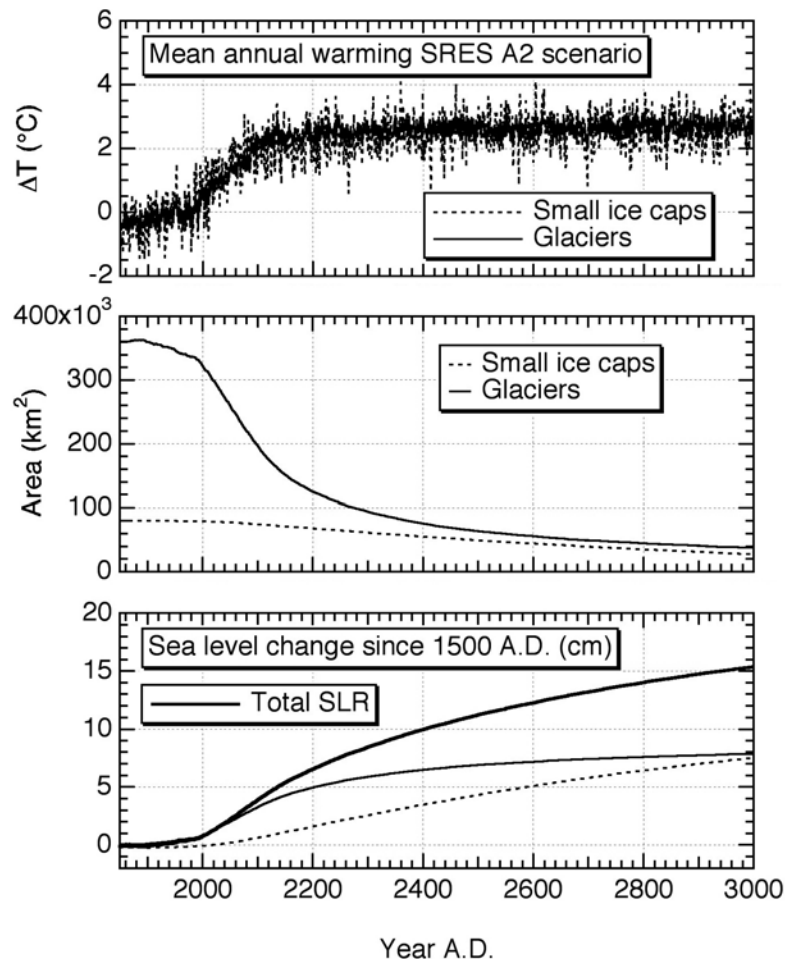


Figure 60: Predicted evolution of mountain glaciers and small ice caps during the 3rd millennium under the low-end SRES B1 scenario. The lower panel shows the total sea-level rise (SLR) from both ice bodies added together.

Concerning the response of the glaciers and ice caps, a climate-change experiment over several thousand years is hardly worth the effort. Even for a low scenario (B1), most of the world’s mountain glaciers disappear within two centuries, and small ice caps largely waste away within a thousand years. The potential sea-level rise is limited to about 20 cm, which is all of the ice in the melt algorithm employed here (Figure 60).

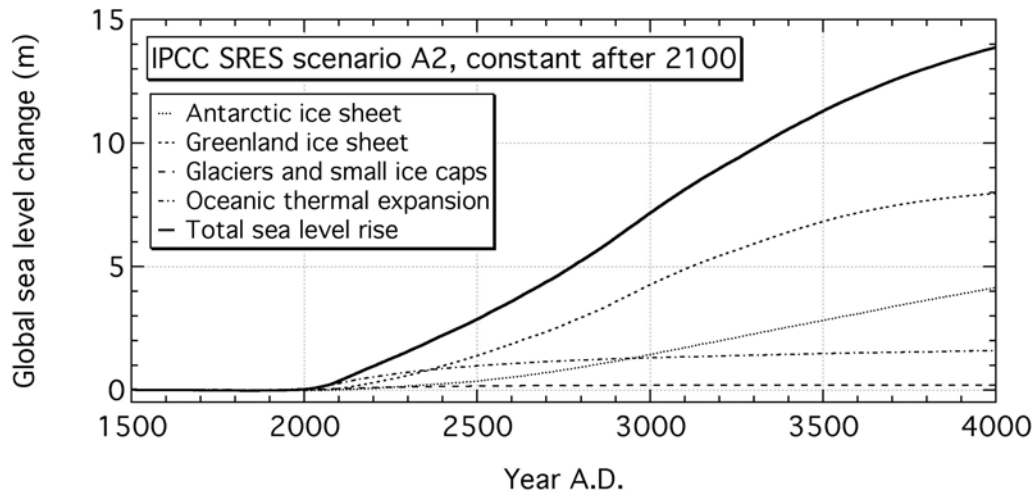


Figure 61: Total predicted sea-level rise and its components after 2000 years of SRES A2 forcing. In this scenario, the radiative forcing stabilizes at about 9 Wm^{-2} , or 1.2 W m^{-2} higher than the second highest forcing applied in the $4\times\text{CO}_2$ experiment.

Figure 61 puts together all major contributors to sea-level change in a LOVECLIM experiment under constant SRES A2 forcing. The radiative forcing applied in this experiment is comparable to a $4\times\text{CO}_2$ experiment. This shows relatively little change during the first hundred years (about 35 cm of sea-level rise), but reaching a maximum rate of 1 m per hundred years around the year 3000 AD. It takes some time for the polar ice sheets to come up to speed, but already after a few centuries of sustained warming, both ice sheets are found to become the dominant contributors to sea-level rise. The Greenland ice sheet is most vulnerable, and after 1000 years of warming, the Antarctic ice sheet takes second place, still rising at an almost linear rate after 2000 years. By the year 3000 AD, sea level in this experiment has risen by 7.15 m. Most of it is due to melting of the Greenland ice sheet (+4.25 m), followed by melting of the Antarctic ice sheet (+1.42 m), thermal expansion (+1.29 m, and stationary) and the contribution from mountain glaciers and small ice caps (+0.19 m). Contributions to sea-level change from other LOVECLIM experiments performed for the 3rd millennium are summarized in Figure 62. From this graph, it can be inferred that it will be very difficult to limit the eventual sea-level rise to less than 1 m after 1000 years, unless the CO_2 concentration can be stabilized to less than twice the pre-industrial value. Such a goal can only be reached by emission reductions far larger than any policy currently pursued.

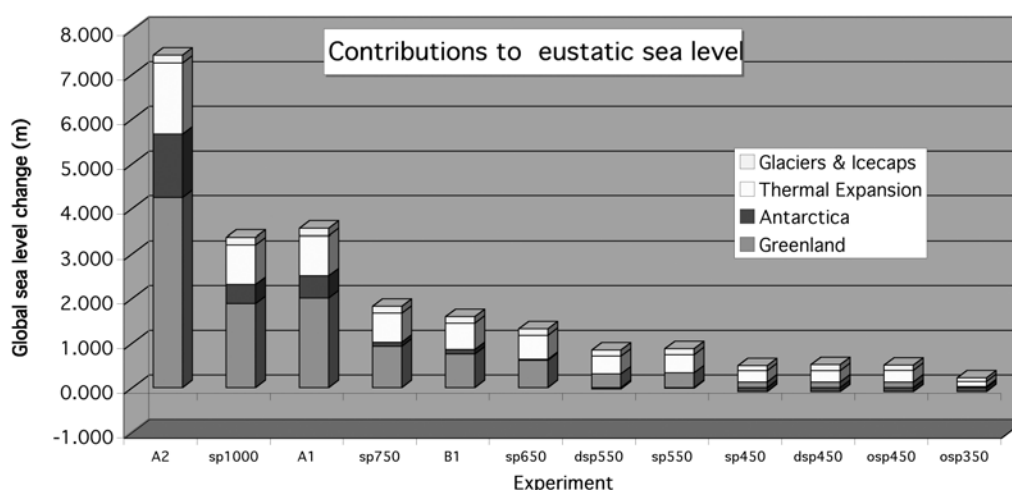


Figure 62: Contributions to global sea-level rise by the end of the third millennium (3000 AD) for some LOVECLIM experiments for which the radiative forcing is shown in Figure 41.

5.3. Sensitivity experiments

5.3.1. Interactions between the Greenland ice sheet and climate

Experimental design

In order to quantify the contribution of the ice sheets to the climate changes simulated by LOVECLIM, two additional experiments were conducted. Both of them were run from year 2000 AD until year 4000 AD, and included the same forcings as in A2. In the first one, named A2NA (A2 No AGISM), AGISM was switched off. In this case, ECBilt computed by itself the mass balance over the ice sheets. It is worth mentioning that continental ice in ECBilt is represented as land with a high albedo, but it cannot melt. Only the snow on its top can melt. For this reason, the runoff from ice sheets cannot increase largely if AGISM is not activated. Moreover, the altitude and albedo of the surface are fixed to the ECBilt reference values. In the second experiment, called A2FA (A2 Fixed AGISM), the climate model (ECBilt–CLIO–VECODE) was forced by constant ice-sheet characteristics corresponding to average conditions for the period 1970–2000 AD, and AGISM was driven off-line by the modelled climate changes. The only difference with A2 lay in the fact that the feedbacks of ice sheets on climate were absent. The differences in results between A2 and A2NA give information about the role of the ice-sheet model in the computed climate. This includes the impact of the ice-sheet changes as well as the influence of the way the ice sheets are represented in the model. On the other hand, the differences in results between A2 and A2FA provide only the impact of the ice-sheet changes. If we assume that the modifications of the climate due to those

contributions are linear, the differences in results between A2FA and A2NA give the climate changes associated with the different ice-sheet representations in ECBilt and AGISM. Obviously, these experiments do not allow separating the effects of the Greenland and Antarctic ice sheets. Therefore, it has to be borne in mind that the changes in the Arctic region and in the Atlantic Ocean area discussed below can be related not only to the Greenland ice sheet but also, to a lesser extent, to the Antarctic ice sheet.

Atmospheric circulation and surface temperature

During the two millennia of the A2 integration, the Greenland ice sheet becomes smaller and thinner. The lowering of the Greenland ice sheet is expected to have an impact on the wind circulation in the Arctic region. Figure 63 displays the geopotential heights for the last 50 years of A2 and A2NA. Large changes are noticed over the Greenland region. In A2NA, there is no interactive ice-sheet model, the topography in this simulation is hence fixed. In this experiment, an anticyclone is present over Greenland. In A2, the Greenland topography lowers because of the ice sheet thinning, the anticyclone declines and winds, instead of turning around Greenland, cross over it. In winter, the Icelandic low deepens and extends over South Greenland. Toniazzo et al. (2004) performed a present-day simulation with a CGCM in which they removed the Greenland ice sheet. They obtained the same circulation modifications in response to the orography changes, i.e. a shift and deepening of the Icelandic low and more zonal atmospheric circulation over Greenland. Also, Lunt et al. (2004) found a strengthening and an expansion of the Icelandic low at 500 hPa during winter in their CGCM when they removed the Greenland ice sheet.

The changes in the surface topography of the Greenland ice sheet also influence, although to a lesser extent, the Arctic atmospheric circulation. In particular, the westerlies over West Siberia are weakened. The climate in central Siberia during winter is colder and drier than in western Siberia in the model. The weakened westerlies there induce a westward expansion of the central Siberia air mass. This signal is strong and can be seen on an annual average, but it is maximum in late winter and early spring (Figure 64). This atmospheric circulation modification generates a negative temperature anomaly in western Siberia, which extends westwards to Scandinavia and southwards to 45° N. Figure 64 indicates that the surface temperature differences between the last 50 years of A2 and A2NA reach 5°C on average in February, March and April. This is the only major impact that can be attributed with a high level of confidence to the changes in wind patterns. In the GIN Seas, the atmospheric circulation is highly perturbed, but this does not seem to deeply affect the oceanic currents there. It should be noted that Lunt et al. (2004), Ridley et al. (2005) and Toniazzo et al. (2004) found a winter cooling centered in the

Barents Sea in their deglaciation experiments, that Toniazzo et al. (2004) attributed to changes in storm tracks.

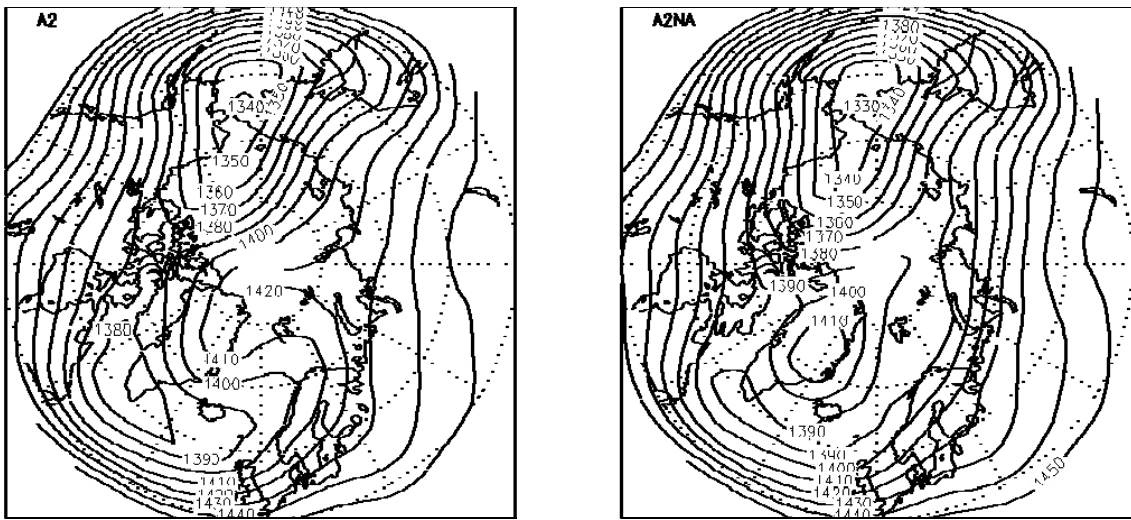


Figure 63: Annual mean 800 hPa geopotential heights for the last 50 years of A2 (left) and A2NA (right). The contour interval is 10 m.

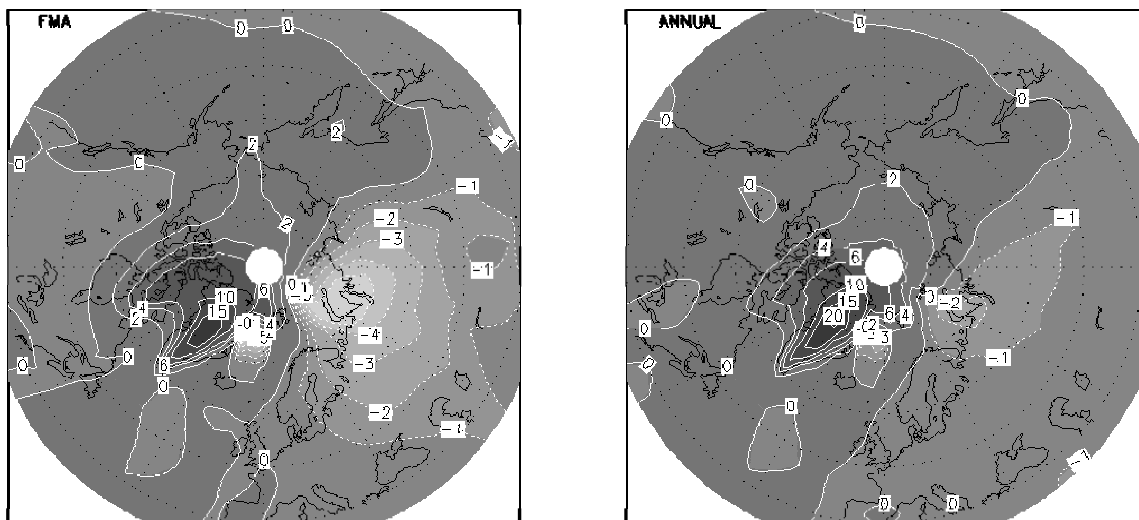


Figure 64: Surface temperature differences between the last 50 years of A2 and A2NA during February–March–April (left) and on an annual average (right). The contour interval is not constant. Units are °C. The contribution of the surface altitude changes is taken into account.

The lowering of the Greenland ice sheet is also supposed to warm surface air by adiabatic heating. It is worth stressing that the variations of surface temperature discussed here take into account the changes in surface altitude. In year 4000 AD of

A2, the altitude decrease compared to CTL reaches 2800 m in central Greenland. The albedo–temperature feedback is absent in December–January–February since Greenland receives nearly no incoming solar radiation during this time period. Assuming there is no winter change in heat advection between the ends of integrations A2 and A2NA (like in Ridley et al., 2005), the elevation contribution to the surface temperature increase at the end of A2 can be approximated. The temperature difference for December–January–February between the ends of A2 and A2NA amounts to $+4.3^{\circ}\text{C}$. In June–July–August, the temperature increase associated with albedo change is therefore $\sim 6.2^{\circ}\text{C}$ on average over the Greenland, since the additional warming present in A2 compared to A2NA is 10.5°C . Thus, the albedo–temperature feedback is found to be dominant in summer as in Lunt et al. (2004). Figure 65 depicts the changes in annual mean surface albedo over Greenland between the ends of experiments A2 and A2NA.

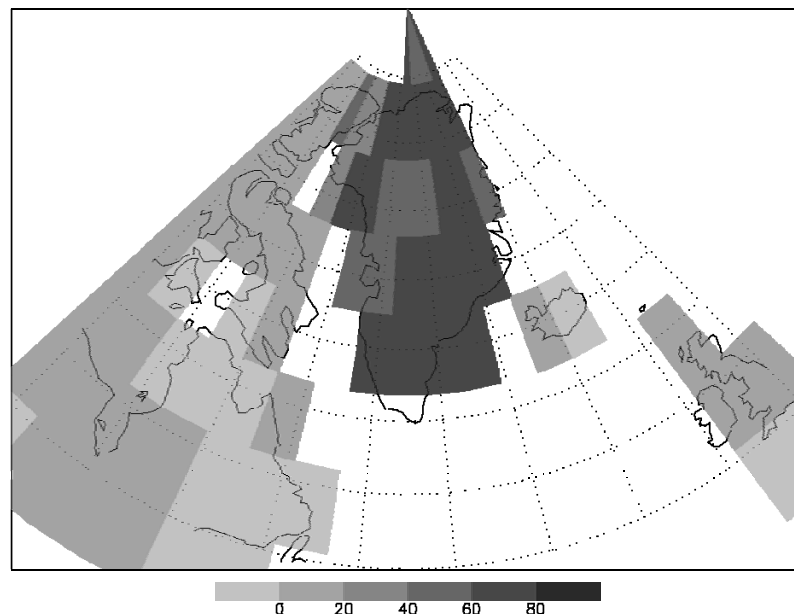


Figure 65: Changes in annual mean surface albedo between the last 50 years of A2 and A2NA. Units are %.

The albedo decrease ranges from 40% to 70%. The ice-free land becomes partly covered by grassland or forest. The strongest albedo changes are observed at locations where a large fraction of grid cell becomes covered by forest (South and East Greenland) in the warmer climate. Since the total incoming solar radiation reaches approximately 80 W m^{-2} on an annual average, those albedo changes yield a radiative perturbation at surface ranging between 30 and 55 W m^{-2} . The Canadian Archipelago and the Arctic Ocean experience a warming in A2 compared to A2NA (see Figure 64). This behaviour is partly due to the amplification of the Greenland

warming taking place in A2. The intensification of the warming over the Canadian Archipelago might also result from the decline of the Greenland anticyclone. This anticyclone is responsible for a transport of Arctic air towards Canada in CTL during winter months. At the end of A2, the Canadian Archipelago receives heat from Baffin Bay thanks to the modification of the atmospheric circulation (see Figure 63).

Freshwater input and its impact on deep convection

The melting of the Greenland ice sheet represents an additional freshwater input to the ocean surrounding the island. The difference in total freshwater flux from Greenland amounts to +0.08 Sv on an annual average during the period 2900–3000 AD between A2 and A2F2. This period has been chosen for the comparison because it corresponds to the period during which the meltwater flow from Greenland is maximum in A2. The difference between A2FA and A2NA lies mainly in the geographical distribution of the freshwater flux around Greenland: the freshwater input is reduced at the end of A2NA compared to the end of A2FA at the southern tip of Greenland and enhanced in Baffin Bay as well as in Denmark Strait (not shown). This has only a small effect on salinity in comparison with the changes obtained in A2.

Figure 66 show the anomalies in sea-surface salinity between the ends of A2 and A2FA and the end of CTL. The freshening that takes place all around Greenland can be due to an increase in surface freshwater flux as well as to changes in oceanic circulation. The salinity reductions simulated along the northeastern and northwestern coasts appear related to the enhancement of the freshwater flux resulting from the melting of the Greenland ice sheet (not shown). In the GIN Seas, along the sea-ice edge, the freshwater flux diminishes in winter because of a decrease in sea-ice melting there and because of a shift of precipitation leading to a reduction in rainfall at that location. However, the sea-surface salinity decreases in this area in A2. If this salinity change cannot be explained by the modifications of the surface freshwater flux, it must be induced by an enhanced advection from less salty regions or a weakening of the sinking of freshwater to great depths. The northeastern salinity anomaly is indeed transported southwards by the East Greenland Current. Moreover, the convection weakens in this region compared to pre-industrial times, most probably because of the initial salinity decrease. The amount of freshwater that sinks is subsequently reduced. This reinforces the initial surface salinity decrease, thus tending to reduce deep convection. In A2FA, the sea-surface salinity in Denmark Strait increases in agreement with the surface freshwater flux decrease. This means that the compensating effects in this simulation are not as strong as in A2. The salinity anomaly further north is indeed much smaller than in A2. The convection at that place thus strengthens. In the GIN Seas and Baffin Bay, the

Greenland ice-sheet melting induces in A2 a significant freshening. Note that the difference in annual mean sea-surface salinity between A2 and A2FA exceeds 4 psu in Baffin Bay and Denmark Strait.

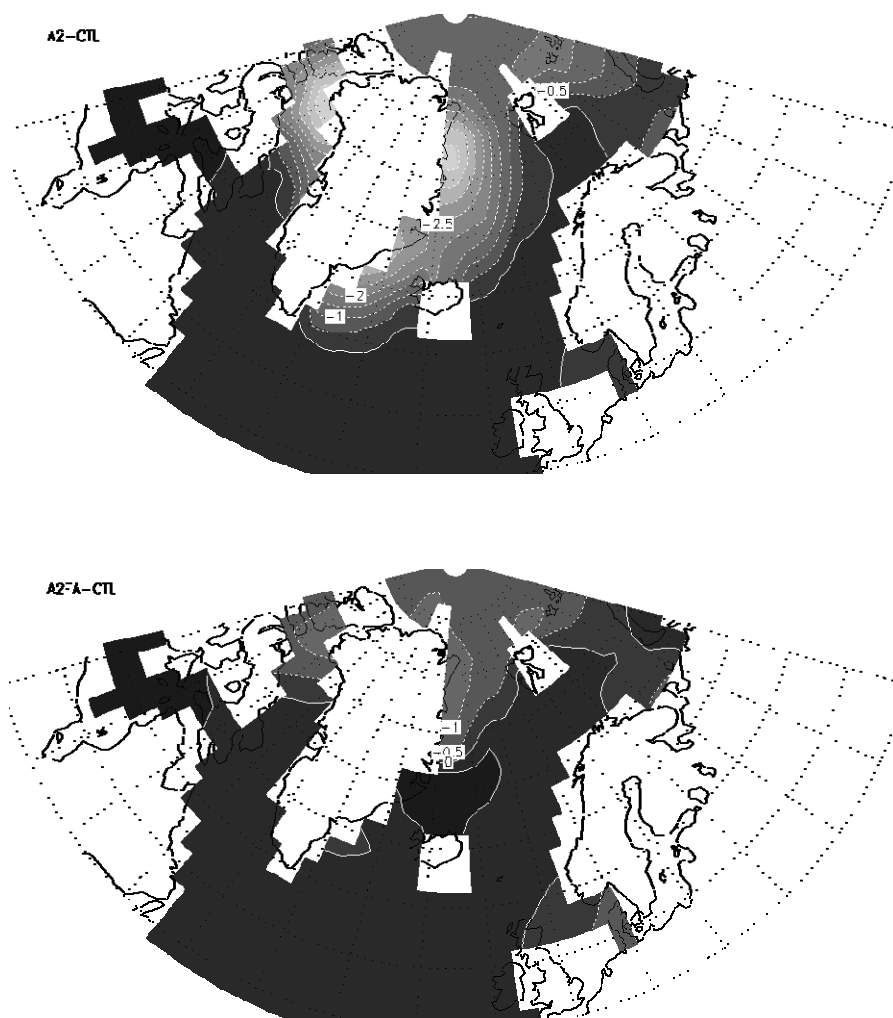


Figure 66: Changes in annual mean sea-surface salinity between years 2950–3000 AD of A2 and CTL (top) and between years 2950–3000 AD of A2FA and CTL (bottom). The contour interval is 0.5 psu.

Figures 67 display the convection depths during winter averaged over years 2950–3000 AD of A2 and averaged over the last 50 years of CTL. As previously mentioned, because of the initial salinity decrease occurring in A2, convection is completely stopped along the northeastern coast of Greenland. By contrast, in the Labrador Sea, convection is slightly deeper than in CTL.

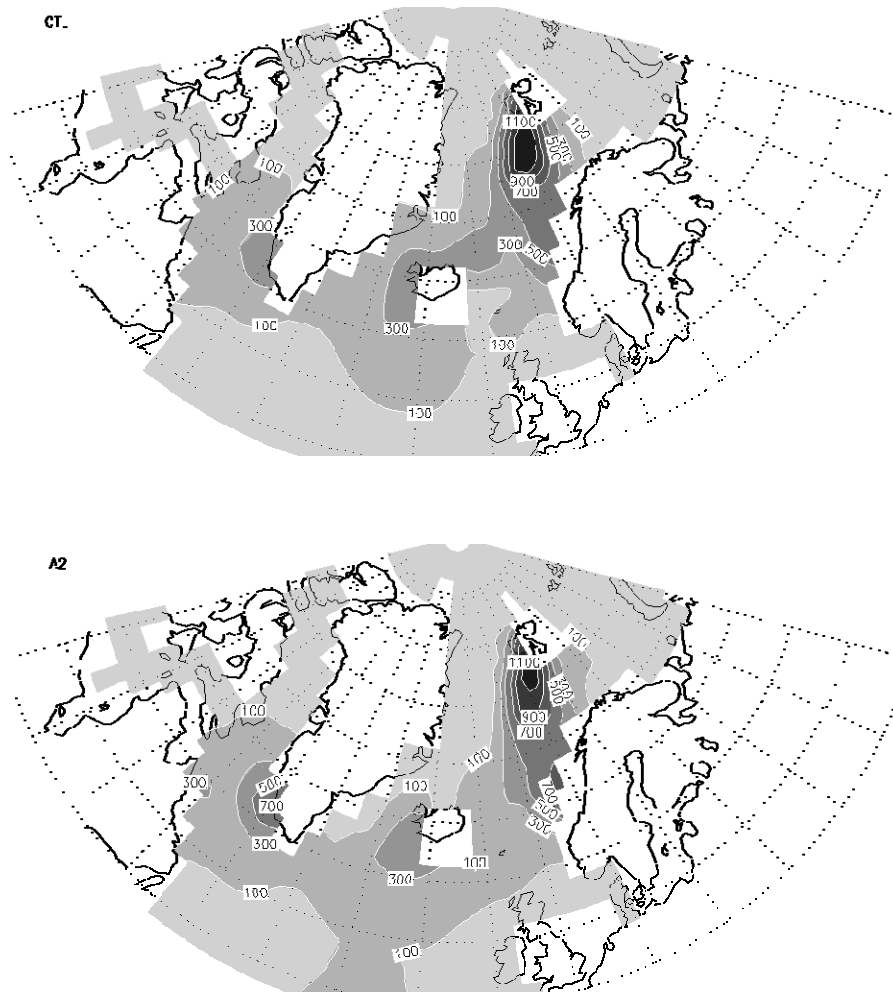


Figure 67 Convection depths in March averaged over the last 50 years of CTL (top) and over years 2950–3000 AD of A2 (bottom). The contour interval is 200 m.

At the end of simulation A2FA, in which the Greenland ice-sheet characteristics were not allowed to vary, the convection area extends eastwards in the GIN Seas owing to an increase in sea-surface salinity there. In this experiment, sea-ice melting during wintertime is reduced in the GIN Seas because of a retreat of the ice edge. In A2NA, the convection area extends even further north than in A2FA. During the period 2950–3000 AD, the freshwater forcing is indeed weaker along the northeastern coast of Greenland in A2NA than in A2FA. During the same period, in both A2FA and A2NA, the convective activity in the Labrador Sea is weaker than in CTL, despite an increase in sea-surface salinity in this area. This feature is caused by the warming of surface waters resulting from the prescribed radiative perturbation. In A2, the balance between the changes in sea-surface salinity and temperature is quite different, thus leading to a deepened convection.

MOC

The changes in convection patterns inevitably impact on the Atlantic MOC. As the convective activity is enhanced in the northern North Atlantic in A2FA and A2NA, the NADW cell is stretched northwards in these experiments. Around year 2975 AD of A2, the maximum value of the annual meridional overturning streamfunction below the surface layer between 45° and 75° N in the Atlantic basin is lower than in CTL (Figure 68). Also, the export of NADW at 30° S in the Atlantic, which is another index of the MOC strength, is weaker at that time (Figure 69).

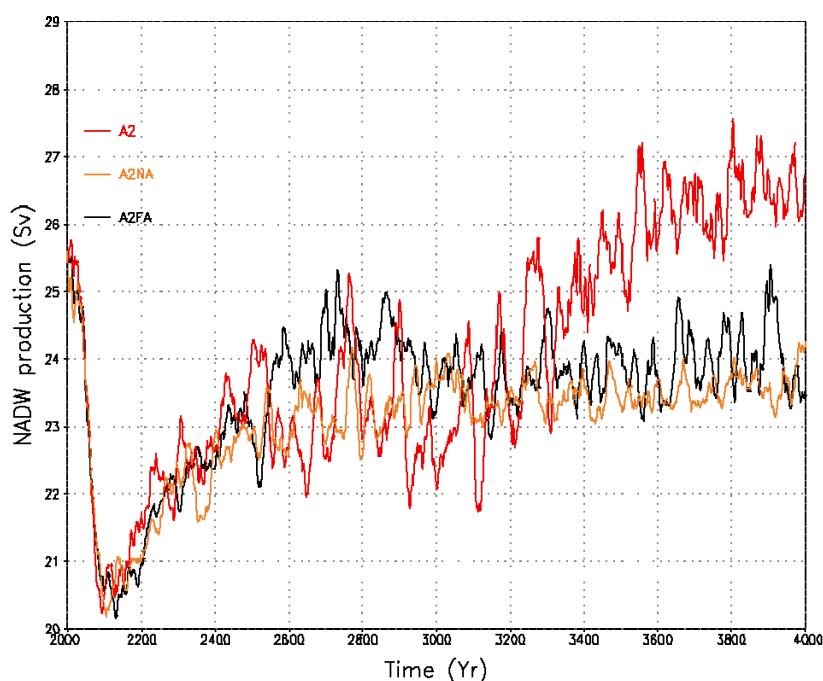


Figure 68: Time series of the maximum value of the annual mean meridional overturning streamfunction below the surface layer between 45° and 75° N in the Atlantic basin from A2 (red), A2NA (orange) and A2FA (black). A 21-yr running average has been applied to all time series.

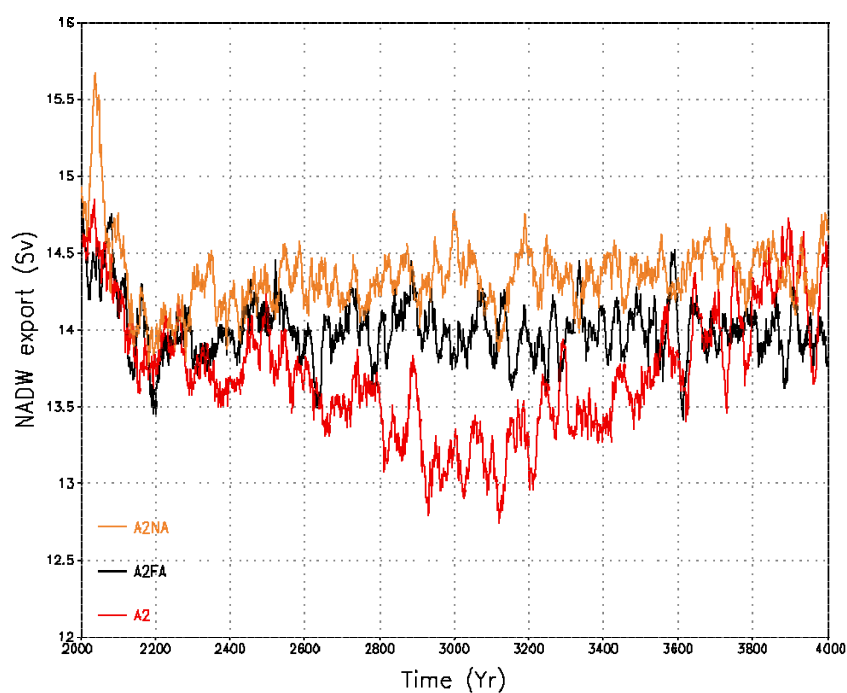


Figure 69: Time series of the export of NADW at 30° S in the Atlantic basin from A2 (red), A2NA (orange) and A2FA (black). A 21-yr running average has been applied to all time series.

If the ice sheets are fixed to their modern state, as in A2FA, or if AGISM is switched off, as in A2NA, the NADW production also exhibits a decrease during the first centuries of integration, as illustrated in Figure 68. In both sensitivity experiments, the export of NADW towards the Southern Ocean only experiences a slight weakening, which is somewhat smaller than in A2 (see Figure 69). The difference of behaviour regarding the NADW cell in the various simulations is very likely related to the Greenland freshwater flux and its influence on salinity.

Compared to CTL, the annual mean meridional oceanic heat transport (OHT) at 35° N in the Atlantic basin averaged over years 2950–3000 AD is reduced by 0.05 PW in A2FA and by 0.05 PW in A2 (Table 6). At 72° N, the OHT is larger in the sensitivity experiments than in CTL and A2. In A2NA, this feature is mostly caused by the northward expansion of the deep-convection area in the GIN Seas and by an associated increase in northward mass transport. This increase of heat input towards the area located north of 72°N is compensated by an increase of surface heat loss in A2FA and A2NA in the GIN Seas surface during winter. This represents a heat gain for the atmosphere that could explain the relatively large winter warming in A2NA and A2FA compared to A2 in this region. The retreat of the sea-ice edge is therefore responsible for the enhanced heat input north of 72°N. By contrast, in year 2975 AD of A2, the salinity anomaly keeps deep convection to the south until Denmark Strait. The OHT at 72°N is therefore reduced with respect to CTL.

	35° N	72° N
CTL	0.80 PW	0.15 PW
A2	0.68 PW	0.13 PW
A2FA	0.75 PW	0.17 PW
A2NA	0.77 PW	0.20 PW

Table 6: Annual mean meridional oceanic heat transport at 35° and 72° N in the Atlantic basin averaged over years 2950–3000 of CTL, A2, A2NA and A2FA.

At the end of A2, the anomaly in sea-surface salinity is weakened, and deep convection occurs further north. As a consequence, the OHT enhances slightly, and the ice edge is found further north than in 2975–3000 AD. Also, the NADW cell becomes more intense. The production of NADW is even larger at the end of A2 than at the ends of A2FA and A2NA, most probably because the salinity of the North Atlantic is higher in A2 than in the other two simulations.

Table 7 gives the contributions of the NADW temperature and cell intensity to the OHT at 72°N according to the following approximation:

$$OHT = \rho C_{p0} \Delta T \varphi_{max} ,$$

where ρ is the reference density of seawater, C_{p0} is the specific heat of seawater, φ_{max} is the maximum value of the annual mean meridional overturning streamfunction at that latitude and ΔT is the temperature difference between the upper and lower branches of the cell weighted by the mass transport. This approximation shows its limit when the changes are small. Thus, the results have to be interpreted carefully.

During years 2950–3000 AD of A2, the temperature and velocity contributions partly compensate each other in the above equation. The mass transport is indeed reduced by 2 Sv at 72° N compared to CTL, but the water in the upper branch is warmer than in CTL. Hence, the slight decrease shown in Table 6 likely results from the decline of the NADW cell. In both sensitivity experiments, the increase in OHT during 2950–3000 AD is underestimated by the approximation. The strengthening of the NADW cell is responsible for this increase when AGISM is switched off (A2NA). This is in line with the northward shift of the deep-convection area. In A2FA, it seems that the deep convection is not shifted far enough to have a substantial effect on OHT at 72°N since φ_{max} is 0.5 Sv higher than in CTL. Instead, the warming of the water flowing northwards is the leading contribution responsible for the OHT increase of 0.03 PW compared to CTL (see Table 6).

	CTL	A2	A2FA	A2NA
OHT	0.12 PW	0.12 PW	0.15 PW	0.17 PW
ΔT	2.8°C	3.7°C	3.5°C	3.2°C
φ_{max}	10.3 Sv	8.2 Sv	10.8 Sv	13.2 Sv

Table 7: Contributions to the annual mean meridional oceanic heat transport at 72°N in the Atlantic basin averaged over years 2950–3000 of CTL, A2, A2NA and A2FA. See text for details.

Cryosphere

The behaviour of the winter sea-ice edge is a consequence of a feedback loop. The northward retreat of the ice edge in A2FA and A2NA as a result of global warming induces higher salinities in the GIN Seas along the ice margin (those seas are areas where sea ice is advected and melts in CTL). This in turn leads to the shift of the deep-convection region discussed previously, which further intensifies the sea-ice melting. In A2, the large freshwater input from the Greenland ice sheet prevents convection to deepen as in the sensitivity experiments. As a consequence, in years 2950–3000 AD, the winter ice edge is located farther south (Figure 70). This is in agreement with the changes in Arctic heat input (see Table 6). In years 3975–4000 AD, the convection being stronger farther north in the GIN Seas, the sea-ice edge retreats northwards to reach almost the same position as in A2FA and A2NA. In Baffin Bay and Hudson Bay, the ice concentration is smaller at the end of simulation A2 than in A2NA and A2FA mostly because of the enhanced warming. In all, the Northern Hemisphere effective sea-ice area in wintertime is smaller in A2 than in A2NA and A2FA at the end of the simulations.

In summer, the feedback mechanisms occurring over Greenland in A2 lead to a larger warming in the whole Arctic region than in the other simulations. In June, for instance, during the period 3950–4000 AD, the warming in central Greenland is higher in A2 than in A2FA by 27°C. This warming is transported towards the Arctic Ocean by the atmosphere, enhancing the sea-ice melting. This melting is strongly reduced if the feedbacks in Greenland are switched off. The main difference is that a very large portion of the Arctic Ocean is free of summer sea ice at the end of A2, but not at the ends of A2NA and A2FA (see Figure 70).

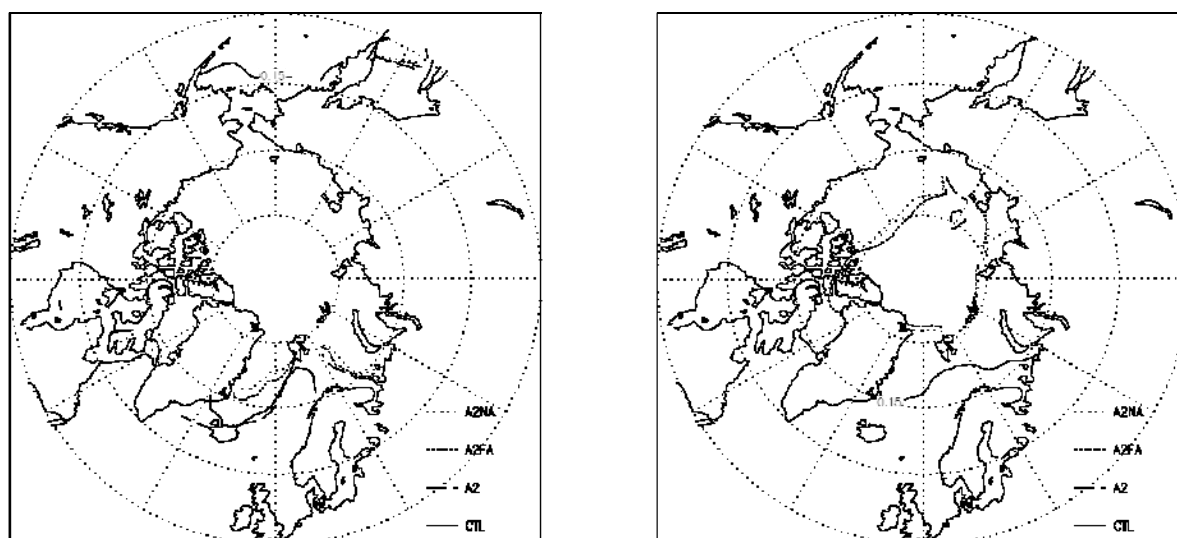


Figure 70: Positions of the Arctic sea-ice edge during March (left) and September (right) after 1000 years in CTL, A2FA, A2NA and A2. The sea-ice edge is defined as the 15% ice concentration contour.

In A2, after two millennia of integration, the Greenland ice sheet is almost melted away, while in A2FA, the ice volume is reduced by only one third and seems to stabilize. This underlines how important it is to take into consideration the two-way interactions between the Greenland ice sheet and climate in long-term projections of sea-level changes. In contrast, Ridley et al. (2005) found an increase in the rate of decline of the ice sheet when climate feedbacks were not included. They attributed this behaviour to a negative feedback in their model involving changes in the local atmospheric circulation during summer. Such a feedback is absent from our simulations, possibly because of the coarse resolution of ECBilt.

5.3.2. Carbon cycle

Carbon exchanges between reservoirs and climate change

In this section devoted to the carbon cycle, we analyze two sets of experiments. First, we examine the effect of changes in the radiative forcing in simulations using smooth stabilization profiles for the atmospheric CO₂ concentration. Note also that these experiments will serve later on to derive the anthropogenic emissions that would lead to such atmospheric CO₂-stabilization pathways. Then, we investigate the system response to anthropogenic emission scenarios in simulations with prognostic atmospheric CO₂.

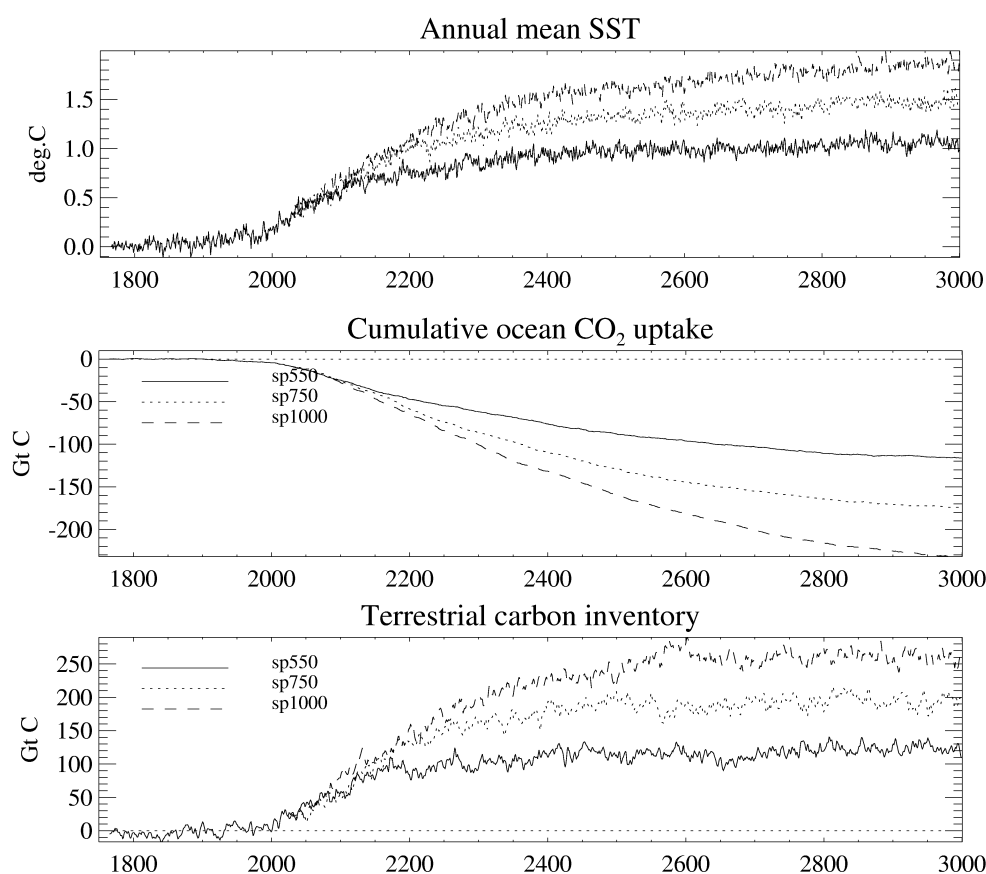


Figure 71: Differences in globally averaged, annual mean sea-surface temperature (top), cumulative oceanic carbon uptake (middle) and terrestrial carbon inventory (bottom) between experiments with radiative forcing and without it for smooth CO₂-stabilization profiles.

Smooth CO₂-stabilization profiles

In the first series of simulations, the atmospheric CO₂ concentration was constrained to follow the three scenarios sp550, sp750 and sp1000 (see Figure 39). For each scenario, we performed two experiments: one with no radiative forcing change and another one in which the radiative forcing evolved following the CO₂ partial pressure. The setup for these runs is described in Section 5.1. It is worth mentioning that, as CO₂ affects the growth of plants, a constant radiative forcing is not equivalent to fixed climate conditions. However, such experiments allow obtaining an estimate of the impact of climate change on the global carbon cycle.

Figure 71 illustrates the differences between the simulations with climate change and those with a constant radiative forcing. In Table 8, we give the changes in the carbon inventories on land and in the ocean over the period 1860–3000 AD. In the runs with climate change, the carbon uptake over land is roughly half of the carbon

uptake by the ocean. With no radiative forcing change, the terrestrial uptake represents at most one third of the oceanic uptake. The impact of climate change on the carbon uptakes by the ocean and the terrestrial biosphere is of similar magnitude but of opposite sign (see also Table 9). The uptake by the terrestrial biosphere is enhanced due to both the CO₂ increase and the warming climate. By contrast, the higher sea-surface temperatures lead to larger sea-surface CO₂ partial pressures, which results in a decrease of the oceanic uptake under climate change.

Exp.	sp550	sp550CR	sp750	sp750CR	sp1000	sp1000CR
Ocean	1351	1467	1820	1994	2189	2421
Land	543	434	833	634	1092	833

Table 8: Carbon uptakes by the ocean and the terrestrial biosphere in the sp experiments. The numbers represent the cumulative uptakes (in GtC) from 1860 to 3000 AD. The results from experiments with radiative forcing changes are presented in columns 2, 4 and 6. Experiments with constant radiative forcing correspond to columns 3, 5 and 7.

Experiment			sp550	sp750	sp1000
Ocean	Climate effect	GtC	-116	-174	-232
		%	-7.9	-8.7	-9.6
Land	Climate effect	GtC	+109	+199	+259
		%	25.1	31.4	31.1
	"CO ₂ " effect	%	74.9	68.6	68.9

Table 9: Differences in carbon uptakes by the ocean and the terrestrial biosphere between the sp experiments with and without radiative forcing change. Absolute differences are given in lines 2 and 4, and relative differences in lines 3 and 5. The CO₂-fertilization effect on the terrestrial biosphere is given in the last line.

We further evaluate the influence of climate change by computing the following ratio (Table 9):

$$(U - U_{CR})/U_{CR}$$

where U denotes the uptake under climate change and U_{CR} the uptake when no radiative change occurs. While the absolute differences ($U - U_{CR}$) for the ocean and the land have a similar magnitude, the relative changes are much larger for the continental biosphere. The climate impact on the oceanic uptake represents at most -10% . In the same time, the terrestrial uptake increases by up to 30% . The CO_2 -fertilization effect contributes for about 70% to the total uptake.

Emission-commitment scenarios

The anthropogenic CO_2 emissions in the selected emission commitment scenarios increase up to the end of the 21st century and then abruptly stop (see Figure 40). In response to this forcing the atmospheric CO_2 increases steadily up to year 2100 AD and then begins to decrease first rapidly and then more slowly (Figure 72).

Exp.	SP550EC	SP750EC	SP1000EC
Ocean	858	1010	1047
Land	303	356	371

Table 10: Carbon uptakes by the ocean and the terrestrial biosphere in the emission-commitment experiments. The numbers represent the cumulative uptakes (in GtC) from 1860 to 3000 AD.

As discussed in Section 4, the continental biosphere is a strong CO_2 sink during the 21st century in LOVECLIM, which compensates for the decrease in oceanic uptake resulting from the increasing sea-surface temperatures. At longer-term, however, the role of the continental biosphere in setting the atmospheric CO_2 becomes less and less important. For instance, in year 3000 AD, the cumulative carbon uptake by the continents represents only $\sim 30\%$ of that of the ocean (Table 10).

Once CO_2 emissions stop, the atmospheric CO_2 concentration decreases very rapidly owing to the combined effects of the ocean and the terrestrial biosphere. The latter constitutes a carbon sink for one more century after emissions stop. At the beginning, the oceanic sink is entirely determined by the large partial pressure difference across the sea surface. On longer time-scales, the oceanic uptake is governed by the replacement rate of surface waters by old under-saturated waters. Given that the turnover time of the World Ocean is approximately 1000 years, the atmospheric CO_2 will only reach its stabilization level after several centuries. In

addition, the continents become a source after the 22nd century (see Figure 72) as a consequence of the decrease in fertilization resulting from the drop in atmospheric CO₂. This process also prevents a rapid decrease in atmospheric CO₂ concentration.

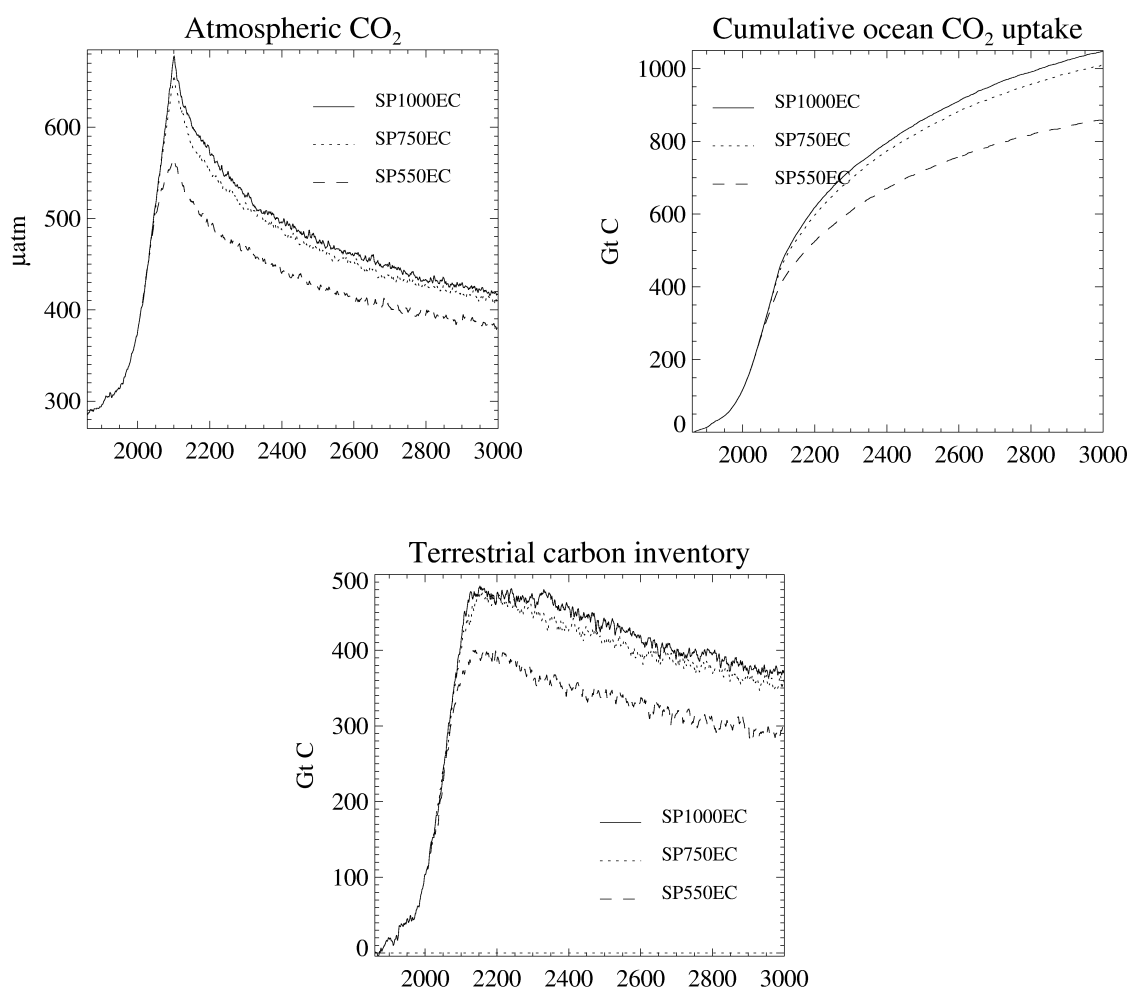


Figure 72: Results from the three emission-commitment experiments. Temporal evolution of atmospheric CO₂ concentration (top, left), cumulative oceanic carbon uptake (top, right) and terrestrial carbon inventory (bottom). Inventories are relative to year 1860 AD.

Biogeochemical cycles and climate change

Models of the ocean biogeochemistry usually includes simple parameterisations of fluxes (e.g., Sarmiento et al., 1998) or basic biological modules (e.g., Six and Maier-Reimer, 1996; Bopp et al., 2001). The model used in this study is not better than those models. Among the shortcomings of all these models, we may put forward the lack of mechanistic representation of the fate of the organic matter leaving the

upper oceanic layers, the reduced number of plankton species considered, the neglect of the acidification effect on calcareous shell building organisms, ... As a consequence, the results from any study dealing with the impact of future climate change on the ocean biological cycles should be taken with utmost care. There are mainly two reasons for using such simplified tools. First, a sophisticated representation of biogeochemical cycles would be extremely demanding in computer resources and would jeopardize the possibility to perform century-long runs. Second, most processes simply have to rely on crude parameterisation due to a lack of deep understanding of their functioning. However, these elementary tools may help in evidencing possible processes or important pathways that need more investigation.

We have conducted several experiments with LOVECLIM in which the biological module of LOCH was activated. The initial state corresponded to results from a pre-industrial control run which span several millennia, the time needed for the oceanic carbon reservoir to reach a quasi-steady state. The atmospheric CO₂ concentration was then forced to follow the reconstructed atmospheric signal from 1750 to 2000 AD, at which stage we applied the two concentration scenarios SRES B1 and SRES A2 and let the simulation run until year 2300 AD. Those experiments were carried out with both the on-line and off-line versions of LOCH. In the off-line case, LOCH was driven by output fields from CLIO. These fields were obtained by averaging the hydrodynamic and climate seasonal fields over the last 20 years of the pre-industrial control run. Each experiment (on-line or off-line) was accompanied by a control run, i.e. an experiment with no climate nor CO₂ change, in order to ensure that no model drift would bias the results.

The model does not predict any major change in the biologically mediated ocean carbon fluxes over the next centuries under climate change (experiments C_B A2 and C_B B1). At the end of the model integration, there is a slight increase of the order of 3% in global export production (+0.2 GtC over 6.5 GtC) under scenario A2 (Figure 73). This contrasts with other modelling studies, which suggest a significant decrease in the export production under climate change: -7% in Maier-Reimer et al. (1996), -15% in Matear and Hirst (1999), -6% in Bopp et al. (2001) and up to -25% in Bopp et al. (2005). It should be noted that, in these studies, significant changes occur in the oceanic circulation: enhanced stratification, large increase in sea-surface temperature, much reduced NADW transport, ..., all changes that we do not observe

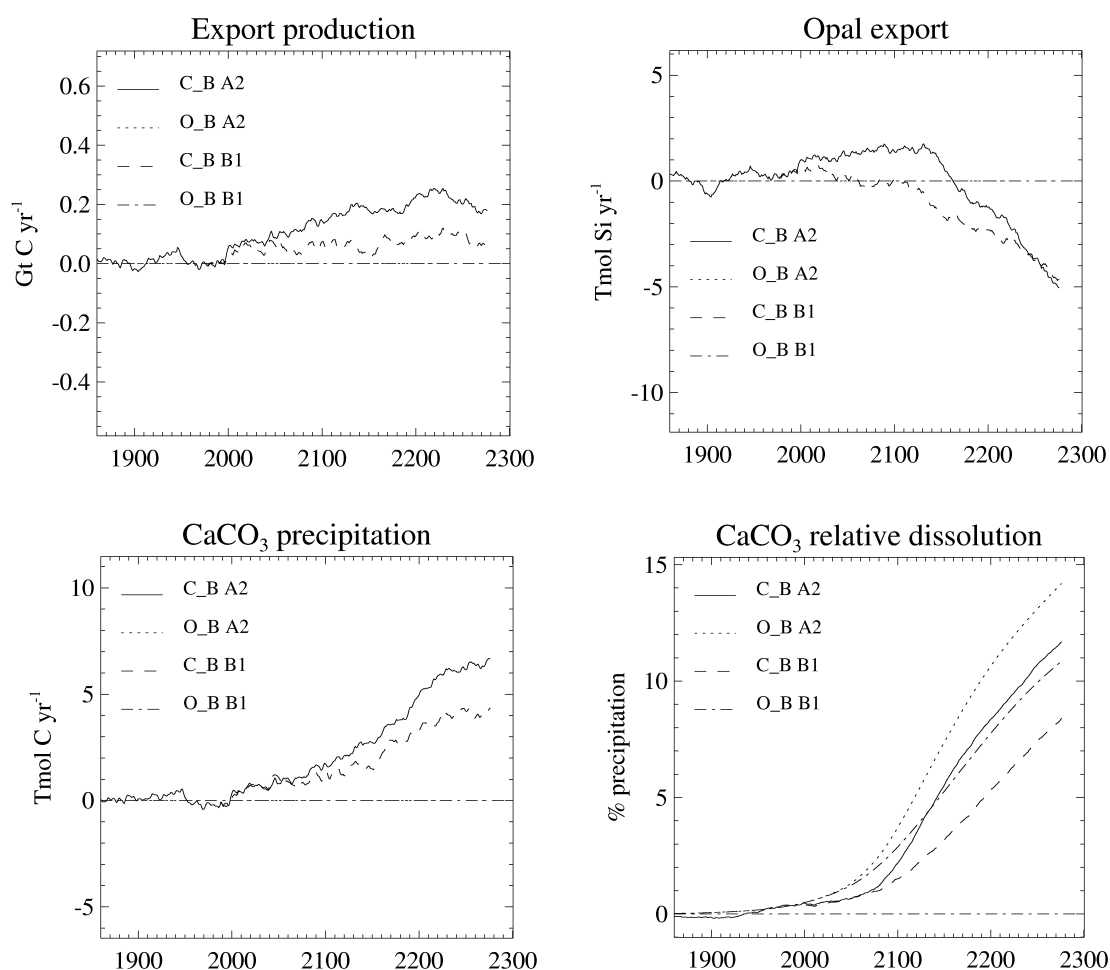


Figure 73: Changes over the centuries in the export production (top, left), the opal export (top, right), the CaCO₃ shell building (bottom, left) and the CaCO₃ dissolution relative to precipitation (bottom, right). These changes were obtained under the two SRES scenarios B1 and A2 for atmospheric CO₂ and represent anomalies with respect to the corresponding control run. Experiments labelled C_B refer to the on-line version of the carbon-cycle model, while those whose name starts with O_B were run with the off-line version.

in the present model. This might explain the large discrepancy between our results and those from these other studies. Some explanation might also be found in the model design. Among these other studies, only Bopp et al. (2005) considered more than one phytoplankton species (actually, their model included diatoms and nano-phytoplankton). Hence, in their model, enhanced stratification in the Southern Ocean resulted in a significant shift from diatoms to nano-phytoplankton, which contributes less to the export of carbon from the surface ocean. Our model allows other species to replace diatoms, but the distribution profile of dead organic matter with depth does not reflect the species distribution in the euphotic zone (the possibility of adapting the vertical profile of organic matter remineralization to the ecosystem composition exists in the model, but was not activated in these experiments). An ecosystem shift

consecutive to significant changes in the surface ocean constitutes a potentially positive feedback.

Similarly to the other studies, our model predicts a shift of the biological activity towards higher latitudes because the sea-ice retreat leads to a longer growing season there. Indeed, at high latitudes, productivity is principally limited by the lack of sunlight. Sea ice, when present, reflects a large part of the incoming shortwave radiation. The drastic reduction in ice-covered area discussed previously results in an enhanced primary productivity. This increase of export production more than compensate for the slight decrease observed at low latitudes (Figure 74) in our model, in contrast with the results from the abovementioned studies.

This increase in biological activity is accompanied by a significant decrease in silicate content in the euphotic layer at high latitudes (see Figure 74). Silicate concentrations in the Southern Ocean drop by as much as 30% in 2300 AD under the SRES scenario A2 when compared to the control run. This decrease in surface silica concentration comes from an enhanced utilization of silica at high latitudes consecutive to the increase in biological activity. Opal dissolution occurs at much deeper levels than nutrient remineralization, and is thus less readily available in the surface layers. Therefore, less and less of primary production is supported by opal-shell building organisms, which translates into a significant decrease in the export of opal from the euphotic layer (see Figure 73). In the model, this produces a shift towards other forms of primary producers and yields a quite significant increase in global CaCO_3 precipitation (see Figure 73). Despite the fact that low temperatures limit the growth of calcareous-shell building organisms in polar areas, the general increase in export production together with the depletion of silica in the euphotic layer result in a global increase in CaCO_3 biologically-mediated precipitation. This leads to a small positive feedback, as this process increases dissolved CO_2 . Yet, the model does not consider the effect of ocean acidification on calcareous organisms, hence the modelled effect may be considered as representing an upper bound for this feedback. CO_2 invasion into the deep ocean is responsible for an increase in CaCO_3 dissolution (see Figure 73). Under SRES scenario A2 with climate change (experiment C_B A2), the dissolution anomaly in 2300 AD compared to year 2000 AD reaches up to 12% of the CaCO_3 export. However, this negative feedback will not be effective before the deep waters, in which this dissolution anomaly takes place, come back to the surface – a delay of several centuries. The difference in relative dissolution rate between the on-line and off-line runs arises from a combination of processes. The rate of CaCO_3 -shell dissolution increases with acidification; the latter is larger in the off-line run which does not experience any sea-surface temperature change and which exhibits a larger oceanic uptake of atmospheric CO_2 . In addition, the increase and redistribution of CaCO_3 -shell builders consecutive to the change in

silica content of the upper layers in the C_B experiments result in a larger saturation at depth, which decreases dissolution rates.

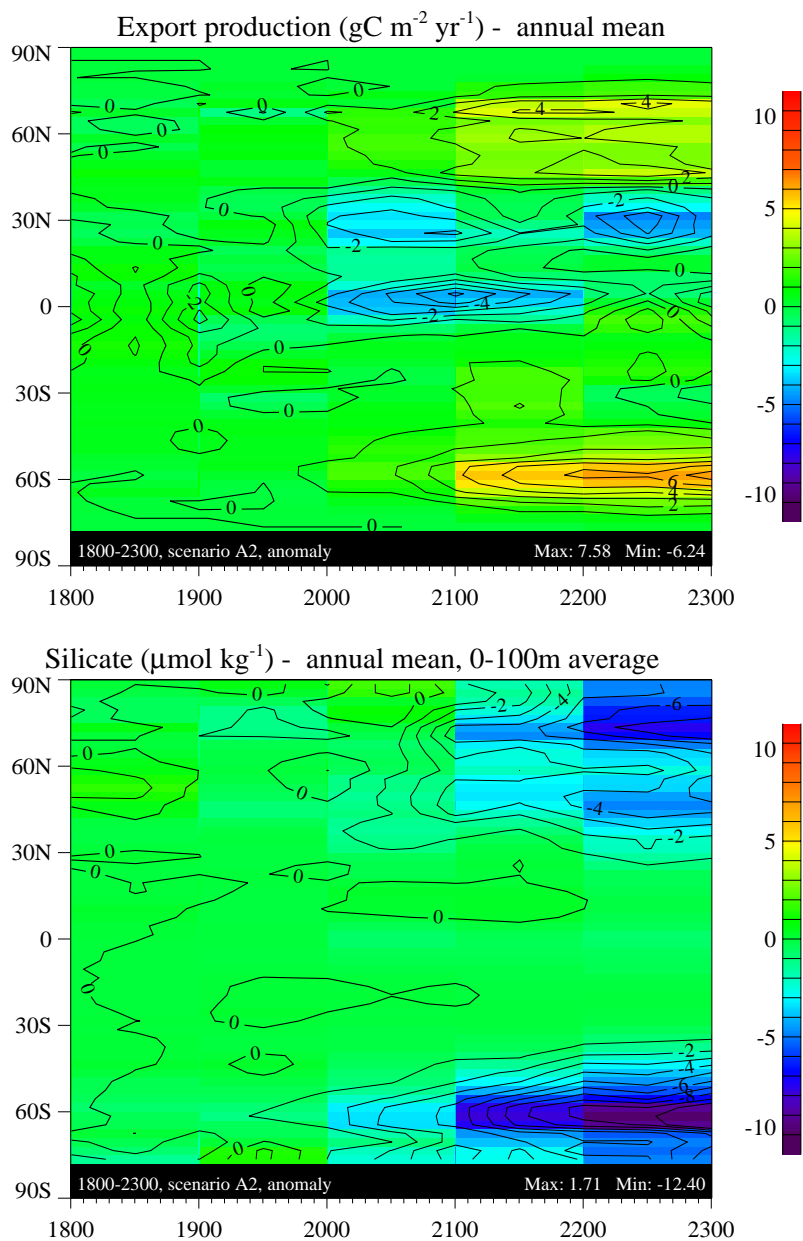


Figure 74: Temporal evolution of the anomalies in export production (top) and silica content of the upper 100 m (bottom) averaged over each latitudinal band for the experiment using the SRES scenario A2.

Anthropogenic emissions leading to given atmospheric CO₂ levels

From the experiments with prescribed atmospheric CO₂ concentrations, it is possible to derive the anthropogenic emissions that would result in a given atmospheric CO₂ level. Indeed, the balance between fluxes to or from the ocean and

continents and anthropogenic inputs determine the atmospheric CO₂ content. The change in atmospheric carbon content dA during a given time interval τ writes

$$dA = (E_A + F_O + F_C) \tau,$$

where E_A , F_O and F_C represent the anthropogenic emissions and the net carbon fluxes from the ocean and continental reservoirs, respectively. Knowing dA , F_O and F_C together with their temporal evolution, we may then obtain the evolution of E_A with time.

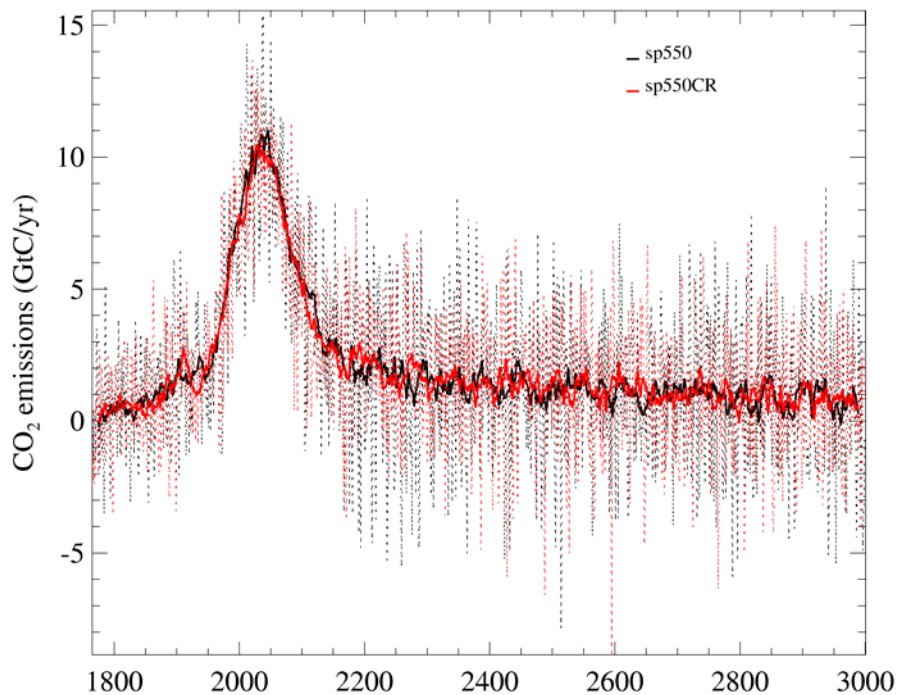


Figure 75: Temporal evolution of the emissions that would lead to the atmospheric CO₂ concentrations as given by scenario sp550. The black curve is for the case with climate change, the red one for the case without climate change. Dotted lines are used for the unfiltered data, while solid lines are obtained by applying a 20-yr running average.

The curves in Figures 75 and 76 represent the emissions that would lead to the evolutions of the atmospheric CO₂ concentration as prescribed by scenarios sp550 and sp1000. The cases with and without climate-change effect are plotted. For each scenario, the possible emissions are slightly larger when the warming effect is taken into account. However, this difference is hardly significant. Indeed, the cumulated emissions from 1765 to 3000 AD under scenario sp550 amount to 2491 GtC with warming and to 2493 GtC without it, respectively. Under scenario sp1000, these figures become 4832 GtC with warming and 4801 GtC without it. In both cases, the relative difference between the total emissions with or without warming represent less than 1% (–0.04% for sp550 and 0.6% for sp1000). Climate change produces a

decrease (increase) in the carbon uptake by the ocean (terrestrial biosphere). As mentioned previously, the strengthening of the terrestrial vegetation sink nearly compensates for the weakening of the oceanic carbon sink. This model behaviour explains why the reconstructed emissions curves are so close.

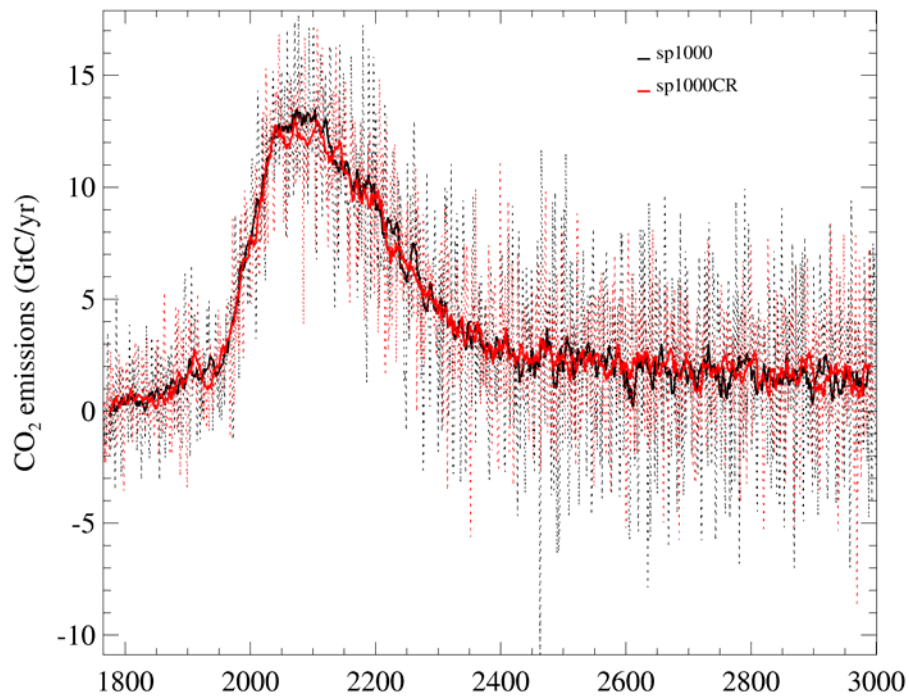


Figure 76: Same as Figure 75, but for scenario sp1000.

6. DISSEMINATION OF THE RESULTS

The results discussed above were presented in numerous scientific meetings and workshops, and led to about 70 international peer-reviewed publications (two common ones are still in preparation). Moreover, some of these results are part of the forthcoming IPCC AR4. Dissemination took also place via the training of young researchers. In particular, one PhD thesis directly related to MILMO was defended during the project.

The research network MILMO consisted of scientists deeply involved in the activities of the IPCC, the European Union’s Fifth and Sixth Framework Programmes, the World Climate Research Programme (WCRP), especially its core projects Climate and Cryosphere (CliC) and Climate Variability and Predictability (CLIVAR), the core projects Past Global Changes (PAGES) and Surface–Ocean–Lower Atmosphere Study (SOLAS) of the International Geosphere–Biosphere Programme (IGBP), and the core project Antarctic Climate Evolution (ACE) of the Scientific Committee on Antarctic Research (SCAR). In particular, one member was Lead Author of one chapter of the IPCC AR4 and two others were Contributing Authors of several chapters. This has enabled the dissemination of the MILMO results both to scientists involved in studying climate change and to the communities involved in impact studies.

MILMO-related results were also disseminated outside the scientific community via vulgarization conferences in universities, schools and societies, the printed press, and television and radio interviews. Parts of these results are included in the Belgian Global Change Research 1990–2002 Assessment and Integration Report published in June 2005 and intended, in particular, for policymakers. Besides those activities, an international workshop was organized at VUB on November 16–17, 2004 to inform the Belgian scientific community about our results. A specific web site was also created on the server of the coordinator and connected to PPS Science Policy’s information system. This site provided information about the objectives, the model and the progress of the project. Finally, we would like to stress here that most of the model outputs generated during the project are stored in a database and are available upon request.

7. CONCLUSIONS AND RECOMMENDATIONS

Most of the initial objectives of MILMO, that are recalled in Section 1 of the present report, have been reached. In particular, a new three-dimensional EMIC that includes representations of the polar ice sheets and of the carbon cycle has been developed and validated over the last few centuries. Furthermore, we showed with this model, named LOVECLIM, that, for a wide range of greenhouse-gas-stabilization profiles, it is very likely that the volume of the Greenland ice sheet will largely decrease in the future. In the most extreme case considered in our study, Greenland becomes ice-free in about 2000 years. Note that the ice-sheet disintegration might be even more rapid if processes responsible for the widespread glacier acceleration currently observed in Greenland (e.g., Rignot and Kanagaratnam, 2006) were taken into account in the model. We also found that the freshwater flux from the melting Greenland ice sheet into the neighbouring oceans, which peaks in the most extreme scenario tested at 0.11 Sv and remains above 0.1 Sv during three centuries, is not large enough to trigger a shutdown of the AMOC in our model. Some models are, however, more responsive to freshwater perturbations than ours (e.g., Rahmstorf et al., 2005; Stouffer et al., 2006). Besides, we showed that climate feedbacks play a crucial role in the ice-sheet evolution and that the Greenland deglaciation considerably enhances the greenhouse-gas-induced warming over Greenland and the central Arctic, thus leading to the quasi-disappearance of the summer Arctic sea-ice pack. This stresses the importance of incorporating the two-way interactions between the Greenland ice sheet and climate in climate- and sea-level-change projections at the millennial time-scale. For the Antarctic ice sheet, the response is much less drastic than for the Greenland ice sheet. For instance, after 3000 years of $4\times\text{CO}_2$ forcing, the Antarctic grounded ice volume and area are reduced in our model by only 8% and 4 %, respectively. Our results suggest that it will be very difficult to limit the eventual sea-level rise to less than 1 m after 1000 years, unless the atmospheric CO_2 concentration can be stabilized to less than twice its pre-industrial level. Such a goal can only be reached by emission reductions far larger than any policy currently pursued. Concerning the carbon cycle, the experiments carried out with LOVECLIM highlight the opposite responses of the terrestrial and oceanic carbon reservoirs to climate change. We also found that, when anthropogenic CO_2 emissions cease, the terrestrial biosphere becomes a weak carbon source, while the ocean continues to be a sink. It should be stressed that no dramatic change in the global marine productivity is observed in our simulations. This arises from the fact that the modifications of the oceanic properties that affect this productivity (stratification, meridional overturning, ...) are rather moderate. The effects of climate change are however not negligible. In particular, the decrease in sea-ice extent predicted by the model results in a longer growing season and a larger nutrient

uptake (especially silica) in polar regions. As a result, by the end of the 23rd century, silica concentrations in the upper 100 m of the Southern Ocean drop by as much of 30% for the most extreme forcing scenarios.

The work made within MILMO is a contribution to the ongoing international scientific effort to better understand and assess how human activities impact the climate system at the global scale. This is needed in order to provide a sound basis for policies designed to address the challenge of climate changes. The problem will not go away quickly, and is most likely to become more and more important. Each Party to the United Nations Framework Convention on Climate Change (UNFCCC) has committed itself to "promote and cooperate in scientific (...) research (...) related to the climate system and intended to further understand and reduce the remaining uncertainties (...)." (UNFCCC Article 4.1(g)).

The sustained funding of this kind of research is required both at the international and national levels, so that the appropriate scientific capacity is available in as many countries as possible. One area that requires a particular attention is the improvement of the representation of physical and biogeochemical processes in Earth system models in order to reduce uncertainties in projections. So that the Belgian research effort becomes better integrated in the European and international research programmes, the appropriate support should be given to facilitate participation in the existing and planned model-intercomparison programmes. These allow the different modelling laboratories to confront their methods and results to each other, so that the origin of differences can be better understood. This will lead to better models, enhance capacity building and help in integrating the Belgian research efforts. For the same reasons, participation of Belgian modellers to interdisciplinary research dealing with the impacts and mitigation of climate change is of high value, and collaboration to the work of the IPCC should be encouraged.

REFERENCES

- Bahr, D. B., Meier, M. F. and Peckham, S. D. 1997. The physical basis of glacier volume-area scaling. *Journal of Geophysical Research*, 102, 20,355-20,362.
- Bamber, J. L., Layberry, R. L. and Gogineni, S. P. 2001. A new ice thickness and bed dataset for the Greenland ice sheet. 1. Measurement, data reduction, and errors. *Journal of Geophysical Research*, 106, 33,773-33,780.
- Bard, E., Raisbeck, G., Yiou, P. and Jouzel, J. 2000. Solar irradiance during the last 1200 years based on cosmogenic nuclides. *Tellus*, 52 , 985-992.
- Beckmann, A. and Goosse, H. 2003. A parameterization of ice shelf–ocean interactions for climate models. *Ocean Modelling*, 5 , 157-170.
- Bernsten, T., Wyhre, G., Stordal, F. and Isaksen, F. 2000. Time evolution of tropospheric ozone and its radiative forcing. *Journal of Geophysical Research*, 105, 8915-8930.
- Bond, G., Broecker, W., Johnsen, S., McManus, J., Labeyrie, L., Jouzel, J. and Bonani, G. 1993. Correlations between climate records from North Atlantic sediments and Greenland ice. *Nature*, 365, 143-147.
- Bopp, L., Monfray, P., Aumont, O., Dufresne, J.-L., Le Treut, H., Madec, G., Terray, L. and Orr, J. C. 2001. Potential impact of climate change on marine export production. *Global Biogeochemical Cycles*, 15, 81-100.
- Bopp, L., Aumont, O., Cadule, P., Alvain, S. and Gehlen, M. 2005. Response of diatoms distribution to global warming and potential implications: A global model study. *Geophysical Research Letters*, 32, L19606, DOI: 10.1029/2005GL023653.
- Boucher, O. and Pham, M. 2002. History of sulfate aerosol radiative forcings. *Geophysical Research Letters*, 29 , 1308-1311.
- Braithwaite, R. J., Zhang, Y. and Raper, S. C. B. 2002. Temperature sensitivity of the mass balance of mountain glaciers and ice caps as a climatological characteristic. *Zeitschrift für Gletscherkunde und Glazialgeologie*, 38, 35-61.
- Brovkin, V., Bendsten, J., Claussen, M., Ganopolski, A., Kubatzki, C., Petoukhov, V and Andreev, A. 2002. Carbon cycle, vegetation and climate dynamics in the Holocene: Experiments with the CLIMBER-2 model. *Global Biogeochemical Cycles*, 16, DOI: 10.1029/2001GB001662.
- Brovkin, V., Claussen, M., Driesschaert, E., Fichet, T., Kicklighter, D., Loutre, M.-F., Matthews, H., Ramankutty, N., Schaeffer, M. and Sokolov, A. 2006. Biogeophysical effects of historical land cover changes simulated by six Earth

- system models of intermediate complexity. *Climate Dynamics*, 26, 587-600, DOI: 10.1007/s00382-005-0092-6.
- Campin, J.-M. and Goosse, H. 1999. A parameterization of density-driven downsloping flow for a coarse resolution model in z-coordinate. *Tellus*, 51, 421-430.
- Charlson, R. J., Langner, J., Rodhe, H., Leovy, C. B. and Warren, S. G. 1991. Perturbation of the Northern Hemisphere radiative balance by backscattering from anthropogenic sulfate aerosols. *Tellus*, 43, 152-163.
- Chou, C. and Neelin, J. 1996. Linearization of a long-wave radiation scheme for intermediate tropical atmospheric models. *Journal of Geophysical Research*, 101, 15,129-15,145.
- Church, J. A., Gregory, J. M., Huybrechts, P., Kuhn, M., Lambeck, K., Nhuan, M. T., Qin, D. and Woodworth, P. L. 2001. Changes in sea level. In: *Climate Change 2001: The Scientific Basis. Contribution of Working Group I to the Third Assessment Report of the Intergovernmental Panel on Climate Change*. Houghton, J. T., Ding, Y., Griggs, D. J., Noguer, M., van der Linden, P. J., Dai, X., Maskell, K. and Johnson, C. A. (Eds.), Intergovernmental Panel on Climate Change, Cambridge Univ. Press, Cambridge, United Kingdom and New York, U.S.A., pp. 639-694.
- Claussen, M., Kubatzki, C., Brovkin, V., Ganopolski, A., Hoelzmann, P. and Pachur, H.-J. 1999. Simulation of an abrupt change in Saharan vegetation in the mid-Holocene. *Geophysical Research Letters*, 26, 2037-2040.
- Cox, P. M., Betts, R. A., Jones, C. D., Spall, S. A. and Totterdell, I. J. 2000. Acceleration of global warming due to carbon-cycle feedbacks in a coupled climate model. *Nature*, 408, 184-187.
- Cramer, W., Bondeau, A., Woodward, F.I., Prentice, I., Betts, R., Brovkin, V., Cox, P., Fisher, V., Loley, J., Friend, A., Kucharik, C., Lomas, M., Ramankutty, N., Stitch, S., Smith, B., White, A. and Young-Molling, C. 2001. Global response of terrestrial ecosystem structure and function to and climate change: Results from six dynamic global vegetation model. *Global Change Biology*, 7, 357-373.
- Crowley, T. J. 2000. Causes of climate change over the past 1000 years. *Science*, 289, 270-277.
- Deleersnijder, E. and Campin, J.-M. 1995. On the computation of the barotropic mode of a free-surface World Ocean model. *Annales Geophysicae*, 13, 675-688.
- deMenocal, P. B., Ortiz, J., Guilderson, T., Adkins, J., Sarnthein, M., Baker, L. and Yarusinski, M. 2000. Abrupt onset and termination of the African humid period:

- Rapid climate response to gradual insolation forcing. *Quaternary Science Reviews*, 19, 347-361.
- de Wolde, J., Huybrechts, P., Oerlemans, J. and van de Wal, R. S. W. 1997. Projections of global mean sea level rise calculated with a 2D energy-balance climate model and dynamic ice sheet models. *Tellus*, 49A, 486-502.
- Dickson, A. G. 1981. An exact definition of total alkalinity and a procedure for the estimation of alkalinity and total inorganic carbon from titration data. *Deep-Sea Research*, 28A, 609-623.
- Dickson, A. G., and Goyet, C. 1996. Handbook of Methods for the Analysis of the Various Parameters of the Carbon Dioxide System in Sea Water. Version 2. ORNL/CDIAC-74, United States Department of Energy, Washington, D. C., USA.
- Dixon, K. and Lanzante, J. 1999. Global mean surface air temperature and North Atlantic overturning in a suite of coupled GCM climate change experiments. *Geophysical Research Letters*, 26, 1885-1888.
- Driesschaert, E. 2005. Climate change over the next millennia using LOVECLIM, a new Earth system model including the polar ice sheets. PhD. thesis, Univ. catholique de Louvain, Louvain-la-Neuve, Belgium, 214 pp.
- Dufresne, J.-L., Friedlingstein, P., Berthelot, M., Bopp, L., Ciais, P., Fairhead, L., Le Treut, H. and Monfray, P. 2002. On the magnitude of positive feedback between future climate change and the carbon cycle. *Geophysical Research Letters*, 29, DOI: 10.1029/2001GL013777.
- Duplessy, J.-C., Shackleton, N. J., Fairbanks, R. G., Labeyrie, J., Oppo, D. and Kallel, N. 1988. Deepwater source variations during the last climatic cycle and their impact on the global deepwater circulation. *Paleoceanography*, 3, 343-360.
- Fichefet, T. and Morales Maqueda, M. A. 1997. Sensitivity of a global sea ice model to the treatment of ice thermodynamics and dynamics. *Journal of Geophysical Research*, 102, 12,609-12,646.
- Fichefet, T. and Tricot, C. 1992. Influence of the starting date of model integration on projection of greenhouse-gas-induced climatic change. *Geophysical Research Letters*, 19, 1771-1774
- Flato, G. M. and Participating CMIP Modelling Groups. 2004. Sea-ice and its response to forcing as simulated by global climate models. *Climate Dynamics*, 23, 229-241, DOI: 10.1007/s00382-004-0436-7.
- Foley, A., Kutzbach, J., Coe, M. T. and Levis, S. 1994. Feedbacks between forests during the Holocene epoch. *Nature*, 371, 52-54.

- Gent, P. R. and McWilliams, J. C. 1990. Isopycnal mixing in ocean general circulation models. *Journal of Physical Oceanography*, 20 , 150-155.
- Gerdes, R., Determann, J. and Grosfeld, K. 1999. Ocean circulation beneath Filchner-Ronne Ice Shelf from three-dimensional model results. *Journal of Geophysical Research*, 104, 15,827-15,842.
- Goosse, H. and Fichefet, T. 1999. Importance of ice-ocean interactions for the global ocean circulation: A model study. *Journal of Geophysical Research*, 104 , 23,337-23,355.
- Goosse, H. and Renssen, H. 2005. A simulated reduction in Antarctic sea-ice area since 1750: Implications of the long memory of the ocean. *International Journal of Climatology* , 25 , 569-579.
- Goosse, H., Selten, F. M., Haarsma, R. J. and Opsteegh, J. D. 2001. Decadal variability in high northern latitudes as simulated by an intermediate-complexity climate model. *Annals of Glaciology*, 33, 525-532.
- Goosse, H., Crowley, T., Zorita, E., Ammann, C., Renssen, H. and Driesschaert, E. 2005. Modelling the climate of the last millennium: What causes the differences between simulations? *Geophysical Research Letters*, 32, L06710 , DOI: 10.1029/2005GL022368.
- Gordon, A. L. 1986. Interocean exchange of thermocline water. *Journal of Geophysical Research*, 91, 5037-5046.
- Gregory, J. M. and Huybrechts, P. 2006. Ice-sheet contributions to future sea-level change. *Philosophical Transactions of the Royal Society of London A*, 364, 1709-1731, DOI:10.1098/rsta.2006.1796.
- Gregory, J. M. and Oerlemans, J. 1998. Simulated future sea-level rise due to glacier melt based on regionally and seasonally resolved temperature changes. *Nature*, 391, 474-476.
- Gregory, J. M., Stouffer, R. J., Raper, S. C. B., Stott, P. A. and Rayner, N. A. 2002. An observationally based estimate of the climate sensitivity. *Journal of Climate*, 15, 3117-3121.
- Gregory, J. M., Huybrechts, P. and Raper, S. C. B. 2004a. Threatened loss of the Greenland ice sheet. *Nature*, 428, 616.
- Gregory, J. M., Ingram, W. J., Palmer, M. A., Jones, G. S., Stott, P. A., Thorpe, R. B., Lowe, J. A., Johns, T. C. and Williams, K. D. 2004b. A new method for diagnosing radiative forcing and climate sensitivity. *Geophysical Research Letters*, 31, L03205, DOI: 10.1029/2003GL018747.

- Gregory, J., Dixon, K. W., Stouffer, R. J., Weaver, A. J., Driesschaert, E., Eby, M., Fichefet, T., Hasumi, H., Hu, A., Jungclaus, J. H., Kamenkovich, I. V., Levermann, A., Montoya, M., Murakami, S., Nawrath, S., Oka, A., Solokov, A. P. and Thorpe, R. B. 2005. A model intercomparison of changes in the Atlantic thermohaline circulation in response to increasing atmospheric concentration *Geophysical Research Letters*, 32, L12703, DOI: 10.1029/2005GL023209.
- Greve, R. 2000. On the response of the Greenland ice sheet to greenhouse climate change. *Climatic Change*. 46, 289-303.
- Gruber, N., Gloor, M., Mikaloff Fletcher, S. E., Doney, S. C., Dutkiewicz, S., Follows, M., Gerber, M., Jacobson, A. R., Joos, F., Lindsay, K., Menemenlis, D., Mouchet, A., Sarmiento, J. L. and Takahashi, T. 2006. Oceanic sources and sinks of atmospheric CO₂. *Global Biogeochemical Cycles*, submitted.
- Holland, M. M. and Bitz, C. M. 2003. Polar amplification of climate change in coupled models. *Climate Dynamics*, 21, 221-232, DOI: 10.1007/s00382-003-0332-6.
- Houghton, R. A. and Hackler, J. L. 2002. Carbon flux to the atmosphere from land-use changes. In Trends: A Compendium of Data on Global Change. Carbon Dioxide Information Analysis Center. Oak Ridge National Laboratory, U.S. Department of Energy, Oak Ridge, Tenn., U.S.A.
- Houghton, J. T., Ding, Y., Griggs, D. J., Noguer, M., van der Linden, P. J., Dai, S., Maskell, K. and Johnson, C. A. 2001. Climate Change 2001: The Scientific Basis. Contribution of Working Group I to the Third Assessment Report of the Intergovernmental Panel on Climate Change. Intergovernmental Panel on Climate Change, Cambridge Univ. Press, Cambridge, United Kingdom and New York, USA, 881 pp.
- Huybrechts, P. 2002. Sea-level changes at the LGM from ice-dynamic reconstructions of the Greenland and Antarctic ice sheets during the glacial cycles. *Quaternary Science Reviews*, 21, 203-231.
- Huybrechts, P. and de Wolde, J. 1999. The dynamic response of the Greenland and Antarctic ice sheets to multiple-century climatic warming. *Journal of Climate*, 12, 2169-2188.
- Huybrechts, P., Janssens, I., Poncin, C. and Fichefet, T. 2002. The response of the Greenland ice sheet to climate changes in the 21st century by interactive coupling of an AOGCM with a thermomechanical ice-sheet model. *Annals of Glaciology*, 35, 409-415.
- Huybrechts, P., Gregory, J. M., Janssens, I. and Wild, M. 2004. Modelling Antarctic and Greenland volume changes during the 20th and 21st centuries forced by

- GCM time slice integrations. *Global and Planetary Change*, 42, 83-105, DOI: 10.1016/j.gloplacha.2003.11.011.
- Janssens, I. and Huybrechts, P., 2000. The treatment of meltwater retention in mass-balance parameterizations of the Greenland ice sheet. *Annals of Glaciology*, 31, 133-140.
- Jones, P. D. and Moberg, A. 2003. Hemispheric and large-scale surface air temperature variations: An extensive revision and an update to 2001. *Journal of Climate*, 16, 206-223.
- Joos, F. and Bruno, M. 1996. Pulse response functions are cost-efficient tools to model the link between carbon emissions, atmospheric CO₂ and global warming. *Physics and Chemistry of the Earth*, 21, 471-476.
- Joos, F., Plattner, G.-K., Stocker, T. F., Marchal, O. and Schmittner, A. 1999. Global warming and marine carbon cycle feedbacks on future atmospheric CO₂. *Science*, 284, 464-467.
- Klaas, C. and Archer, D. E. 2002. Association of sinking organic matter with various types of mineral ballast in the deep sea: Implications for the rain ratio. *Global Biogeochemical Cycles*, 16, DOI:10.1029/2001GB001765.
- Knutti, R. and Stocker, T. F. 2000. Influence of the thermohaline circulation on projected sea level rise. *Journal of Climate*, 13, 1997-2001.
- Latif, M., Roeckner, E., Botzet, M., Esch, M., Haak, H., Hagemann, S., Jungclaus, J. H., Legutke, S., Marsland, S., Mikolajewicz, U. and Mitchell, J. 2004. Reconstructing, monitoring and predicting multidecadal-scale changes in the North Atlantic thermohaline circulation with sea surface temperature. *Journal of Climate*, 17, 1605-1614.
- Lean, J., Beer, J. and Bradley, R. 1995. Reconstruction of solar irradiance since 1610: Implications for climate change. *Geophysical Research Letters*, 22, 1591-1594.
- Liu, H., Jezek K. C. and Li, B. 1999. Development of an Antarctic digital elevation model by integrating cartographic and remotely sensed data: A geographic information system based approach. *Journal of Geophysical Research*, 104, 23,199-23,213.
- Lunt, D., de Noblet-Ducoudré, N. and Charbit, S. 2004. Effects of a melted Greenland ice sheet on climate, vegetation and the cryosphere. *Climate Dynamics*, 23, 679-694, DOI: 10.1007/s00382-004-0463-4.

- Lythe, M. and Vaughan, D. G. 2001. BEDMAP: A new ice thickness and subglacial topographic model of Antarctica. *Journal of Geophysical Research*, 106, 11,335-11,351.
- Maier-Reimer, E., Mikolajewicz, U. and Winguth, A., 1996, Future ocean uptake of CO₂: Interaction between ocean circulation and biology. *Climate Dynamics*, 12, 711-721.
- Manabe, S. and Stouffer, R. 1994. Multiple-century response of a coupled ocean–atmosphere model to an increase of atmospheric carbon dioxide. *Journal of Climate*, 7, 5-23.
- Mann, M. E. and Jones, P. D. 2003. Global surface temperature over the past two millennia. *Geophysical Research Letters*, 30(15), 1820, DOI: 10.1029/2003GL017814.
- Marland, G., Boden, T. A. and Andres, R. J. 2003. Global, regional, and national fossil fuel CO₂ emissions. In Trends: A Compendium of Data on Global Change. Carbon Dioxide Information Analysis Center. Oak Ridge National Laboratory, U.S. Department of Energy, Oak Ridge, Tenn., U.S.A.
- Martin, J. H., Knauer, G. A., Karl D. M. and Broenkow, W. W. 1987. VERTEX: Carbon cycling in the northeast Pacific. *Deep-Sea Research*, 34, 267-285.
- Matear, R. J. and Hirst, A. C. 1999, Climate change feedback on the future oceanic CO₂ uptake. *Tellus*, 51, 722-733.
- Mathieu, P.-P. and Deleersnijder, E. D. 1998. What is wrong with isopycnal diffusion in World Ocean models? *Applied Mathematical Modelling*, 22, 367-378.
- Matsumoto, K., Sarmiento, J. L., Key, R. M., Aumont, O., Bullister, J. L., Caldeira, K., Campin, J.-M., Doney, S. C., Drange, H., Dutay, J.-C., Follows, M., Gao, Y., Gnanadesikan, A., Gruber, N., Ishida, A., Joos, F., Lindsay, K., Maier-Reimer, E., Marshall, J. C., Matear, R. J., Monfray, P., Mouchet, A., Najjar, R., Plattner, G.-K., Schlitzer, R., Slater, R., Swathi, P. S., Totterdell, I. J., Weirig, M.-F., Yamanaka, Y., Yool A. and Orr, J. C. 2004. Evaluation of ocean carbon cycle models with data-based metrics. *Geophysical Research Letters*, 31, L07303, DOI: 10.1029/2003GL018970.
- Meier, M. F. 1984. Contribution of small glaciers to global sea level. *Science*, 226, 1418-1421.
- Mellor, G. L. and Yamada, T. 1982. Development of a turbulence closure model for geophysical fluid problems. *Review of Geophysics*, 20 , 851-875.
- Mikaloff Fletcher, S. E., Gruber, N., Jacobson, A. R., Doney, S. C., Dutkiewicz, S., Follows, M., Gerber, M., Joos, F., Lindsay, K., Menemenlis, D., Mouchet, A.,

- Müller, S. and Sarmiento, J. L. 2006. Inverse estimates of anthropogenic CO₂ uptake, transport, and storage by the ocean. *Global Biogeochemical Cycles*, 20, GB2002, DOI: 10.1029/2005GB002530.
- Millero, F. J. 1979. The thermodynamics of the carbonate system in seawater. *Geochimica Cosmochimica Acta*, 43, 1651-1661.
- Mouchet, A. and François, L. 1996. Sensitivity of a global oceanic carbon cycle model to the circulation and to the fate of organic matter: Preliminary results *Phys. Chem. Earth*, 21, 511-516.
- NOCES HowTo 2003. NOCES Interannual Howto Document. <http://www.ipsl.jussieu/projets/NOCES>.
- Oerter, H., Kipfstuhl, J., Determann, J., Miller, H., Wagenbach, D., Minikin, A. and Graf, W. 1992. Evidence for basal marine ice in the Filchner-Ronne ice shelf. *Nature*, 358, 399-401.
- Oppenheimer, M. 1998. Global warming and the stability of the West Antarctic ice sheet. *Nature*, 393, 325-331.
- Opsteegh, J. D., Haarsma, R. J., Selten, F. M. and Kattenberg, A. 1998. ECBilt: A dynamic alternative to mixed boundary conditions in ocean models. *Tellus*, 50, 348-367.
- Rahmstorf, S. 1995. Bifurcations of the Atlantic thermohaline circulation in response to changes in the hydrological cycle. *Nature*, 378, 145-149.
- Rahmstorf, S. and Ganopolski, A. 1999. Long-term global warming scenarios computed with an efficient coupled climate model. *Climatic Change*, 43, 353-367.
- Ramankutty, N. and Foley, J. A. 1999. Estimating historical changes in global land cover: Croplands from 1700 to 1992. *Global Biogeochemical Cycles*, 13, 997-1027.
- Raper, S. C. B. and Braithwaite, R. J. 2005. The potential for sea level rise: New estimates from glacier and ice cap area and volume distribution. *Geophysical Research Letters*, 32, L05502, DOI:10.1029/2004GL021981.
- Raper, S. C. B. and Braithwaite, R. J. 2006. Low sea level rise projections from mountain glaciers and icecaps under global warming. *Nature*, 439, 311-313.
- Raper, S. C. B., Brown O. and Braithwaite, R. J. 2000. A geometric glacier model for sea-level change calculations. *Journal of Glaciology*, 46, 357-368.
- Raper, S. C. B., Gregory, J. M. and Stouffer, R. J. 2001. The role of climate sensitivity and ocean heat uptake on AOGCM transient temperature response. *Journal of Climate*, 15, 124-130.

- Rayner, N. A., Parker, D. E., Horton, E. B., Folland, C. K., Alexander, L. V., Rowell, D. P., Kent, E. C. and Kaplan, A. 2003. Globally complete analyses of sea surface temperature, sea ice and night marine air temperature since the late nineteenth century. *Journal of Geophysical Research*, 108, 4407, DOI: 10.1029/2002JD002670.
- Reeh, N. 1999. Mass balance of the Greenland ice sheet: Can modern methods reduce the uncertainty? *Geografiska Annaler*, 81A, 735-742.
- Renssen, H., Goosse, H., Fichefet, T., Brovkin, V., Driesschaert, E. and Wolk, F. 2005. Simulating the Holocene climate evolution at northern high latitudes using a coupled atmosphere–sea ice–ocean–vegetation model. *Climate Dynamics*, 24, 23-43, DOI: 10.1007/s00382-004-0485-y.
- Ridley, J. K., Huybrechts, P., Gregory, J. M. and Lowe, J. A. 2005. Elimination of the Greenland ice sheet in a high CO₂ climate. *Journal of Climate*, 18, 3409-3427.
- Rignot, E. J. and Jacobs, S. J. 2002. Rapid bottom melting widespread near Antarctic ice sheet grounding lines. *Science*, 296, 2020-2023.
- Rignot, E. J. and Kanagaratnam, P. 2006. Changes in the velocity structure of the Greenland ice sheet. *Science*, 311, 986-990.
- Robin, G. de Q. 1977. Ice cores and climatic change. *Philosophical Transactions of the Royal Society of London B*, 280, 143-168.
- Sarmiento, J. L., Le Quéré, C. L. and Pacala, S. W. 1995. Limiting future atmospheric carbon dioxide. *Global Biogeochemical Cycles*, 9, 121-137.
- Sarmiento, J. L., Hughes, T. M., Stouffer, R. J. and Manabe, S. 1998. Simulated response of the ocean carbon cycle to anthropogenic climate warming. *Nature*, 393, 245-249.
- Sarnthein, M., Winn, K., Jung, S. J. A., Duplessy, J.-C., Labeyrie, L., Erlenkeuser, H. and Ganssen, G. 1994. Changes in east Atlantic deepwater circulation over the last 30,000 years: Eighth time slice reconstructions. *Paleoceanography*, 9, 209-267.
- Shepherd, A., Wingham, D. J. and Rignot, E. J. 2004. Warm ocean is eroding West Antarctic Sheet. *Geophysical Research Letters*, 31, L23402, DOI: 10.1029/2004GL021106.
- Six, K. and Maier-Reimer, E. 1996. Effects of plankton dynamics on seasonal carbon fluxes in an ocean general circulation model. *Global Biogeochemical Cycles*, 10, 559-583.
- Steinhage, D., Nixdorf, U., Meye, U. and Miller, H. 2001. Subglacial topography and internal structure of central and western Dronning Maud Land, Antarctica

- determined from airborne radio echo sounding. *Journal of Applied Geophysics*, 47, 183-189.
- Stocker, T. F. and Schmittner, A. 1997. Influence of CO₂ emission rates on the stability of the thermohaline circulation. *Nature*, 388, 862-865.
- Stommel, H. 1961. Thermohaline convection with two stable regimes of flow. *Tellus*, 13, 225-230.
- Stouffer, R. J. and Manabe, S. 2003. Equilibrium response of thermohaline circulation to large changes in atmospheric concentration. *Climate Dynamics*, 20, 759-773.
- Stouffer, R. J., Yin, J., Gregory, J. M., Dixon, K. W., Spelman, M. J., Hurlin, W., Weaver, A. J., Eby, M., Flato, G. M., Hasumi, H., Hu, A., Jungclaus, J. H., Kamenkovich, I. V., Levermann, A., Montoya, M., Murakami, S., Nawrath, S., Oka, A., Peltier, W. R., Robitaille, D. Y., Sokolov, A., Vettoretti, G. and Weber, S. L. 2006. Investigating the response of the thermohaline circulation to past and future climate changes. *Journal of Climate*, 19, 1365-1387.
- Takahashi, T., Sutherland, S., Sweeney, C., Poisson, A., Metz, N., Tilbrook, B., Bates, N., Wanninkhof, R., Feely, R., Sabine, C., Olafsson, J. and Nojiri, Y. 2002. Global sea-air CO₂ flux based on climatological surface ocean pCO₂ and seasonal biological and temperature effects. *Deep-Sea Research*, 49, 1601-1622.
- Takahashi, T., et al. 2006. Climatological mean surface ocean pCO₂ and net sea-air CO₂ flux over the global oceans: Progress since 2002. *Journal of Geophysical Research*, in preparation.
- Tartinville, B., Campin, J.-M., Fichefet, T. and Goosse, H. 2001. Realistic representation of the surface freshwater flux in an ice-ocean general circulation model. *Ocean Modelling*, 3, 95-108.
- Thomas, R. H., 1973. The creep of ice shelves: Theory. *Journal of Glaciology*, 3, 38-42.
- Toniazzo, T., Gregory, J. M. and Huybrechts, P. 2004. Climatic impact of a Greenland deglaciation and its possible irreversibility. *Journal of Climate*, 17, 21-33.
- UNESCO 1987. Thermodynamics of the Carbon Dioxide System in Seawater. UNESCO Technical Papers in Marine Science 51.
- van de Wal, R. S. W. and Oerlemans, J. 1997. Modelling the short term response of the Greenland ice sheet to global warming. *Annals of Glaciology*, 27, 161-168.

- van de Wal, R. S. W. and Wild, M. 2001. Modelling the response of glaciers to climate change by applying volume-area scaling in combination with a high resolution GCM. *Climate Dynamics*, 18, 359-366.
- Vaughan, D. G. and Spouge, J. 2002. Risk estimation of a collapse of the West Antarctic ice sheet. *Climatic Change*, 52, 65-91.
- Voldoire, A. 2005. Prise en compte des changements de végétation dans un scénario climatique du XXIème siècle. PhD thesis, Univ. de Toulouse II, Toulouse, France.
- Wanninkhof, R. 1992. Relationship between wind speed and gas exchange over the ocean. *Journal of Geophysical Research*, 97, 7373-7382.
- Warner, R. C. and Budd, W. F. 1998. Modelling the long-term response of the Antarctic ice sheet to global warming. *Annals of Glaciology*, 27, 161-168.
- Weertman, J. 1974. Stability of the junction of an ice sheet and an ice shelf. *Journal of Glaciology*. 13, 3-11.
- Weiss, R. 1974. Carbon dioxide in water and seawater: The solubility of a non-ideal gas. *Marine Chemistry*, 2, 203-215.
- Wiebe, E. C. and Weaver, A. J. 1999. On the sensitivity of global warming experiments to the parameterisation of sub-grid scale ocean mixing. *Climate Dynamics*, 15, 875-893.
- Wild, M., Calanca, P., Scherrer, S. C. and Ohmura, A. 2003. Effects of polar ice sheets on global sea level in high-resolution greenhouse scenarios. *Journal of Geophysical Research*, 108, 4165, DOI:10.1029/2002JD002451.
- Williams, M. J. M., Jenkins, A. and Determann, J. 1998. Physical controls on ocean circulation beneath ice shelves revealed by numerical models. In: Ocean, Ice, and Atmosphere: Interactions at the Antarctic Continental Margin. Jacobs, S. J. and Weiss, R. F. (Eds.), Antarctic Research Series, 75, American Geophysical Union, Washington, D.C., U.S.A., pp. 285-299.